Preprint Cambridge Centre for Computational Chemical Engineering ISSN 1473 – 4273

Reviewing the modelling treatment of deposits in particulate filters for internal combustion emissions

Chung Ting Lao[1], Jethro Akroyd[1,2], Markus Kraft[1,2,3]

released: February 22, 2022

[1] Department of Chemical Engineering
and Biotechnology
University of Cambridge
Philippa Fawcett Drive
Cambridge, CB3 0AS
United Kingdom

[2] CARES
Cambridge Centre for Advanced
Research and Education in Singapore
1 Create Way
CREATE Tower, #05-05
Singapore, 138602

[3] School of Chemical
and Biomedical Engineering
Nanyang Technological University
62 Nanyang Drive
Singapore, 637459

Preprint No. 291

Keywords: Review, Emission, Ash, Computational model, Diesel particulate filter (DPF), Gasoline particulate filter (GPF)

Edited by
Computational Modelling Group
Department of Chemical Engineering and Biotechnology
University of Cambridge
Philippa Fawcett Drive
Cambridge, CB3 0AS
United Kingdom

E-Mail: mk306@cam.ac.uk
World Wide Web: https://como.ceb.cam.ac.uk/

Abstract

Internal combustion in transport vehicles is still one of the biggest contributors to ultrafine particle emissions which have been proven to have many adverse effects on human health and the environment in general. To mitigate this problem a variety of particle filters have been developed and along with these filters a whole range of models aiming to optimise filter performance. This paper reviews a wide variety of particulate filter models for vehicular emission control and presents the volume of work in a unified and consistent notation. Particle filtration models are examined with respect to their filtration efficiency, the way they handle particle deposits within the filter wall, the formation of filter cake and the role of catalytic conversion and the effect of gaseous emission. Further, the impact of the chemical and physical properties of particulate deposits on the filter regeneration process is analysed and reaction pathways and rates are presented. In addition the accumulation of ash deposits and its impact on the filter behaviour is critically reviewed. Finally, various measures are identified that can potentially improve the current particle filter models.

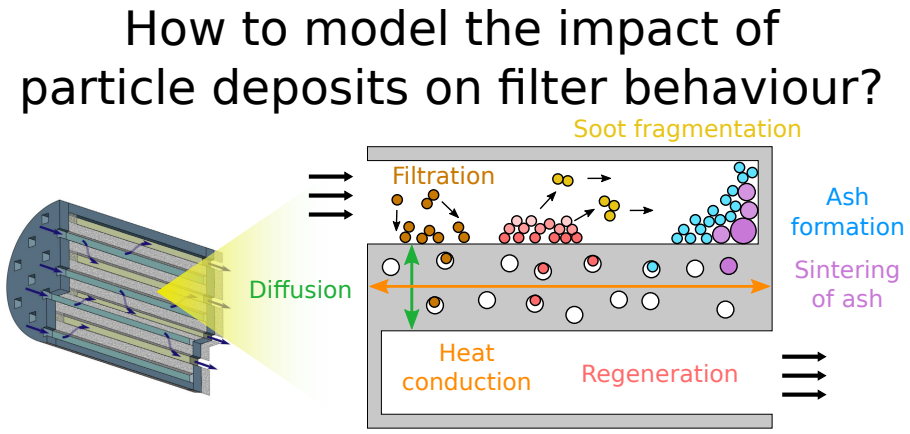

Highlights

- The treatment of particle deposits in filtration models of particulate filters is reviewed.
- The impact of particle deposit on momentum, heat and mass transfer within the particulate filter is discussed.
- Different regeneration models of particulate filters are compared.
- Current modelling approaches of ash deposits are critically discussed.

Contents

1 Introduction **4**

1.1 Particulate emissions from engines 4

1.2 Particulate filters 5

1.3 Particulate filter models 8

1.4 Scope 9

2 Modelling particle filtration **9**

2.1 Filtration efficiency of clean filters 10

2.1.1 Unit collector model 13

2.1.2 Fibrous filter filtration model 16

2.1.3 Combining different filtration mechanisms 18

2.2 Particle deposition within filter walls 19

2.2.1 Spherical unit collector model 20

2.2.2 The two-layer approach 22

2.2.3 The Kamp's and Sappok's model 23

2.2.4 Summary of in-wall deposition treatment in unit collector models 23

2.2.5 Fibrous filter model 24

2.3 Formation of the particle cake layer 25

2.4 Impact on catalytic conversion of gaseous pollutants 31

2.5 Impact on heat transfer 34

3 Modelling regeneration **36**

3.1 Reaction pathways 36

3.2 Rate equations 38

3.3 Evolution of particle deposit 44

4 Modelling ash accumulation and migration **48**

4.1 Formation mechanisms 48

4.2 Impact of ash deposits on filter performance 51

5 Summary **53**

Nomenclature **55**

References 59

1 Introduction

1.1 Particulate emissions from engines

Vehicular emission is often the biggest contributor towards ultrafine particle emissions in urban areas [158]. Particulate matter emitted by vehicles can have adverse health and environmental impacts [126, 181]. There is a great variety in the size, shape and composition of such particulates [146, 157, 179]. The properties of the particulates are influenced by the fuel composition, engine speed, engine load and combustion mode of the engine [17, 58, 127, 136]. A typical particle size distribution of particles emitted from an internal combustion engine (ICE) is shown in Fig. 1. Three size classes may be identified: the nucleation mode (below 50 nm), the accumulation mode (50 nm to 1 micron) and the coarse mode (above 1 micron) [3]. The relative proportion of particles in each mode can vary significantly depending on the engine and its operating condition [183]. Each particle mode can be approximated well by a log-normal distribution [97]. The nucleation mode is formed from nucleation of hydrocarbon and sulphates when the exhaust is cooled down. The accumulation mode is composed of soot aggregates formed during the combustion process. They may grow into coarse mode particles if they deposit on the surface of engine cylinders, which are re-entrained into the exhaust at a later stage.

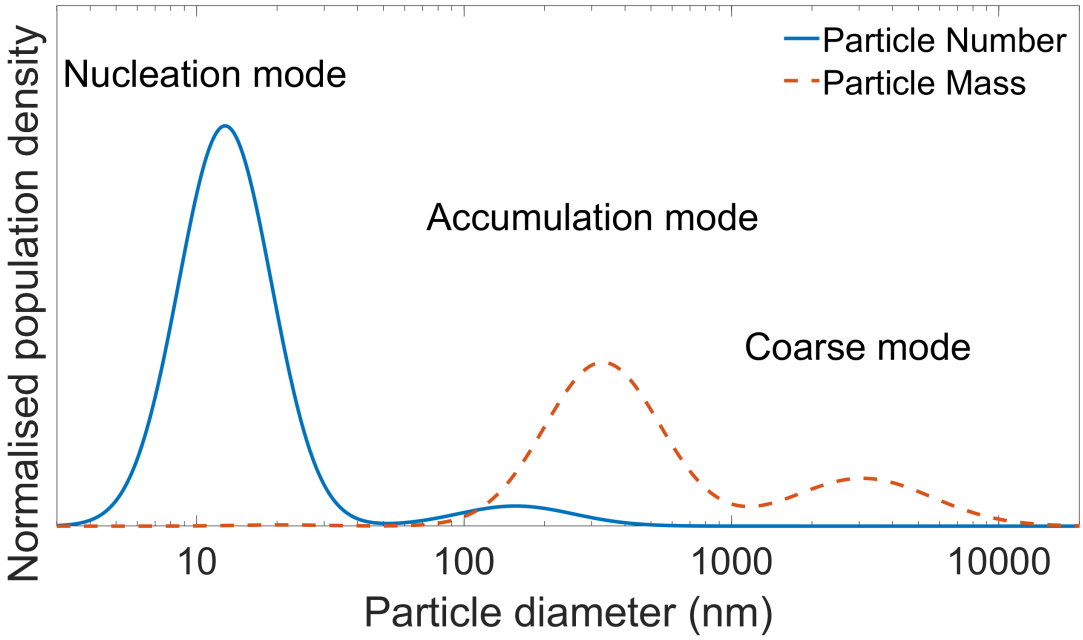

Figure 1: *A typical particle size distribution from an Internal Combustion Engine (ICE) (adapted from ref. [97]).*

The major component of engine-out particles is soot [97]. This can be loosely defined as hydrocarbon solid substances with an 8:1 carbon-to-hydrogen ratio [221]. It is the product of the inception of polyaromatic hydrocarbons (PAHs) in fuel-rich regions inside engine cylinders, where fuel pyrolysis occurs [142, 157]. The major steps of soot formation are shown in Fig. 2. Primary particles formed at the early stages are approximately spheri-

cal [26]. Primary particles can grow in size via condensation of gaseous species; larger aggregates can be formed due to the coagulation of smaller primary particles [221, 224]. This leads to a fractal-like aggregate structure as shown in Fig. 3. The morphology of the aggregate may be further modified by oxidation which can also lead to fragmentation [97].

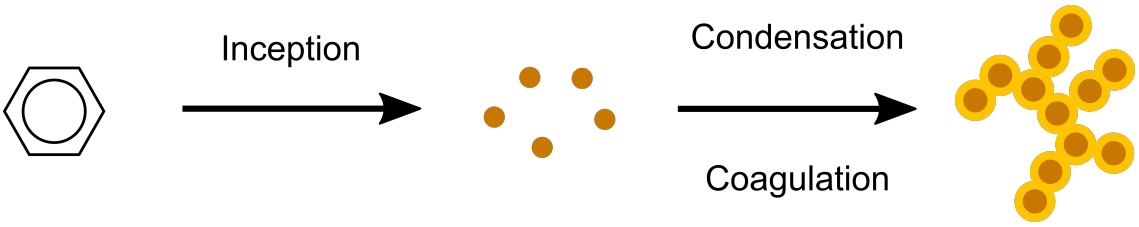

Figure 2: *Schematic diagram of soot formation process (adapted from ref. [221]).*

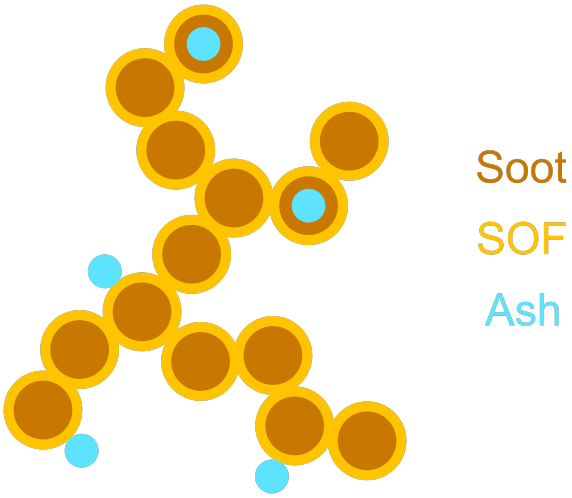

Figure 3: *A typical aggregate from Internal Combustion Engines (ICEs) [237]. Ash may be embedded within soot particles or attached to their surface.*

In addition, metallic ash may be found in engine-out particulates [237]. This originates from metallic additives doped in the fuel and the lubricant oil. Ash may be found on the surface of aggregates or is embedded within the aggregate [194]. In addition, wear and corrosion can lead to the formation of individual ash particles [147]. ICEs may also emit liquid condensate and semi-volatile particles as opposed to solid particles [124]. The semi-volatile particles are often composed of soluble organic fractions (SOFs) derived from unburnt fuel or lubricant. Inorganic species such as sulphates and phosphates can also be of significant quantity depending on the fuel formulation [247].

1.2 Particulate filters

As the negative impacts of particulates were realised, governing bodies around the world imposed limits on particulate emissions from ICEs [65]. The application of particulate filer was found to be effective in controlling engine-out particulate emissions. The Diesel

Particulate Filter (DPF) is now an essential component of diesel engine systems to comply with emission standards [154]. However, particular filters are not just relevant to diesel, but also to other types of engine.

Emission standards have been continuously revised to be more stringent as the understanding of the negative impacts of particulates and relevant measuring technologies improve [65]. The European Union (EU) introduced limits on Particle Number (PN) emission in addition to the Particle Mass (PM) limit in an attempt to reduce emissions of ultrafine particles [1]. This is because smaller particles may penetrate the respiratory system more easily than larger particles and are therefore more harmful [22]. Effective control of ultrafine particle emission will become more important as the cut-off particle size for the PN limit is expected to reduce from 23 nm to 10 nm [21].

In addition to more stringent emission standards, the emission testing procedure has been improved to minimise differences between laboratory emission measurements and real emission. Several studies have indicated that over-simplistic drive cycles, for example, the New European Drive Cycle (NEDC), can lead to underestimation of real emissions [77, 141, 204]. Drive cycles developed based on data collected from actual vehicles such as the Worldwide harmonized Light vehicles Test Cycles (WLTC) were introduced to address this issue [167]. Furthermore, the development of portable emission measurement systems (PEMS) has enabled real driving emission (RDE) tests that measure the on-road emissions from vehicles [19].

The updates of emission standards and testing protocols have been motivating for wider applications of particulate filters and newer particulate filter technologies. Gasoline Particulate Filters (GPFs) are becoming more popular for gasoline direct injection (GDI) engines to comply with the Euro 6 PN limit [80, 113]. Moreover, port fuel injection (PFI) engines may need to be installed with GPFs in the future as RDE studies have shown that PFIs can have comparable PN emission to GDI in cold environments [76, 264].

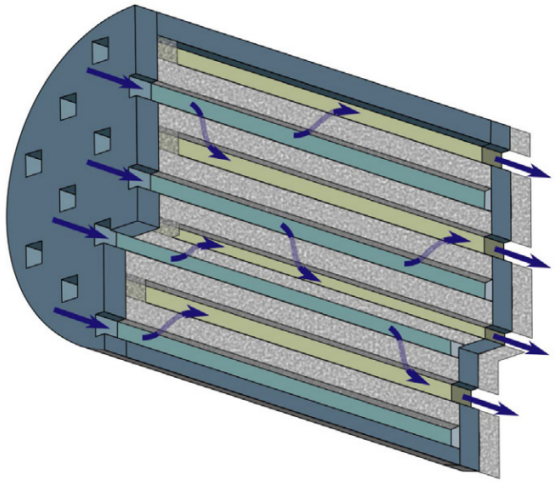

Figure 4: *The structure of a typical Wall Flow Monolith (WFM) [120].*

The most common structure of particulate filters is the Wall Flow Monolith (WFM) structure as shown in Fig. 4 [106]. The monolith is composed of a set of alternately plugged porous walled channels. The inlet channels are plugged at the rear and the outlet channels

are plugged at the front of the monolith. The engine-out exhaust enters the filter via the inlet channels and exits through the outlet channels. The porous wall between inlet and outlet channels traps the particles carried by the exhaust gas. Particle deposition inside the porous space of the wall leads to an increase in filtration efficiency but also an increase in the pressure drop across the filter. As this process continues, further in-wall particle deposition is prevented by pore closure due to already deposited particles. As a result, a particle cake layer is formed on the interface between the inlet channel and the porous wall instead.

Regeneration refers to the process of burning off the trapped particles. Regeneration is necessary to avoid high filter pressure drop (and associated fuel penalty) and overfilling of the filter [162]. "Active regeneration" describes regeneration strategies that require a temporary change in the operating condition of the filter. Typical active regeneration increases the filter temperature to promote the oxidation of trapped particles, usually by O_2. The additional heat may be provided by post-fuel injection [31], electric heaters [209] or microwaves [52, 166]. It should be noted that ash is incombustible and therefore remains in the filter after regeneration.

On the contrary, "passive regeneration" occurs spontaneously whenever the operating condition is favourable without active control. Passive regeneration usually relies on NO_2 as the oxidant, since it is a stronger oxidising agent than O_2 which allows particle combustion to occur at a lower temperature [248]. An oxidation catalyst is needed to produce NO_2 for passive regeneration since engine-out NO_2 concentration is insufficient [71]. It should be noted that GPFs operate at different conditions than DPFs and therefore their regeneration strategies differ significantly. Passive regeneration of GPFs with O_2 is possible since the exhaust temperature from gasoline engines is usually higher than that of diesel engines [28]. Spontaneous regeneration of GPFs can occur during deceleration, at which point additional air flows through the engine and provides sufficient O_2 for regeneration reactions [24].

DPFs with catalytic coatings were developed in order to improve the regeneration performance [100]. Oxidation catalysts such as Precious Group Metals (PGM) may be coated inside or on the surface of the porous wall to promote passive regeneration via *in-situ* NO_2 generation [94, 259]. In addition, oxidation catalysts can increase the reactivity of O_2 regeneration and thus lower the ignition temperature of soot [15]. NO_x removal ($deNO_x$) catalysts including lean NO_x trap (LNT) and selective catalytic reduction (SCR) catalysts can be coated on DPF walls to reduce the volume of the overall exhaust after-treatment system [35, 92]. Similarly, three way catalysts (TWC) are often coated on GPFs for the same reason [117].

In contrast to the conventional filter design shown in Fig. 4, alternative structures have been developed in order to further improve the performance of particulate filters [71]. Increasing the cross-sectional area of inlet channels can increase the particle storage capacity and achieve lower pressure drop at the same particle loading with respect to filters with symmetrical channel designs [6, 260]. Filters with triangular and hexagonal cross-sections have been studied and they exhibit different heat and mass transfer behaviour to channels with square cross-sections [231]. More sophisticated filter designs where channels may have more than one type of cross-section have also been explored, for example, the Octo-Square (OS) design [105] and Hexagonal-Rectangular-Triangular (HRT) design

[245]. They have shown better performance than the traditional design and they are not limited to the 1:1 ratio of inlet and outlet channels [159].

1.3 Particulate filter models

Many particulate filter models have been developed in order to reduce the cost of the design process and to interpret experimental results and gain more insight into filter behaviour [60, 100, 102, 256]. Adequate consideration of phenomena occurring at multiple length scales is essential for accurate prediction of filter behaviour. Particulate filter models can be put into three main categories based on the length-scale of interest, namely pore-scale, channel-scale and monolith-scale [60]. Depending on the length-scale, the balance equations describing momentum, thermal energy, species, and particle population are solved in different levels of detail.

Pore-scale models focus on processes happening within individual pores of the filter wall. A prerequisite of meaningful pore-scale simulations is to consider "*a sufficiently large domain that contains statistical representation of the morphological features present in the studied system*" [99]. Experimental techniques such as X-ray tomography (XRT) can be used to provide a detailed three-dimensional topology of the porous wall as an input to pore-scale models [226, 254]. The gas flow through the porous network can either be solved by Computational Fluid Dynamics (CFD) approaches or Lattice Boltzmann Methods (LBM) [13, 99]. The trajectories of individual particles can be solved by Lagrangian particle tracking [175]. Since the characteristic length of pore-scale models is $\mathrm{O}(\mathrm{nm}) - \mathrm{O}(\mu\mathrm{m})$, high spatial resolution is needed for convergence, and hence pore-scale models are generally very demanding of computational resources. The Eulerian-Eulerian approach is often adopted for both the gas phase and particle phase in order to reduce the computational cost [14].

Channel-scale models focus on the relevant phenomena occurring at the scale of the channel diameter, $\mathrm{O}(\mu\mathrm{m}) - \mathrm{O}(\mathrm{mm})$. Single-channel models consider an inlet channel and an outlet channel of the wall-flow monolith. In the case of filters with asymmetric channel designs, channel-scale models should simulate the "minimum repeating unit" of the filter; for example, three hexagonal channels, three rectangular channels and a triangular channel are needed to be considered for the HRT filter design [245]. The gas flow and associated heat and mass transfer may be solved by commercial CFD software packages; this approach is called the "3D single-channel model". Since the cross-section of filter channels usually exhibit rotational symmetries, the channel model may be simplified into 2D or 1D single-channel models [256]. Empirical correlations are often employed to describe convective heat and mass transfer processes in 1D single-channel models [20]. The detailed structure of the porous wall is not fully resolved in channel-scale models. It is usually approximated as an assemble of simple geometries *i.e.* the "cell model" [236]. These are discussed in more detail in the next section.

Monolith-scale models consider an ensemble of multiple inlet and outlet channels. They are developed to study the impact of inlet maldistribution and interaction between filter channels [256]. The behaviours of inlet channels may not be identical if they are subjected to different inlet conditions. Single-channel models cannot describe the filter behaviour

adequately in these cases. The spatial domain of the filter model may need to be extended beyond the filter channels in order to study the flow distribution effect [216]. Monolith-scale models are generally expensive to solve given the large spatial domain involved.

The choice of model depends on the purpose, expected level of detail, accuracy required and computational cost limitation of the particular application. Single-channel models are the most popular in the scientific literature since they provide a good compromise between predictive power and computational cost [102]. Pore-scale models are becoming more popular as designers are interested in optimising the catalytic coating and microstructure of the porous wall for better filtration and pollutant conversion [175, 249]. Multi-channel models are valuable in assisting designs of inlet cones as well as investigation of non-uniform filter behaviour [115].

1.4 Scope

Many balance equations, including those of momentum, thermal energy, species and particle population need to be solved by filter models. The process described by these equations can be influenced by the properties of incoming and deposited particles. Adequate description of the particle phase is essential for an accurate filter model. This is not an easy task given the wide range of size, morphology and composition exhibited by engine-out particulates.

This review seeks to answer the following questions:

1. How have the state and the impact of particles been considered in existing filter models?
2. What level of detail is needed in order to adequately describe the impact of particles on filter behaviour?

The rest of this paper is structured as follows: Modelling of the filtration process and the influence of trapped particles on the filter behaviour are described in Section 2. Filter regeneration models and the treatment of particle deposit during regeneration are described in Section 3. The accumulation of incombustible ash deposits and their impact on the filter behaviour is described in Section 4. Finally, the review is summarised in Section 5 with suggestions for future work.

2 Modelling particle filtration

The soot deposition process in particulate filters may be divided into four stages as shown in Fig. 5. The first stage is called the “deep bed filtration” or “depth deposition” stage where particles are trapped within the filter wall. As particles deposit within the filter wall, they can block the pores on the surface of the wall. This forces incoming particles to build upon the wall surface instead. At first, lumps of particles are observed over the blocked pores [148]. These are referred to as “particle trees” and this stage is called the

"particle tree growth" stage. The thickness of the cake layer (which is non-uniform at this point) is increasing most rapidly at this stage [49]. As particle deposition continues, the particle trees being to grow laterally, where particles are depositing on the ceramic surface [148]. The thickness of the cake layer grows more slowly at this "particle tree connection" stage. The soot cake layer becomes uniform by the end of the connection stage, at which point the rate of soot cake thickness growth becomes steady [49]. The onset soot cake layer thickness at the beginning of this "soot cake layer" stage has been found to be between 20–50 microns [49, 148].

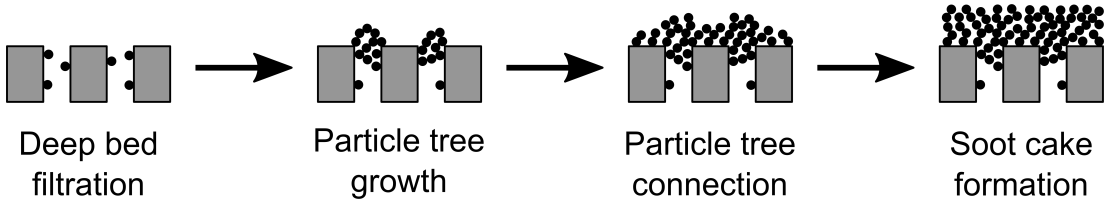

Figure 5: *The build-up of the soot cake layer is initially non-uniform.*

2.1 Filtration efficiency of clean filters

The filtration process is controlled by the properties of the filter medium, the particles being filtered and the carrying fluid [66]. The ideal gas law is commonly used to describe the gaseous exhaust carrying engine-out particulates [93, 103, 122]. The gas flow across the filter wall is determined by its tortuous internal pore network which is highly related to the manufacturing process [164].

The movement of particles may be simulated by solving the Lagrangian equation of motion for the particles [8]

$$m_\mathrm{p} \frac{\mathrm{d}\underline{v}_\mathrm{p}}{\mathrm{d}t} = \sum \underline{F}, \tag{1}$$

where m_p is the mass of a particle, $\underline{v}_\mathrm{p}$ is the vector of particle velocity and $\sum \underline{F}$ is the resultant force acting on the particle. The contributions to the force from drag and Brownian motion are usually considered [13], whereas gravitational force can be ignored for engine-out particulates [8].

The drag force of a particle $\underline{F}_\mathrm{D}$ may be represented by [62]

$$\underline{F}_\mathrm{D} = \frac{3\pi\mu \left(\underline{v} - \underline{v}_\mathrm{p}\right) d_\mathrm{p}}{C_\mathrm{c}}, \tag{2}$$

where μ is the dynamic viscosity of the carrying fluid, $\underline{v}$ is the velocity of the carrying fluid, d_p is the particle diameter and C_c is the Cunningham correction factor

$$C_\mathrm{c} = 1 + \mathrm{Kn}\left(C_1 + C_2 \exp\left[-\frac{C_3}{\mathrm{Kn}}\right]\right), \tag{3}$$

where C_1, C_2 and C_3 are empirical parameters. Their values depend on the carrying gas. It is common to assume that the carrying gas has the same properties as air, in which case $C_1 \approx 1.257$, $C_2 \approx 0.4$ and $C_3 \approx 1.1$ [168]. The Knudsen number Kn is the ratio of the mean free path of gas molecules to the particle radius [62]

$$\mathrm{Kn} = \frac{2\lambda}{d_\mathrm{p}}, \tag{4}$$

where the mean free path λ is calculated by

$$\lambda = \frac{\mu}{\rho}\sqrt{\frac{\pi \overline{M}_\mathrm{r}}{2RT}}, \tag{5}$$

where ρ is the gas density, $\overline{M}_\mathrm{r}$ is the average molecular weight of the gas, R is the universal gas constant and T is the gas temperature.

The Brownian diffusion force F_B may be described as [13]

$$\underline{F}_\mathrm{B} = \frac{3\pi\mu\left(\underline{v} - \underline{v}_\mathrm{p}\right) d_\mathrm{p}}{C_\mathrm{c}} \sqrt{2D_\mathrm{p}} \frac{\mathrm{d}W}{\mathrm{d}t}, \tag{6}$$

where W is a 3D Wiener process and D_p is the diffusion coefficient of particles [54]

$$D_\mathrm{p} = \frac{k_\mathrm{B} T C_\mathrm{c}}{3\pi\mu d_\mathrm{p}}, \tag{7}$$

where k_B is the Boltzmann constant.

Eq. (1) may be called the Langevin equation when the Brownian diffusion force is included [13]. The thermophoretic force may be included as a deterministic term in eq. (1) as shown by Matte-Deschênes et al. [145], but its contribution is only significant when high space velocity occurs, typically far above those seen in practical devices. Pore-scale models often assume particles are trapped once they make contact with the filter wall with 100% efficiency [145, 175]. This is generally true except for sub-10 nm particles which can bounce off from the wall surface due to the high kinetic energy-to-mass ratio [206].

Solving for the particle mass concentration is an alternative to solving eq. (1) in order to reduce computational demand [249, 253, 255]. The local mass fraction of trapped particles is given by the following equation, which is used in conjunction with the Lattice Boltzmann Method (LBM) model [252]

$$Y_\mathrm{C,s}\left(\underline{\mathrm{x}}, t + \Delta t\right) = Y_\mathrm{C,s}\left(\underline{\mathrm{x}}, t\right) + \sum_\mathrm{g} f_\mathrm{C,g}\left(\underline{\mathrm{x}}, t\right) \cdot p_\mathrm{D}, \tag{8}$$

where $Y_\mathrm{C,s}\left(\underline{\mathrm{x}}, t\right)$ is the mass fraction of soot particles in the solid phase at position $\underline{\mathrm{x}}$ and time t. $f_\mathrm{C,g}$ is the distribution function of soot mass fraction in the LBM model. The sum of all $f_\mathrm{C,g}$ gives the soot mass fraction in the gas phase. The deposition probability

p_D determines the number of particles trapped when they flow through a filtering node. Particles that are not trapped will bounce back into the gas flow [255]. The deposition probability is calibrated based on experimental data and treated as a constant [249].

In channel-scale models, particles are usually assumed to distribute homogeneously in the carrying gas and follow the streamlines of the gas [93, 135]. The "unit-cell" approach is commonly used to describe the filtration process in channel-scale particulate filter models [14, 102]. The complex internal structures of the filter wall are represented by an ensemble of particle "collectors" with simple geometry *e.g.* spheres (for extruded ceramic filters) or cylinders (for fibrous filters) [119, 233]. The diameter of a spherical collector d_c can be estimated from the pore diameter d_{pore} and the porosity of the filter wall ε_w. Assuming that the filter wall is composed of uniform cylindrical pores, the pore diameter is four times the ratio of the total pore volume to the total pore surface area [66, 168]:

$$d_c = \frac{3\left(1-\varepsilon_w\right)}{2\varepsilon_w} d_{pore}. \tag{9}$$

The rest of this paper only considers models for filter walls with homogeneous microstructure *i.e.* uniform pore size and porosity everywhere within the filter wall. Real filter wall substrates can be highly non-uniform with great local variations of both porosity and pore size [67, 251]. The readers are recommended to read publications by Gong and Rutland [66], Gong et al. [68] and Wang et al. [236] for details of filtration models that consider variations in porosity and pore diameter.

The overall filtration efficiency of a filter wall represented as a bed of spherical collectors can be derived from classical filter model theory [104, 125]

$$E = 1 - \exp\left[-\frac{3C_S}{2}\frac{\eta\left(1-\varepsilon\right)w}{\varepsilon d_c}\right], \tag{10}$$

where E is the overall filtration efficiency, η is the collection efficiency of a single collector, ε and w are the porosity and the thickness of the filter medium. The sticking coefficient C_S is an empirical parameter introduced to calibrate the single collector efficiency η to fit against experimental data[202], although it is frequently assumed to be 1. The overall filtration efficiency of a filter wall with a fibrous structure can be calculated as [25]

$$E = 1 - \exp\left[-\frac{4C_S}{\pi}\frac{\eta\left(1-\varepsilon\right)w}{\varepsilon d_f}\right], \tag{11}$$

where d_f is the diameter of a fibre. In some modelling works, the effective thickness of the filter medium w in eqs. (10) and (11) may not be the actual thickness of the entire medium. For example, Serrano et al. [202] assumed only a fraction of the filter medium is considered to be trapping particles. This is based on the experimental observation that soot particles only penetrate filter walls superficially [59]. In such models, the filtration process is omitted in the remainder of the filter medium. This modelling approach will be called the "two-layer" approach in the rest of this paper.

The gas flow around a single collector or fibre can be described analytically by the Kuwabara and Happel models [66]. These two models assume different boundary conditions at the surface of the collector. the Happel model assumes that the tangential stress vanishes at fluid-solid boundary whereas the Kuwabara model assumes that the vorticity vanishes [233]. The filtration efficiency of a single collector via a specific filtration mechanism can then be derived. The three major filtration mechanisms, namely Brownian diffusion, interception and inertial impaction, are shown in Fig. 6.

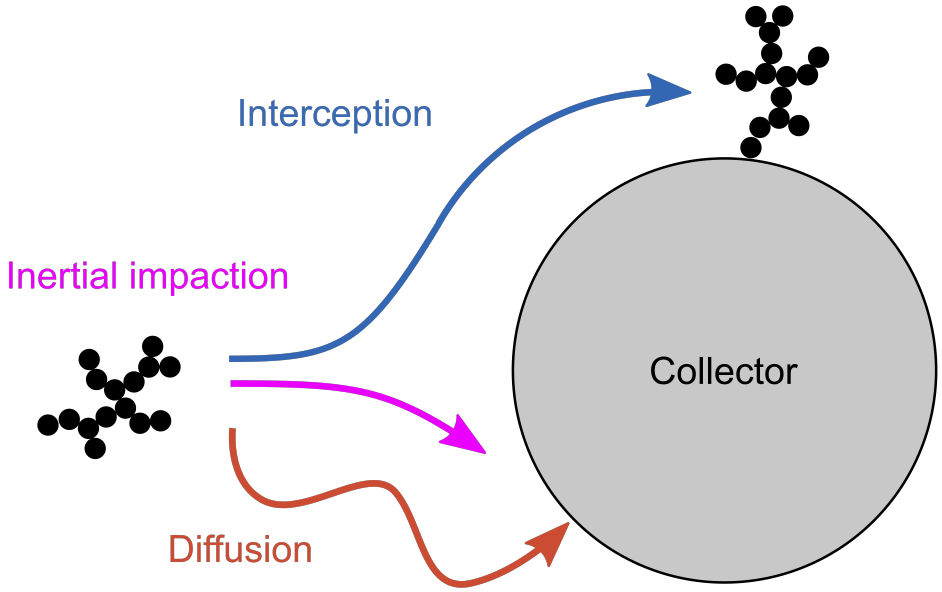

Figure 6: *Summary of filtration mechanisms in filter wall [202].*

Brownian diffusion considers particle deposition onto the collector due to random collision with gas molecules. Interception considers particles that are trapped on the collectors because they follow along gas streamlines that lie closely to the surface of collectors [161]. Inertial impaction considers the filtration of particles that are too large to follow the streamlines that cannot change direction fast enough to avoid colliding with the collector.

2.1.1 Unit collector model

Various expressions of the single collector efficiencies for each filtration mechanism have been presented by different authors in the literature. A general expression for diffusional single collector efficiency η_{B} is

$$\eta_{\mathrm{B}} = C_1 \left(\frac{\varepsilon}{K}\right)^{\frac{1}{3}} \mathrm{Pe}^{C_2}, \tag{12}$$

where C_1 and C_2 are numerical coefficients. The Kuwabara function K, which derives from the Kuwabara model of the flow around the collector, is a function of the porosity ε [66]

$$K = 1 - 1.8\,(1-\varepsilon)^{\frac{1}{3}} + (1-\varepsilon) - 0.2\,(1-\varepsilon)^2, \tag{13}$$

and the Peclet number Pe is

$$\mathrm{Pe} = \frac{v d_\mathrm{c}}{D_\mathrm{p}}, \tag{14}$$

where v is the gas velocity and D_p is the particle diffusion coefficient calculated as per eq. (7). It should be noted that unit collector models are essentially one-dimensional, and hence all velocities mentioned here and below are also one-dimensional, in the direction of the particle flow. Literature models for diffusional filtration differ in the following aspects:

1. The values of C_1 and C_2
2. Definition of gas velocity v within Pe in eq. (14)
3. Length scale used for slip-correction in the calculation of D_p ((3) and eq. (7))

According to the derivation by Lee and Gieseke [125], $C_1 = 2\left(\frac{3\pi}{4}\right)^{\frac{2}{3}} \approx 3.5$. Most existing models adopted the approximate value of 3.5 whilst Gong and Rutland [66] has used the exact value. An additional empirical multiplier was introduced by Karamitros and Koltsakis [93] in order to adjust the value of the collector efficiency to capture the behaviours of different substrate materials. The index of the Peclet number C_2 is usually $-\frac{2}{3}$ [169, 202, 215]. Recent studies have shown that $C_2 = -\frac{1}{2}$ is better suited for non-spherical collectors [133].

The Peclet number may be defined by either the superficial velocity U which is the through-wall gas velocity at the face of the filter wall, or the interstitial velocity u which is the actual gas velocity within the pores. They are related by

$$u = \frac{U}{\varepsilon}. \tag{15}$$

Both definitions are used in the literature. Gong and Rutland [66], Liu et al. [129] and Tan et al. [214] all used superficial velocity whereas Konstandopoulos et al. [106], Serrano et al. [200] and Payri et al. [169] used interstitial velocity. Since the original formulation developed by Lee and Gieseke [125] defined the Peclet number using the velocity at the boundary of the collectors, it may be more appropriate to define the Peclet number using the interstitial velocity for diffusional filtration. Using different definitions can lead to a factor of 2 difference in the value of η_B because the typical porosities of particulate filters are around 50% [192].

The correction for slip phenomena (eq. (3) and eq. (7)) requires the Knudsen number to be calculated (eq. (4)). Whilst most literature models have used the particle diameter to define the Knudsen number, Payri et al. [168] used the pore diameter of the filter wall as the relevant length scale for the slip phenomena. This practice is adopted by following modelling works [169, 200, 202, 214, 215]. Since the diffusion of the particle is due to random collisions with gas molecules, the relevant interface when slip occurs would be

the surface of the particle. Hence the particle diameter should be used in slip correction calculation.

The interceptional single collector efficiency has been derived by Lee and Gieseke [125] to be

$$\eta_{\mathrm{R}} = \frac{3}{2}\frac{\varepsilon}{K}\frac{N_{\mathrm{R}}^2}{(1+N_{\mathrm{R}})^s}, \tag{16}$$

where the interception parameter N_{R} is the ratio between the particle diameter d_{p} and the collector diameter d_{c}

$$N_{\mathrm{R}} = \frac{d_{\mathrm{p}}}{d_{\mathrm{c}}}. \tag{17}$$

The interception exponent $s = \frac{3-2\varepsilon}{3\varepsilon}$ is sometimes approximated to be 2 [66], which implies $\varepsilon \approx \frac{3}{8}$ (lower end of typical wall porosity [192]). Karamitros and Koltsakis [93] introduced an additional empirical multiplier to η_{R} in their model, similar to their treatment for η_{B} to account for different substrate materials.

An alternative formulation for interceptional single collector efficiency was proposed by Wurzenberger et al. [242]. The authors adapted expressions from Ohara et al. [161] (who only presented expressions for single collector efficiencies for the limiting cases $\mathrm{Re} \to 0$ and $\mathrm{Re} \to \infty$) and obtained the following expression based on fitting against experimental data

$$\eta_{\mathrm{R}} = 1.5N_{\mathrm{R}} + 10^{-7}N_{\mathrm{R}}^2. \tag{18}$$

This formulation does not consider the impact of the filter medium porosity. As a result, eq. (18) is expected to only work for highly porous filter media with collectors that are far from each other and can be approximated to be isolated.

Inertial impaction is often neglected in filtration models for particulate filters. Jiang et al. [83] showed that inertial impaction can be neglected for particles below 1 micron. This means that the inertial impaction is only relevant for coarse mode particles which are a minor fraction of engine-out particulates. However, Liu et al. [129] suggested that inertial impaction is non-negligible due to the low porosities of ceramic filters. Gong and Rutland [66] used the following expression for single collector efficiency due to inertial impaction

$$\eta_{\mathrm{I}} = \frac{\mathrm{St}_{\mathrm{eff}}^3}{(0.0014+\mathrm{St}_{\mathrm{eff}})^3}, \tag{19}$$

where the effective Stokes number $\mathrm{St}_{\mathrm{eff}}$ incorporates the influences of porosity ε and Reynolds number Re into the original Stokes number. The effective Stokes number is

$$\mathrm{St}_{\mathrm{eff}} = \left[1 + 1.75\mathrm{Re}\frac{\varepsilon}{150(1-\varepsilon)}\right]\mathrm{St}, \tag{20}$$

where the original Stoke number St is

$$\mathrm{St} = \frac{\rho_\mathrm{p} d_\mathrm{p}^2 U}{18 \mu d_\mathrm{c}}, \tag{21}$$

and the Reynolds number Re is

$$\mathrm{Re} = \frac{\rho_\mathrm{g} U d_\mathrm{c}}{\mu}, \tag{22}$$

where ρ_p is particle density and ρ_g is gas density. Gong and Rutland [66] defined both Reynolds and Stokes numbers using the superficial velocity U.

Serrano et al. [202] has the following expression for η_I which is inherited in later works [200, 215]

$$\eta_\mathrm{I} = \frac{\mathrm{St}'^2}{(0.25 + \mathrm{St}')^2}, \tag{23}$$

where a different definition was used for the Stokes number St′

$$\mathrm{St}' = \frac{\rho_\mathrm{p} d_\mathrm{p}^2 u}{9 \mu d_\mathrm{c}} C_\mathrm{c}, \tag{24}$$

where the Cunningham correction factor C_c is calculated based on the pore diameter of the filter medium. In contrast to eq. (21), the interstitial velocity u is used in defining the Stokes number in eq. (24). This is thought to be more appropriate as the interstitial velocity would be the actual gas velocity "experienced" by the particle. The use of interstitial velocity also incorporates the influence of filter wall porosity into the inertial filtration efficiency expression.

2.1.2 Fibrous filter filtration model

Significantly fewer modelling works have considered particulate filters with fibrous walls. The following expression was used by Wang et al. [233] and Liu et al. [129] for diffusional single fibre efficiency η_Bf

$$\eta_\mathrm{Bf} = 1.6 \left(\frac{\varepsilon}{K_\mathrm{f}} \right)^{\frac{1}{3}} \mathrm{Pe}^{-\frac{2}{3}} C_\mathrm{B1} C_\mathrm{B2}, \tag{25}$$

where K_f is the Kuwabara function for fibrous filters

$$K_\mathrm{f} = -0.5 \ln(1-\varepsilon) + (1-\varepsilon) - 0.25 (1-\varepsilon)^2 - 0.75. \tag{26}$$

The coefficients of diffusional single fibre efficiency C_B1 and C_B2 are

$$C_{\mathrm{B1}} = 1 + 0.388\mathrm{Kn}\left(\frac{\varepsilon \mathrm{Pe}}{K_{\mathrm{f}}}\right)^{\frac{1}{3}}, \tag{27}$$

$$\frac{1}{C_{\mathrm{B2}}} = 1 + 1.6\left(\frac{\varepsilon}{K_{\mathrm{f}}}\right)^{\frac{1}{3}} \mathrm{Pe}^{-\frac{2}{3}} C_{\mathrm{B1}}, \tag{28}$$

where the Peclet number Pe and Knudsen number Kn are calculated using the particle diameter d_{p} and the superficial velocity U. The Knudsen number is included to account for the slip effect of gas molecules at the surface of particles [129]. Ou et al. [165] used a variation of eq. (25) without C_{B2} where the fibre diameter d_{f} and the superficial velocity U were used to define C_{B1}, Kn and Pe.

Wang et al. [233], Liu et al. [129] and Ou et al. [165] used the following expression for the interceptional filtration in fibrous filters

$$\eta_{\mathrm{Rf}} = 0.6\left(\frac{\varepsilon}{K_{\mathrm{f}}}\frac{N_{\mathrm{Rf}}^2}{1+N_{\mathrm{Rf}}}\right)\left(1 + 1.996\frac{\mathrm{Kn}}{N_{\mathrm{Rf}}}\right), \tag{29}$$

where Kn is defined by the fibre diameter. The interception parameter for fibrous filters N_{Rf} is similar to that of the unit collector model except for the collector diameter d_{c} in eq. (17) is replaced by the fibre diameter d_{f}.

Babaie Rabiee et al. [8] used a different expression for η_{Rf}

$$\eta_{\mathrm{Rf}} = \frac{1+N_{\mathrm{Rf}}}{2K_{\mathrm{f}}}\left[2\ln\left(1+N_{\mathrm{Rf}}\right) - \varepsilon + \left(1+N_{\mathrm{Rf}}\right)^{-2}\left(1 - \frac{1-\varepsilon}{2}\right) - \frac{1-\varepsilon}{2}\left(1+N_{\mathrm{Rf}}\right)^2\right], \tag{30}$$

which is derived using the Kuwabara flow field by Liu and Wang [132].

The single fibre efficiency due to inertial impaction is modelled as [165]

$$\eta_{\mathrm{If}} = \frac{\mathrm{St}}{4K_{\mathrm{f}}^2}, \tag{31}$$

where the Stokes number is defined as

$$\mathrm{St} = \frac{m_{\mathrm{p}} U}{3\pi\mu d_{\mathrm{p}} d_{\mathrm{f}}} C_{\mathrm{c}}, \tag{32}$$

where m_{p} is the mass of a particle. Eq. (32) relaxed the assumption that the particle is spherical. Eq. (21) can be derived from eq. (32) by substituting $m_{\mathrm{p}} = \rho_{\mathrm{p}}\frac{\pi d_{\mathrm{p}}^3}{6}$.

Babaie Rabiee et al. [8] adopted expressions from Brown [25] for inertial impaction in fibrous filters:

$$\eta_{\mathrm{If}} = \begin{cases} \frac{\mathrm{St}}{(2K_{\mathrm{f}})^2}\left[\left(29.6 - 28\left(1-\varepsilon\right)^{0.62}\right)N_{\mathrm{Rf}}^2 - 27.5N_{\mathrm{Rf}}^{2.8}\right] & N_{\mathrm{Rf}} < 0.4, \text{low St} \\ \mathrm{St}^3\left(\mathrm{St}^3 + 0.77\mathrm{St}^2 + 0.22\right)^{-1} & \text{moderate St.} \end{cases} \tag{33}$$

Brown [25] described scenarios of low and high Stokes numbers without stating the exact ranges of low, moderate and high Stokes numbers. The inertia of the particle can cause a slight perturbation on the particle's trajectory and affect the interception efficiency at low Stokes numbers. When the Stokes number is large, the trajectory of the particle is almost a straight line. Babaie Rabiee et al. [8] applied eq. (33) for $0.01 \leq \mathrm{St} \leq 10$ without further clarification.

2.1.3 Combining different filtration mechanisms

In order to calculate the overall filtration efficiency using eqs. (10) or (11), the overall single collector (fibre) efficiency needs to be calculated by combining the single collector (fibre) efficiencies due to each filtration mechanism. Most filter models in the literature assume each filtration mechanism acts independently; this is adopted owing to mathematical difficulties [66]. Ou et al. [165] considered the enhancement of interception due to Brownian motion, where particles that would not have been trapped by pure interception are filtered because they are "pushed" towards the collector surface due to Brownian motion. The additional single fibre efficiency η_{BRf} is

$$\eta_{\mathrm{BRf}} = \frac{1.24 N_{\mathrm{Rf}}^{\frac{2}{3}}}{\sqrt{K_{\mathrm{f}}\mathrm{Pe}}}. \tag{34}$$

Many authors have combined single collector (fibre) efficiencies by treating them as probabilities [39, 169, 215, 242], for example [200]

$$\eta = 1 - (1-\eta_{\mathrm{B}})(1-\eta_{\mathrm{R}})(1-\eta_{\mathrm{I}}). \tag{35}$$

However, it can be seen from the equations above that the expressions used to describe the single collector (fibre) efficiencies (eqs. (12), (16), (25) etc.) are not bounded between 0 and 1. As a result, applying the independence rule of probabilities may yield unphysical values for the overall single collector efficiency. According to the early work of Lee and Gieseke [125], the diffusional single collector efficiency was defined as *" the ratio of the rate at which particles diffuse to the sphere surface to that at which particles approach toward the sphere surface within the cross-sectional area of the sphere."* A simple additive rule may be more suitable for combining single collector efficiencies since they are **not** probabilities by definition.

Some authors introduced additional multipliers to single collector efficiencies to consider the interaction between the particles and the filter wall. Wang et al. [236] introduced calibrating constants to single collector efficiencies for diffusion η_{B} and interception η_{R} respectively. The authors suggested that the introduction of these constants allows the model to account for the effect of the pore morphology of the filter wall.

The size of a particle is characterised by its diameter in filtration models. Treating particles as spheres in filter models is the most straightforward approach [212]. However, engine-out particulates often are fractal-like aggregates. To overcome this problem, real particles may be treated as spheres in the model with equivalent particle diameter and density [13]. Viswanathan et al. [229] found that the mobility diameter is the determining

parameter for filtration behaviour. Additional consideration of the shape of the particle is unnecessary since it is a function of the mobility diameter. The mobility diameter d_{mob} of engine-out aggregates may be measured using a differential mobility analyser (DMA). It may be estimated if the number n_{pri} and the diameter d_{pri} of primary particles within the aggregate are known [208]

$$d_{\text{mob}} \propto d_{\text{pri}} n_{\text{pri}}^{\frac{1}{D_{\text{mm}}}}, \tag{36}$$

where D_{mm} is the mass-mobility exponent. The value of D_{mm} depends on the flow regimes as well as the number of primary particles within the aggregate [208].

There are concerns about whether the mobility diameter is the correct length scale for **all** filtration mechanisms. A study conducted by Chen et al. [32] on particle filtration of a nuclepore filter suggested that the maximum projected length of the particle should be used to calculate the interceptional filtration efficiency to account for the elongated shape of aggregates. This approach is adopted in the work of Tan et al. [215] on DPFs. In their work, the maximum diameter is calculated using an empirical correlation considering the engine operating conditions.

In addition to the size of the particles, it is also important to describe the mass of the particles since it will affect the effect of forces acting upon the particles (in particle tracking schemes) and the mass-based filtration efficiency which is a common metric used in emission standards. The material density of engine-out particles have been reported or assumed to be in the range of 1500–2500 kg/m^3 [42, 45, 83, 130, 135, 137, 175, 248]. The mass of the particle can then be calculated if the number and the diameter of primary particles are also known.

As mentioned above, most filtration models treat aggregates as spherical particles with equivalent mobility diameters. Hence the effective density of a particle is required to correctly calculate the mass of a particle. The effective density of aggregates is usually described as a power-law relationship [69, 130, 215]

$$\rho_{\text{eff}} = C\rho_{\text{pri}} \left(\frac{d_{\text{mob}}}{d_{\text{pri}}} \right)^{q-3}. \tag{37}$$

where C is a constant and q is fractal dimension according to Gong et al. [69] and mass-mobility exponent according to Liu et al. [130] and Tan et al. [215]. Since the effective density is a function of the mobility diameter, defining q as the fractal dimension will be inappropriate since it is a pure geometric parameter [208]. Other empirical formulas to relate the effective density and the size of aggregates have been used in the literature [13, 69].

2.2 Particle deposition within filter walls

The void volume within the filter wall reduces as particles are trapped in the filter wall. This can influence the instantaneous filtration performance [67] and generally leads to an increase in both filtration efficiency and pressure drop [106, 270].

In pore-scale models, the deposition of particles can be captured by redefining the "wall" region. For example, Yamamoto and Sakai [250] tracked the local particle mass concentration within the filter wall. As it reaches unity, the local node is considered as a solid phase instead of the gas phase. An additional frictional force is applied to the gas flow in the solid region (since soot deposits are porous) [75]. This then has a subsequent impact on the gas flow pattern and the pressure drop.

2.2.1 Spherical unit collector model

In channel-scale models coupled with the spherical unit collector model, the build-up of particles within the filter wall is reflected by an increase in the collector size. The diameter of the collector d_c is often treated as a function of the mass of trapped particles [214, 242]

$$d_c = 2\left[\frac{3}{4\pi}\frac{m_{sw}}{\rho_{sw}} + \left(\frac{d_{c0}}{2}\right)\right]^{\frac{1}{3}}, \tag{38}$$

where d_{c0} is the collector diameter without any trapped particles, m_{sw} is the mass of particle deposits and ρ_{sw} is the packing density of particle deposits within the filter wall. The packing density ρ_{sw} is calibrated to match experimental pressure drop data [98]. Konstandopoulos et al. [112] showed that the value of this parameter may scale with the local Peclet number.

As the diameter of the collector increases, the filtration efficiency of the wall changes according to equations presented in Section 2.1. The local wall porosity ε_w which is another important input for the filtration model can be calculated from the local collector diameter

$$\varepsilon_w = 1 - (1 - \varepsilon_{w0})\left(\frac{d_c}{d_{c0}}\right)^3, \tag{39}$$

where the subscript 0 denotes clean wall condition.

The corresponding pressure drop across the filter wall in a channel-scale model can be described as [107, 143]

$$\Delta P = \frac{\mu w}{\kappa} v + \beta \rho_g w v^2, \tag{40}$$

where ΔP is the pressure drop, w is the thickness of the porous medium (wall), κ is the permeability of the porous medium (wall), ρ_g is the gas density and β is the Forchheimer coefficient of the porous medium (wall). The first-order term on the right-hand side represents the viscous loss and the second-order term on the right-hand side represents the inertial loss [240]. The permeability κ and the Forchheimer coefficient β can be calibrated based on experimental pressure drop data measured at various flow rates [240].

The Forchheimer coefficient of a porous medium can be derived from Ergun's equation [107]

$$\beta = \frac{1.75}{d_c}\frac{1-\varepsilon}{\varepsilon^3}. \tag{41}$$

The inertial momentum loss across porous media is often omitted in filter models due to low wall Reynolds number [14, 103, 239], albeit some experiments has shown that it has a non-negligible impact [40].

As particles deposit within the filter wall, its permeability will reduce and hence lead to an increase in pressure drop. The unit collector model calculates the permeability of the clogged wall κ_w from the local porosity ε_w and collector diameter d_c [98]

$$\kappa_w = \kappa_{w0}\left(\frac{d_c}{d_{c0}}\right)^2 \frac{f_K(\varepsilon_w)}{f_K(\varepsilon_{w0})}, \tag{42}$$

where the Kuwabara geometric function $f_K(\varepsilon)$ is [123]

$$f_K(\varepsilon) = \frac{1}{18}\frac{2-\frac{9}{5}(1-\varepsilon)^{\frac{1}{3}}-\varepsilon-\frac{1}{5}(1-\varepsilon)^2}{1-\varepsilon}. \tag{43}$$

It should be noted that some authors have used another version of eq. (43) which has a factor of 4 difference from the equation reported here [106, for example]. This has no impact on eq. (42) since only the ratio of Kuwabara functions matters. However, one needs to be careful about its impact on modelling the permeability of the clogged wall (see eq. (51)). The rest of the paper assumes the Kuwabara geometric function has the form presented above.

The permeability of the porous wall has been observed to change with temperature [228]. An additional term may be added to eq. (42) to account for the change in permeability due to change in the mean free path of the gas [139]

$$\kappa_w = \kappa_{w0}\left(\frac{d_c}{d_{c0}}\right)^2 \frac{f_K(\varepsilon_w)}{f_K(\varepsilon_{w0})}\left(1 + C\frac{P_0}{P}\mu\sqrt{\frac{T}{\overline{M}_r}}\right), \tag{44}$$

where P is the system pressure, P_0 is the reference pressure at which the clean wall permeability κ_{w0} is calibrated and C is a constant to be determined. Other empirical formulas exist to account for the reduction in wall permeability due to soot loading, for example [222]

$$\kappa_w = \frac{1}{\frac{1}{\kappa_{w0}} + C_1\rho_p + C_2\rho_p^2}\left(1 + C_3\frac{P_0}{P}\mu\sqrt{\frac{T}{\overline{M}_r}}\right), \tag{45}$$

where ρ_p is defined as the ratio of the mass of the particles to the pore volume of the wall. C_1, C_2 and C_3 are constants that require calibration.

2.2.2 The two-layer approach

In channel-scale models, the filter wall is divided into slabs with each slab having a local collector size in order to reproduce the particle deposition profile across the wall [106]. In the work of Serrano et al. [202], the porous wall was divided into two slabs. Only the top slab that is adjacent to the inlet channel is responsible for particle filtration whereas the remainder of the porous wall is always clean. This approach is based on the experimental observation that only superficial soot penetration occurs in the filter wall [59]. Whilst this "two-layer" approach is able to reproduce the pressure drop trend during the filtration process, it provides little predictive power for scenarios not considered during calibration. Furthermore, the thickness of the top slab *i.e.* the soot penetration thickness is an input to the filtration model. The penetration thickness may be estimated using a correlation between the soot penetration thickness and the wall Peclet number [202].

All collectors within the top slab are assumed to behave identically in the "two-layer" model. Serrano et al. [201] introduced a multiplier called "shape factor" to account for irregular (non-spherical) increase of the collector size. Eq. (38) then becomes [169]

$$d_{\mathrm{c}} = 2\left[\frac{3}{4\pi}\frac{m_{\mathrm{sw}}}{\chi\rho_{\mathrm{eff}}} + \left(\frac{d_{\mathrm{c0}}}{2}\right)\right]^{\frac{1}{3}}, \tag{46}$$

where ρ_{eff} is the effective density of individual aggregates described in Section 2.1. Serrano et al. [201] suggested that its value should be 345 kg/m^3 to represent aggregates with medium fractal dimension and number of primary particles. The shape factor χ is bounded between 0 and 1, where a value of 1 represents the perfect spherical growth of the collector. The shape factor χ was found to increase with the soot load and is defined as [169]

$$\chi = C_1\Phi_{\mathrm{soot}}^{-C_2}, \tag{47}$$

where Φ_{soot} is a "soot density factor" and C_1, and C_2 are fitting coefficients. Their values were found to be $C_1 = 2.3136$ and $C_2 = 0.864$ by Serrano et al. [201] after calibration against experimental results. The soot density factor is defined as *"the ratio between the soot packing density inside the porous wall and the soot mass to soot penetration volume ratio"* [201]

$$\Phi_{\mathrm{soot}} = \rho_{\mathrm{eff}}\left(\frac{V_{\mathrm{sp}}}{m_{\mathrm{sw}}}\right)^{-1}, \tag{48}$$

where m_{sw} is the mass trapped inside the wall and V_{sp} is the soot penetration volume, defined as *"the volume of porous wall which is used by soot in the whole monolith"* [201]

$$V_{\mathrm{sp}} = 4d_{\mathrm{ch}}Lw_{\mathrm{w}}N_{\mathrm{ic}}\hat{w}_{\mathrm{sat}} \tag{49}$$

where d_{ch} is the side length of square inlet channels, L is the length of channels, w_{w} is the thickness of the filter wall, N_{ic} is the number of inlet channels and $\hat{w}_{\mathrm{sat}}$ is soot penetration

thickness normalised by the total wall thickness. The permeability of the entire filter wall is the harmonic mean of the permeabilities of the effective filtration slab and the clean slab, weighted by their respective thicknesses

$$\kappa_{\mathrm{w}} = \frac{\kappa_{\mathrm{w,clog}}\kappa_{\mathrm{w0}}}{\hat{w}_{\mathrm{sat}}\kappa_{\mathrm{w0}} + (1-\hat{w}_{\mathrm{sat}})\kappa_{\mathrm{w,clog}}}, \tag{50}$$

where $\kappa_{\mathrm{w,clog}}$ is the permeability of the clogged part *i.e.* the top slab. It is calculated based on the porosity and the collector diameter of the clogged wall

$$\kappa_{\mathrm{w,clog}} = f_{\mathrm{K}}(\varepsilon_{\mathrm{w}})d_{\mathrm{c}}^2 C_{\mathrm{c}}, \tag{51}$$

where variables in eq. (51) can be calculated based on eqs. (3), (39), (43) and (46).

2.2.3 The Kamp's and Sappok's model

Kamp et al. [88] and Sappok [190] used a simple model to estimate the permeability of the filter wall when it has soot deposits

$$\frac{1}{\kappa_{\mathrm{w}}} = \frac{1}{\kappa_{\mathrm{w0}}} + \hat{V}_{\mathrm{soot}}\frac{1}{\kappa_{\mathrm{soot}}}, \tag{52}$$

where $\hat{V}_{\mathrm{soot}}$ is the volume ratio of soot deposit and the total porous space within the wall. This model requires knowledge of the permeability of soot deposits κ_{soot} since it treats soot deposits within the filter wall as a layer itself. Since soot deposits are not physically a layer within the filter wall, the value of κ_{soot} may only be calibrated to match experimental pressure drop data. It was calibrated to be 9.6×10^{-16} m^2 in the work of Zhang et al. [269].

2.2.4 Summary of in-wall deposition treatment in unit collector models

Out of the three families of model described above, the one used by Kamp et al. [88] and Sappok [190] is the only one with a single degree of freedom (κ_{soot}). The other two models have two degrees of freedom. The predictions of the two-layer model developed by Serrano et al. [202] are controlled by the effective density of individual aggregates ρ_{eff} and the ratio between soot penetration thickness and the total wall thickness $\hat{w}_{\mathrm{sat}}$. The filter behaviour predicted by the standard unit collector model with multiple wall discretisation is controlled by the packing density of particle deposits within the filter wall ρ_{sw} and the number of discretisations n_{wall}.

As n_{wall} increases, the calibrated value of ρ_{sw} is expected to converge asymptotically. However, the numerical convergence with respect to n_{wall} has not been studied extensively. Researchers often choose the value of n_{wall} a priori without justification [139]. One needs to be aware of this practice and not assume that asymptotic convergence is achieved without evidence.

On the other hand, the parameters of Serrano et al. [202]'s model can be experimentally measured. Their model however requires a good estimation of the penetration thickness

of soot deposits as an input, which is supposed to be the output of the model. This limits the predictability of the model. Furthermore, the soot deposition profile within the filter wall cannot be reproduced by Serrano et al. [202]'s model.

2.2.5 Fibrous filter model

Particles trap in fibrous filters will form dendrites in the wall which have been shown to act like new fibres [217]. The fibrous filter wall was discretised into 35 slabs in the work of Wang et al. [233]. Each slab of the fibrous filter wall was split into two regions, one representing filter fibres without soot particles whereas the other representing soot dendrites within the fibrous wall. This is shown in Fig. 7.

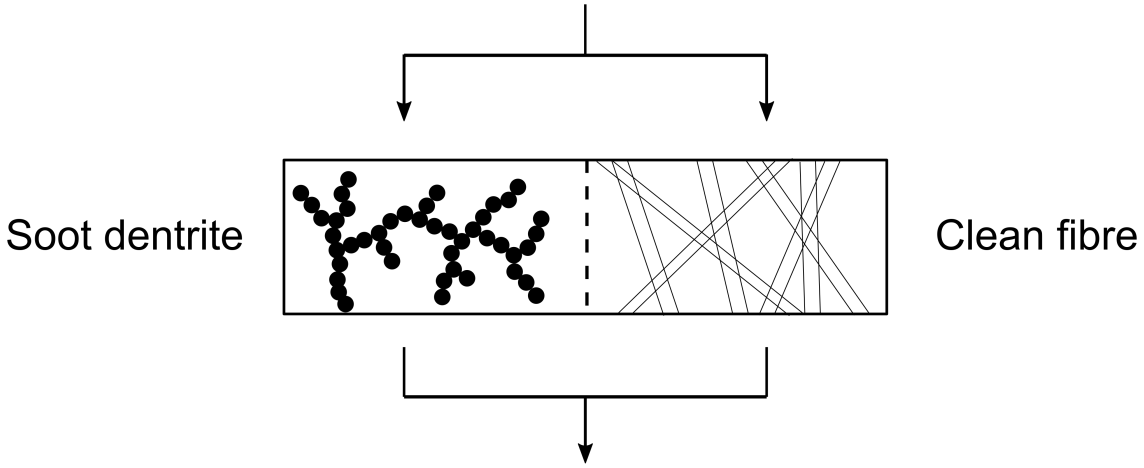

Figure 7: *The clogged portion and the clean portion of the fibrous filter wall is considered to form parallel resistance to gas flow across the wall [233].*

Wang et al. [233] incorporated this effect into a model of a filter composed on metal fibres. The filtration efficiency of the metal fibre E_f is a variation of eq. (11)

$$E_\mathrm{f} = 1 - \exp\left[\frac{-4\alpha_\mathrm{f}\eta_\mathrm{f}w_\mathrm{w}}{\pi d_\mathrm{f}\varepsilon_\mathrm{w}}\right], \tag{53}$$

where α_f is the solid volume fraction of metal fibres, η_f is the single fibre collection efficiency, w_w is the filter wall thickness, d_f is the diameter of metal fibres and ε_w is the filter wall porosity. Similarly, the filtration efficiency of the soot dendrites E_sd is

$$E_\mathrm{sd} = 1 - \exp\left[\frac{-4\alpha_\mathrm{sd}\eta_\mathrm{sd}w_\mathrm{w}}{\pi d_\mathrm{sd}\varepsilon_\mathrm{w}}\right], \tag{54}$$

where subscript "sd" denotes soot dendrite. The single collector efficiency η may be calculated as described in Section 2.1.2 using the dendrite diameter and metal fibre diameter respectively. The dendrite diameter was chosen to fit against experimental pressure drop by Wang et al. [233]. The quality of the model remains to be checked against experimental observations of the dendrites.

As the metal fibres and the soot dendrites are assumed to act as filters in parallel, they are exposed to different portions of in-flow. Wang et al. [233] assumed that the fraction of flow across the dendrite is proportional to the volume it occupies in the filter wall. The pressure drop across a slab of the clogged filter is

$$\Delta P = 64\mu U w_{\mathrm{w}} \sqrt{\left(\frac{\alpha_{\mathrm{sd}}}{d_{\mathrm{sd}}^2} + \frac{\alpha_{\mathrm{f}}}{d_{\mathrm{f}}^2}\right)} \left(\frac{\alpha_{\mathrm{sd}}}{d_{\mathrm{sd}}} + \frac{\alpha_{\mathrm{f}}}{d_{\mathrm{f}}}\right) \left(1 + 56\left(\alpha_{\mathrm{sd}} + \alpha_{\mathrm{f}}\right)^3\right). \tag{55}$$

2.3 Formation of the particle cake layer

A soot cake layer is formed on the interface between the inlet channel and the filter wall when particles deposited in the filter wall prevents further in-wall deposition. The soot cake layer can filter incoming particles effectively once it is established.

The simplest model to describe the transition from deep bed filtration to soot cake formation would be the model used by Zhang et al. [269]. A parameter called "depth filtration threshold" is defined as the maximum amount (mass) of soot allowed to deposit within the filter wall. All filtered particles are assumed to be trapped within the wall before the soot load reaches the depth filtration threshold. Once the filter wall is saturated, all subsequently filtered particles deposit on the soot cake layer. As a result, the deep bed filtration and the soot cake formation regime are distinct and non-overlapping.

Most unit collector models describe the transition by defining a dimensionless parameter called partition coefficient Φ that lies between 0 (pure deep bed filtration) and 1 (pure soot cake formation). Two versions of the formula have been seen in the literature

$$\Phi = \frac{d_{\mathrm{c,interface}}^2 - d_{\mathrm{c0}}^2}{\left(\psi d_{\mathrm{c,max}}\right)^2 - d_{\mathrm{c0}}^2}, \tag{56}$$

$$\Phi = \frac{d_{\mathrm{c,interface}}^3 - d_{\mathrm{c0}}^3}{\left(\psi d_{\mathrm{c,max}}\right)^3 - d_{\mathrm{c0}}^3}, \tag{57}$$

where $d_{\mathrm{c,interface}}$ is the collector diameter of the first filter wall slab *i.e.* the one that is closest to the inlet channel. The maximum collector diameter $d_{\mathrm{c,max}}$ is calculated by matching the porosity of the collector bed to the porosity of the clean filter wall [98]

$$d_{\mathrm{c,max}}^3 = \frac{d_{\mathrm{c0}}^3}{1 - \varepsilon_0}, \tag{58}$$

and ψ is a model parameter called the percolation constant. It controls the collector diameter at the onset of pure soot cake formation and its value is usually calibrated to match experimental pressure drop data [106].

The effect of the percolation constant is demonstrated in Fig. 8. Increasing the value of the percolation constant allow more soot to deposit within the filter wall during the deep bed filtration regime. As a result, the transition to the soot cake formation regime occurs later and at a higher filter pressure drop.

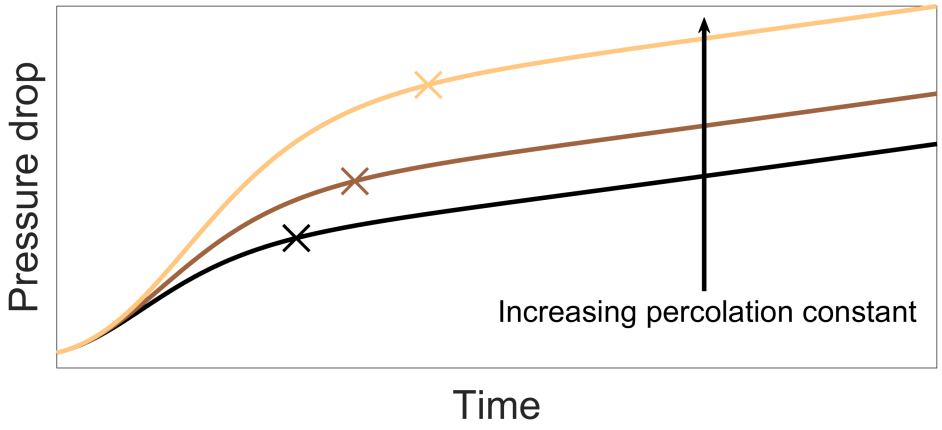

Figure 8: *The effect of the percolation constant on filter calibration. The crosses in the figure indicates the beginning of the soot cake formation regime.*

Filter models that divide the filter wall into multiple slabs often adopt eq. (56) [39, 68, 139, 242]. This formulation implies that soot cake formation is caused by the blockage of surface pores [256]. On the other hand, filter models that adopted the two-layer approach use eq. (57) to describe the transition from deep bed filtration to soot cake formation [169, 202]. The physical interpretation is that soot cake formation is caused by full saturation of the filter wall. Both eq. (56) and (57) have been shown to match well with experimental data. Nonetheless, the value of the calibrated percolation constant will be dependent on the form of the partition coefficient equation and researchers should be careful when they compare the values of percolation constants from different studies.

Both the partition coefficient approaches and the depth filtration threshold method requires the calibration of a model parameter for each set of experimental data. The depth filtration threshold is only useful at estimating the total soot load within the filter wall but it cannot predict the filter performance under a different operating condition other than the calibrated experimental dataset. Whilst the assumption behind eq. (56) resembles the experimental observations more closely, its predictive power is limited as the value of the percolation constant can vary greatly between different sets of experiments [256]. Furthermore, its value may also depend on the level of discretisation within the filter wall as discussed in Section. 2.2. In order to increase the predictive power and applicability of the partition coefficient approach, the dependence of the percolation constant on filter properties, local flow conditions, the properties of incoming particulates and the spatial discretisation should be studied. For example, Uenishi et al. [225] found that the value of the percolation constant is related to the filtration efficiency of the first wall layer and has described their relationship with a third-order polynomial. Future studies should aim to develop a correlation for percolation constant that allows accurate predictions across a wide range of particulate filters.

In addition to the build-up of the soot cake layer due to pore blockage, the soot cake layer itself is an effective filter medium. The partition coefficient is often interpreted **as** the filtration efficiency of the cake layer [68, 223]. Serrano et al. [202] proposed that the soot cake filtration efficiency is proportional to that of the porous wall, and modelled the soot

cake filtration efficiency as

$$E_{\text{cake}} = E_{\text{w}} \max\left[0, \left(\frac{\Phi - C_{\text{sat}}}{1 - C_{\text{sat}}}\right)\right], \tag{59}$$

where C_{sat} is a model parameter called the limit saturation coefficient. The cake filtration efficiency is zero when $\Phi \leq C_{\text{sat}}$. After the partition coefficient has exceeded the limit saturation coefficient, the filtration efficiency of the soot cake increases and approaches that of the wall when $\Phi = 1$.

The approaches mentioned above have considered the filtration efficiency of the soot cake as a function of the state of the filter wall only. They have neglected the effect of the cake layer *itself* on the filtration process. These approaches will not be able to describe the filtration process correctly when an appreciable soot cake layer is present but with a clean filter wall, which can occur during filter regeneration or after a partial regeneration event [119]. Karamitros and Koltsakis [93] considered the contribution towards soot cake growth from the filter wall and the cake itself separately

$$E_{\text{cake}} = E_{\text{mech1}} + E_{\text{mech2}} - E_{\text{mech1}} E_{\text{mech2}}, \tag{60}$$

where E_{mech1} is the cake filtration efficiency due to pore blockage and E_{mech2} is the filtration efficiency due to the presence of the cake. E_{mech1} is assumed to be a linear function of the filter wall porosity and E_{mech2} is assumed to be a linear function of the soot cake thickness respectively. The introduction of E_{mech2} allows the filtration capability of a developing soot cake to be modelled.

Premchand et al. [177] considered the initial soot cake formation by interpreting the partition coefficient as the filtration efficiency of the soot cake at the early stage of its formation. This continues until the permeability of the filter wall reached a pre-defined value, at which point eq. (10) was applied to describe the filtration efficiency of the soot cake. An additional multiplier was introduced by Premchand et al. [177] to eq. (10) to limit the maximum filtration efficiency of the soot cake which is chosen to be 0.937. The collector diameter in the soot cake layer is calculated using eq. (9) with a user-specified pore diameter defined as 100 nm in that work.

For fibrous filters, Wang et al. [233] modelled the cake filtration efficiency using eq. (11) with cake-specific parameters. The onset of soot cake formation is determined by the soot volume fraction of the top wall slab. This is analogous to eq. (57). Once the soot volume fraction reaches a pre-defined limit, the soot cake is formed assuming dendrites begin to grow outside of the filter.

Most filter models assume that the soot cake layer is locally uniform, which means the particle tree formation and connection regimes are ignored. Serrano et al. [202]'s model captured the impact of particle tree growth on the rate of increase of the cake thickness. The surface area on the wall-channel interface that allows soot cake to grow on $A_{\text{cakegrowth}}$ is

$$a_{\text{cg}} = 4 d_{\text{ch}} L \theta, \tag{61}$$

where θ is the area correction factor

$$\theta = \varepsilon_{w0} + (1 - \varepsilon_{w0}) \min \left[\frac{w_{cake}}{w_{cake,lim}}, 1 \right], \tag{62}$$

assuming a linear change in available area for soot cake to grow.

Initially, particle trees only grow on the pores of the porous wall, at this point $\theta = \varepsilon_{w0}$. Since there is less area for the soot cake to grow on, the rate of increase of the cake thickness is higher than when uniform cake growth is assumed. The available area for cake growth increases as the soot cake is formed during the particle tree connection stage and eventually, uniform cake growth is observed ($\theta = 1$). The cake thickness when uniform cake growth begins $w_{cake,lim}$ is a model input that may be measured experimentally [49].

The overall pressure drop of the filter is increased by the formation of the soot cake layer via two means. First, it reduces the available cross-sectional area in the inlet channels for gas flow in the axial direction. Second, an additional pressure drop is caused by gas having to flow through the soot cake layer.

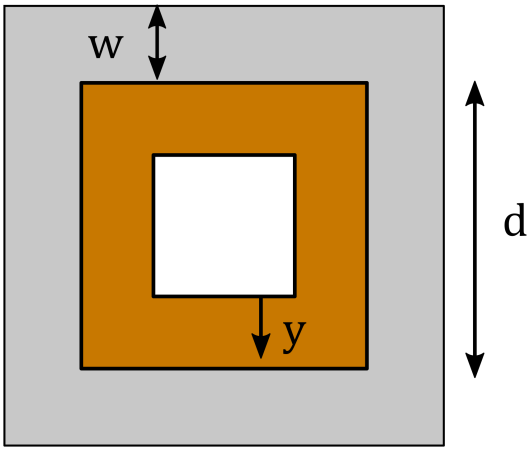

Figure 9: *The cross-section of a square inlet channel filled with soot cake [106].*

The momentum balance in the axial direction of the inlet channel in channel-scale models is [73]

$$\frac{\partial P}{\partial z} + \frac{\partial}{\partial z}\left(\rho_g v^2\right) = -\frac{F_f \mu v}{(d - 2w_w)^2}, \tag{63}$$

where P is the gas pressure, z is the axial coordinate, ρ_g is the gas density, v is the axial gas flow velocity and F_f is the friction factor. The thickness of the soot cake layer can be calculated from the mass of the soot cake, assuming that the shape of the soot cake is geometrically similar to the channel cross-section [238]. For filters with square channels as shown in Fig. 9, the thickness of the soot cake is

$$w_{cake} = \frac{1}{2}\left(d - \sqrt{d^2 - \frac{m_{cake}}{N_{ic} L \rho_{cake}}}\right), \tag{64}$$

where ρ_{cake} is the effective density of the soot cake, which is a function of the material density of soot ρ_{soot} and the porosity of the soot cake $\varepsilon_{\text{cake}}$ [108]

$$\rho_{\text{cake}} = \rho_{\text{soot}} \left(1 - \varepsilon_{\text{cake}}\right). \tag{65}$$

In situ direct measurements showed that the porosity of the soot cake layer in DPFs lies between 0.93 to 0.97 [128]. The porosity of the soot cake is expected to be no less than 0.83 [112]. The packing of the soot cake layer depends on the local gas flow condition. If the gas flow velocity is high, ballistic deposition of soot particles is expected and the soot cake will be dense; otherwise sparse diffusion-limited structures will form [79]. Konstandopoulos et al. [110] suggested that the soot cake porosity is a function of the local Peclet number

$$\varepsilon_{\text{cake}} = 1 - \left(1 - \varepsilon_{\text{cake},\infty}\right) \left(1 + \frac{\text{Pe}_0}{\text{Pe}}\right)^{-q}, \tag{66}$$

where $\varepsilon_{\text{cake},\infty}$ is the minimum cake porosity which is achieved when $\text{Pe} \to \infty$ and Pe_0 is the critical Peclet number that signifies the transition between diffusion-dominant and convection-dominant particle deposition. The value of the exponent q is not reported.

Furthermore, the packing of the soot cake layer may be affected by the local pressure [230]

$$\rho_{\text{cake}} = \rho_{\text{cake0}} \left(1 + \frac{\Delta P_{\text{cake}}}{\Delta P^*_{\text{cake}}}\right)^{q}, \tag{67}$$

where ρ_{cake0} is the uncompressed cake density, ΔP_{cake} is the pressure drop across the cake, ΔP^*_{cake} is the strength of the cake and q is a tunable exponent. Konstandopoulos et al. [110] suggested that soot cakes may exhibit Bingham-like behaviour *i.e.* the packing of the soot cake is unaffected until the pressure difference across it exceeds a critical value. They suggested using the following equation should be used to describe the pressure dependence of the soot cake packing

$$\rho_{\text{cake}} = \rho_{\text{cake0}} \left(1 + \frac{\max\left[0, \Delta P_{\text{cake}} - \Delta P_{\text{cake,cr}}\right]}{\Delta P^*_{\text{cake}}}\right)^{q}, \tag{68}$$

where $\Delta P_{\text{cake,lim}}$ is the minimum pressure drop required to affect the packing of the soot cake layer.

The pressure drop across the soot cake layer is usually described by Darcy's law (eq. (40)), which requires the knowledge of the thickness and the permeability of the soot cake layer [180, 234, 267, 272]. Assuming constant gas density across the soot cake, the pressure drop across the soot cake formed in square channels is [43]

$$\Delta P_{\text{cake}} = \frac{\mu}{\kappa_{\text{cake}}} \int_{y=0}^{y=w_{\text{cake}}} v_{\text{cake}}(y) dy = \frac{\mu v_{\text{cake,top}}}{2\kappa_{\text{cake}}} \left(d - 2w_{\text{cake}}\right) \ln\left(\frac{d}{d - 2w_{\text{cake}}}\right), \tag{69}$$

where y is the distance from the top of the soot cake as shown in Fig. 9, $v_{\text{cake,top}}$ is the gas velocity at the top of the soot cake and κ_{cake} is the permeability of the soot cake. The permeability of the cake layer has been modelled by different approaches in the literature. The easiest method would be to calibrate it directly to match experimental pressure drop data [50, 51, 267]. However, the permeability of the soot cake can be affected by the temperature and the pressure of the system. The following equation has been used to capture the change in cake permeability due to slip phenomenon [93, 155, 222]

$$\kappa_{\text{cake}} = \kappa_{\text{cake0}} \left(1 + C \frac{P_0}{P} \mu \sqrt{\frac{T}{\overline{M}_{\text{r}}}} \right), \tag{70}$$

where C is a numerical parameter, P_0 is the pressure at reference condition (at which κ_{cake0} is defined) and $\overline{M}_{\text{r}}$ is the average molecular weight of the gas. Mahadevan et al. [139] considered the change in soot cake permeability due to the change in mean free path length of the gas

$$[\rho_{\text{cake}} \kappa_{\text{cake}}] = C \frac{\lambda}{\lambda_{\text{ref}}}, \tag{71}$$

where λ is the mean free path length and λ_{ref} is the mean free path length at a specific condition. The calibration constant C is fitted against experimental data.

Some works have attempted to relate the permeability of the soot cake with its microstructure. Konstandopoulos et al. [108] used eq. (51) to estimate the soot cake permeability assuming the soot cake is a bed of spherical primary particles. The Cunningham correction factor is calculated using the primary particle diameter as the relevant length scale ($O(10\,\text{nm})$). On the other hand, Serrano et al. [201] argued that the slip phenomenon is governed by the **pore** diameter of the soot cake layer. In their work, the mean aggregate diameter ($O(100\,\text{nm})$) was used in eq. (51) instead of the primary particle diameter. As a result, the calibrated soot cake porosity ranged from 0.6 to 0.7. The discrepancy between the low soot cake porosity calibrated by Serrano et al. [201] and the experimental data measured by Liu et al. [128] (0.93–0.97) may be explained by Fig. 10.

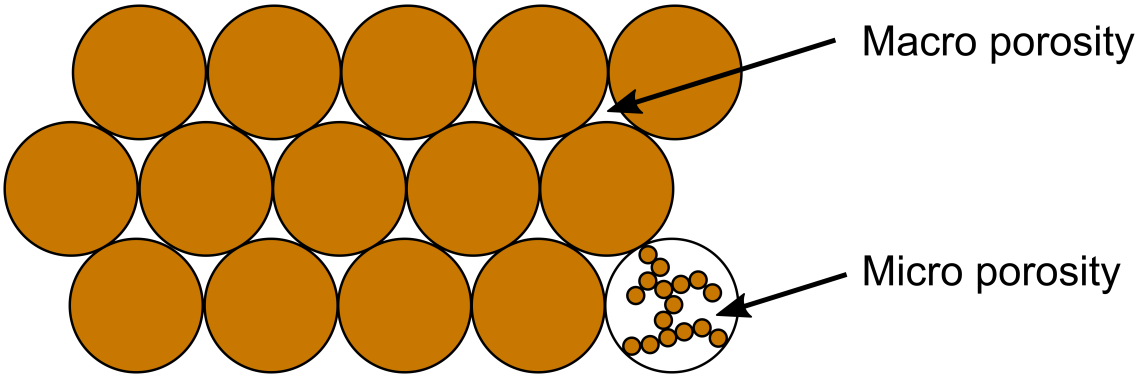

Figure 10: *Macro- and micro-porosity in the soot cake layer [215].*

Models used by Serrano et al. [201], Payri et al. [169] and Macián et al. [137] treated the soot cake layer as a spherical packed bed formed by soot aggregates. However, the soot

aggregates are "porous" because they have fractal-like structures. The actual porosity of the soot cake depends on both the macro-porosity **between soot aggregates** $\varepsilon_{\text{cake,macro}}$ and the micro-porosity **within the soot aggregates** $\varepsilon_{\text{cake,micro}}$

$$\varepsilon_{\text{cake}} = 1 - (1 - \varepsilon_{\text{cake,macro}})(1 - \varepsilon_{\text{cake,micro}}), \tag{72}$$

the true porosity of the cake becomes 0.93 if $\varepsilon_{\text{cake,macro}} = 0.65$ and $\varepsilon_{\text{cake,micro}} = 0.81$ (typical porosity of mean soot aggregate [201]) are assumed, which is consistent with experimental observations.

The equations above have assumed that all particles within the soot cake have the same size. In the case where there is a significant size variation, Endo et al. [55] proposed an equation to estimate the pressure drop across the soot cake if the soot particles within the cake have a log-normal particle size distribution

$$\Delta P_{\text{cake}} = 180 \mu U w_{\text{cake}} \frac{(1 - \varepsilon_{\text{cake}})^2}{\varepsilon_{\text{cake}}^3 C_{\text{c}}} \frac{k}{\overline{d_{\text{p}}}^2 \exp\left(4 \ln^2 \sigma_{\text{p}}\right)}, \tag{73}$$

where $\overline{d_{\text{p}}}$ and σ_{p} are the average diameter and standard deviation of the particle size distribution.

Given the high porosity in the soot cake, Thomas et al. [218] suggested that it should be modelled as a fibrous structure with "particle chains" as the fibres. The pressure drop across the soot cake can then be described as

$$\Delta P_{\text{cake}} = \frac{64 \mu U w_{\text{cake}} (1 - \varepsilon_{\text{cake}})^{\frac{3}{2}} \left[1 + 56 (1 - \varepsilon_{\text{cake}})^3\right] C_{\text{F}}}{C_{\text{c}} d_{\text{p}}^2}, \tag{74}$$

where C_{F} ranges between 1 and $\frac{3}{2}$ for cylindrical fibres and spherical particle chains respectively.

Ribeyre et al. [184] used eqs. (73) and (74) to study the effect of humidity on the pressure drop across the soot cake. It was found that whilst the thickness of the soot cake decreased slightly with increasing water content, the overall pressure drop increased with water content due to reduced permeability as void space within the soot cake was reduced. On the other hand, Konstandopoulos et al. [112] suggested that crack formation can occur if the wetted soot cake is left to dry. The pressure drop across the soot cake will therefore be reduced as cracks provided a shortcut for gas flow and hence the overall permeability is increased.

2.4 Impact on catalytic conversion of gaseous pollutants

Particulate filters often have a catalytic coating to convert gaseous pollutants and aid regeneration. Here we discuss the impact of particle deposition on the performance of catalytic filters during non-regenerating conditions. The efficiency of catalytic conversion depends on the intrinsic activity of the catalyst and the transport of reactants towards the

catalyst. Soot deposits within catalytic filters introduce additional mass transfer resistances via various means.

First, the soot cake layer can affect the convective mass transfer in the inlet channels. The species balance in the inlet channel is [163]

$$\frac{\partial c_{\mathrm{g}}}{\partial t} = -v\frac{\partial c_{\mathrm{g}}}{\partial z} - k_{\mathrm{m}}\frac{4}{d-2w_{\mathrm{cake}}}\left(c_{\mathrm{g}} - c_{\mathrm{g,w}}\right) - v_{\mathrm{w}}\frac{4}{d-2w_{\mathrm{cake}}}c_{\mathrm{gas,w}}, \tag{75}$$

where c_{g} is the molar concentration of the gas species,d is the channel diameter, w_{cake} is the soot cake thickness, v_{w} is the through-wall gas velocity and k_{m} is the convective mass transfer coefficient. In addition to modifying the effective channel diameter, the presence of the soot cake can also affect the convective mass transfer coefficient. The mass transfer coefficient may be calculated using the correlations such as the one developed by Bissett et al. [20]

$$\mathrm{Sh} = \frac{k_{\mathrm{m}}(d-2w_{\mathrm{cake}})}{D_{\mathrm{m,g}}} = 2.98 + 0.6\mathrm{Pe}_{\mathrm{w}} - 0.143\mathrm{Re}_{\mathrm{w}}, \tag{76}$$

where $D_{\mathrm{m,g}}$ is the bulk diffusivity of gaseous species, Pe_{w} is the Peclet number and Re_{w} is the Reynolds number for the through-wall gas flow, which means they are functions of v_{w}. The presence of the soot cake can affect the mass transfer coefficient implicitly due to its effect on the through-wall gas flow velocity profile via eq. (63).

Furthermore, the soot cake acts as a diffusive barrier between the in-wall catalyst and the bulk gas in the inlet channel. An advection-diffusion-reaction equation is needed to resolve the concentration gradient across the soot cake [259]

$$\frac{\partial c_{\mathrm{g}}}{\partial t} = -v_{\mathrm{w}}\frac{\partial c_{\mathrm{g}}}{\partial x} + D_{\mathrm{m,cake}}\frac{\partial^2 c_{\mathrm{g}}}{\partial x^2} + \dot{\omega}, \tag{77}$$

where x is the through-wall coordinate, $D_{\mathrm{m,cake}}$ is the effective diffusivity of the soot cake and $\dot{\omega}$ is the rate of species production due to chemical reactions. It can be seen from eqs. (75) and (77) that the presence of the soot cake will have no impact on the concentration profile if $\dot{\omega} = 0$. This is usually the case in the soot cake when no regeneration occurs within the filters [178]. A notable exception is observed in catalysed DPFs when there are notable chemical interactions between the soot cake and SCR-related species under certain operating conditions. Adsorption of NH_3 as well as fast SCR and NO_2-SCR activity was found to occur on the surface of soot deposits [152, 153]. If these reactions are appreciable, eq. (77) may need to be solved in the soot cake. Furthermore, soot may react with ammonium nitrate and produce CO/CO_2, which suppressed the formation of N_2O [151]. Under these conditions, the interaction between ammonium nitrate and soot cannot be captured by direct integration of independently developed soot and SCR kinetics [34]. It was suggested by Mihai et al. [151] that the presence of soot can inhibit the formation of ammonium nitrate which is formed at low temperature with high NO_2 at the inlet. This subsequently leads to an increase in SCR performance since less ammonium nitrate is inhibiting SCR activity.

Significant diffusion can occur within the catalysed filter wall [163]. Eq. (77) can be applied to the wall if $D_{\mathrm{m,cake}}$ is replaced by the diffusivity of the filter wall $D_{\mathrm{m,w}}$. The diffusivity of the filter wall can be estimated using the parallel pore model which considers both bulk diffusion and Knudsen diffusion [163, 222]

$$\frac{1}{D_{\mathrm{m}}} = \frac{\tau}{\varepsilon}\left(\frac{1}{D_{\mathrm{m,bulk}}} + \frac{1}{D_{\mathrm{m,Kn}}}\right), \tag{78}$$

where τ is the tortuosity of the porous medium, $D_{\mathrm{m,bulk}}$ is the molecular diffusivity of the gas and $D_{\mathrm{m,Kn}}$ is the Knudsen diffusivity

$$D_{\mathrm{m,Kn}} = \frac{d_{\mathrm{pore}}}{3}\sqrt{\frac{8RT}{\pi \overline{M}_{\mathrm{r}}}}. \tag{79}$$

In principle, the porosity and the pore diameter of the filter wall under certain soot loading may be calculated by the unit collector model using eqs. (9), (38) and (39). However, since tortuosity is usually calibrated to match experimental data [39, 93], the impact of soot deposit on in-wall diffusion via porosity reduction may be masked by the uncertainty of the tortuosity calibration. Furthermore, no model has been established to describe the variation in tortuosity as the wall soot load increases. This limits the accuracy of the effective diffusivity estimation.

In addition to the diffusion across the filter wall, Greiner et al. [70] found that pore diffusion within the catalyst particle is important and it can be more significant than the effect of advection-diffusion across the wall as described in eq. (77). The authors suggested that the application of an effectiveness factor to catalytic reactions within the wall is a good choice to consider pore diffusion in channel-scale filter models. The effectiveness factor γ is the *"ratio of the effective to the maximum reaction rate"* [156]

$$\dot{\omega} = \gamma \dot{\omega}_{\mathrm{max}}, \tag{80}$$

where $\dot{\omega}$ and $\dot{\omega}_{\mathrm{max}}$ are the actual and maximum rate of production of a chemical products. The maximum rate of production is calculated assuming the system is kinetic-limited *i.e.* there is no mass transfer limitation. It should be noted that the effectiveness factor approach assumes that the chemical reaction is first-order with a single reactant. Chundru et al. [39] modelled the impact of soot deposits on the mass transfer at the catalyst surface by adopting the unit collector concept. The model is illustrated in Fig. 11.

The thickness of the soot deposits on the surface of collectors can be shown as

$$\delta_{\mathrm{p}} = \frac{1}{2}\left(d_{\mathrm{c}} - d_{\mathrm{c0}}\right) \tag{81}$$

according to Fig. 11. The effectiveness factor in this case is

$$\gamma = \frac{\sqrt{D_{\mathrm{m,cat}} k_{\mathrm{ideal}}}\tanh\phi}{\delta_{\mathrm{p}}\sqrt{D_{\mathrm{m,cat}} k_{\mathrm{ideal}}}\tanh\phi + D_{\mathrm{m,cat}}}, \tag{82}$$

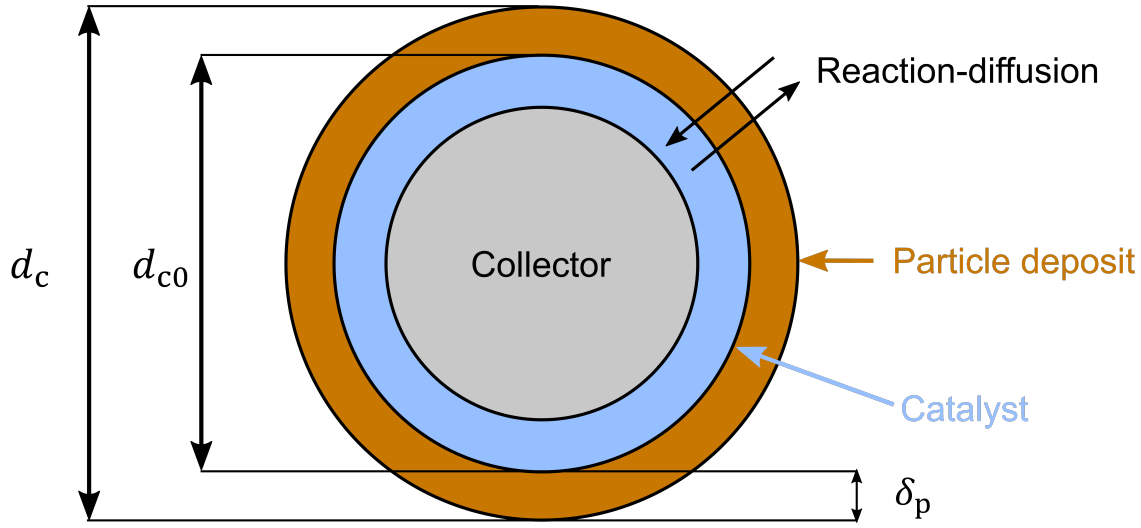

Figure 11: *Soot deposit can inhibit SCR reactions by increasing diffusional resistance between reactant and catalyst [39].*

where $D_{m,cat}$ is the diffusivity within the catalytic washcoat, k_{ideal} is the rate constant of catalytic reaction under kinetic-limited condition and ϕ is the Thiele modulus, which is the ratio of reaction and diffusion within the catalytic coating [162]

$$\phi = \sqrt{\frac{k_{ideal}\delta_p^2}{D_{m,cat}}}. \tag{83}$$

Whilst increased mass transfer resistance due to soot deposition is generally considered to be negative, the overall performance of the catalyst may benefit from deteriorated species transport. For example, the presence of soot can inhibit NH_3 oxidation in SCR-coated filters at high temperatures. This allows more NH_3 to be available for NO_x reduction reactions [151].

2.5 Impact on heat transfer

The heat transfer phenomena and temperature distributions within particulate filters are important topics within the field of filter modelling studies. Many publications have studied the thermal behaviour of particulate filters especially during active regeneration [29, 30, 64, 261–263, 271]. However, the impact of deposits on the heat transfer process has not been studied in detail.

It is common to assume that the gas within the porous wall is at local thermal equilibrium with the filter substrate [33, 45]. The temperature variation across the soot cake layer and the wall is also usually neglected in filter models. This assumption has been investigated by Haralampous and Koltsakis [72] and they found the following condition for this assumption to hold

$$\frac{c_{\mathrm{pg}}\dot{m}_{\mathrm{in}}w_{\mathrm{cake}}}{a\Lambda_{\mathrm{cake}}} \leq 0.1, \tag{84}$$

where c_{pg} is the specific heat capacity of the gas, $\dot{m}_{\mathrm{in}}$ is the inlet mass flow rate to the filter, a is the total area of the interface between the inlet channel and the porous wall and Λ_{cake} is the thermal conductivity of soot deposits. When this condition is satisfied, only a single equation is needed to be solved for the temperature of the solid phase of the filter in single-channel models [149]

$$\begin{aligned}\left(\rho_{\mathrm{cake}}w_{\mathrm{cake}}c_{\mathrm{p,cake}}+\rho_{\mathrm{w}}w_{\mathrm{w}}c_{\mathrm{pw}}\right)\frac{\partial T_{\mathrm{w}}}{\partial t} &= h_1\left(T_1-T_{\mathrm{w}}\right)+h_2\left(T_2-T_{\mathrm{w}}\right)+\rho_{\mathrm{g}}v_{\mathrm{w}}c_{\mathrm{pg}}\left(T_1-T_{\mathrm{w}}\right)\\ &\quad+\Lambda_{\mathrm{cake}}\frac{\partial}{\partial z}\left(w_{\mathrm{cake}}\frac{\partial T_{\mathrm{w}}}{\partial z}\right)+\Lambda_{\mathrm{w}}w_{\mathrm{w}}\frac{\partial^2 T_{\mathrm{w}}}{\partial z^2}+\dot{Q}.\end{aligned} \tag{85}$$

where $c_{\mathrm{p,cake}}$ is the specific heat capacity of the soot cake, ρ_{w} is the bulk density of the filter wall, c_{pw} is the specific heat capacity of the filter wall, h_1 and h_2 are the convective heat transfer coefficients between the filter wall and the inlet/outlet channel, Λ_{w} is the thermal conductivity of the filter wall and $\dot{Q}$ is the temperature source term due to regeneration reactions. Eq. (85) shows that soot deposits can affect heat transfer in the following ways:

1. Additional heat capacity in solid phase ($\rho_{\mathrm{cake}}w_{\mathrm{cake}}c_{\mathrm{p,cake}}+\rho_{\mathrm{w}}w_{\mathrm{w}}c_{\mathrm{pw}}$)
2. Convective heat transfer with inlet channel (h_1)
3. Heat conduction in the soot cake layer and the filter wall ($\Lambda_{\mathrm{cake}}\frac{\partial}{\partial z}\left(w_{\mathrm{cake}}\frac{\partial T_{\mathrm{w}}}{\partial z}\right)+\Lambda_{\mathrm{w}}w_{\mathrm{w}}\frac{\partial^2 T_{\mathrm{w}}}{\partial z^2}$)
4. The heat of regeneration reaction ($\dot{Q}$)

The heat released from regeneration can be calculated from the change in enthalpies of gaseous reactants and products [7, 149]. The convective heat transfer coefficient in the inlet channel depends on the gas flow across the wall, characterised by the wall Reynolds number and the Prantdl number [20, 116, 231]. The presence of soot in and on the wall can affect h_1 implicitly, similar to its impact on convective mass transfer (Section 2.4).

The density and the thickness of the soot cake layer have been investigated by many researchers and have been discussed in Section 2.3. On the other hand, the specific heat capacity $c_{\mathrm{p,cake}}$ and the thermal conductivity Λ_{cake} of soot deposits have not been subjected to the same level of scrutiny. The impact of soot loading on the filter wall thermal conductivity Λ_{w} is usually neglected. Many models have included $c_{\mathrm{p,cake}}$ and $\Lambda_{\mathrm{p,cake}}$ in their model equations without explicitly stating the values used for these parameters [33, 39, 42, 50, 51, 135, 267]. The values of specific heat capacities of soot deposits and the thermal conductivity of soot cake layers are summarised in Table 1.

Literature values for the specific heat capacity of the soot cake agree reasonably and are comparable to that of the filter wall substrate material (1120 J/kgK for cordierite, 800

Table 1: *Summary of thermal properties of soot deposits from literature.*

Reference	Specific heat capacity (J/kgK)	Thermal conductivity (W/mK)
Zheng and Keith [271]	1510	0.84
Depcik and Assanis [44]	889	2
Meng et al. [149]	1500	0.1
Di Sarli and Di Benedetto [46]	900	10

J/kgK for SiC [149]). On the other hand, values of thermal conductivities span over two orders of magnitude. If the thermal conductivities of the soot cake and the filter wall are vastly different, the assumption that the soot cake and the filter wall are at local thermal equilibrium breaks down as heat will dissipate at different speeds in the soot cake and the filter wall.

Since the soot cake layer is porous, its thermal conductivity would be a function of its porosity [72]

$$\Lambda_{\text{cake}} = \varepsilon\Lambda_{\text{g}} + (1-\varepsilon)\,\Lambda_{\text{soot}}. \tag{86}$$

Assuming for a moment that pure soot has the same thermal properties as black carbon (1.6 W/mK), the thermal conductivity of a soot cake with 97% porosity would be 0.108 W/mK [72]. This suggested that the values of thermal conductivities assumed by Depcik and Assanis [44] and Di Sarli and Di Benedetto [46] are unlikely to be realistic.

So far there has been little attention to how soot deposits can impact heat transfer as it is less influential than other factors such as the operating condition and substrate properties. This is reflected in literature modelling studies where very different values have been used for the thermal properties of soot deposits and yet all manage to get good agreement with experimental data. This is reasonable since the mass of soot deposits in particulate filters is small with respect to the filter substrate, and it is not an excellent heat insulator nor a huge heat sink.

3 Modelling regeneration

3.1 Reaction pathways

The major oxidants of soot deposits in particulate filters are O_2 and NO_2 [195]. Soot oxidation by NO is usually neglected as NO is a weaker oxidant than O_2 under the expected operating conditions of particulate filters [121]. Regeneration of soot by O_2 and NO_2 can be expressed as [120]

$$\mathrm{C} + \Upsilon_1\mathrm{O_2} \longrightarrow (2\Upsilon_1 - 1)\,\mathrm{CO_2} + (2 - 2\Upsilon_1)\,\mathrm{CO}, \tag{87}$$

$$\mathrm{C} + \Upsilon_2\mathrm{NO_2} \longrightarrow \Upsilon_2\mathrm{NO} + (\Upsilon_2 - 1)\,\mathrm{CO_2} + (2 - \Upsilon_2)\,\mathrm{CO}, \tag{88}$$

where Υ_1 and Υ_2 are stoichiometric coefficients of the regeneration reactions. Soot is usually represented as pure carbon (C) in regeneration reactions [91]. The formation of N_2 from NO_2-assisted soot oxidation has also been considered in the literature [196]. When both NO_2 and O_2 are available in the exhaust, a synergistic effect has been observed [81]. The overall rate of soot oxidation is higher than the sum of O_2-only oxidation and NO_2-only oxidation activities, which suggests the existence of NO_2-assisted O_2 oxidations [195]

$$C + NO_2 + \frac{1}{2}O_2 \longrightarrow CO_2 + NO, \tag{89}$$

$$C + \frac{1}{2}O_2 \xrightarrow{NO_2} CO. \tag{90}$$

Pyrolysis may happen in the absence of oxygen. This commonly occurs in gasoline engines [24]. Mitsouridis et al. [155] considered the formation of CO from soot and CO_2

$$C + CO_2 \longrightarrow 2CO. \tag{91}$$

This reaction is limited by thermodynamics at low temperatures and is therefore not expected to occur in DPFs. Nonetheless, it may be appreciable in GPFs since the exhaust temperature is generally higher in GPFs than in DPFs [18].

The performance of regeneration can be improved by coating the particulate filter with oxidation catalysts. First, oxidation catalysts can produce NO_2 from NO to support regeneration [259]. Second, catalysts can greatly improve CO_2 selectivity over CO [47, 170]by oxidising CO during regeneration [173]. Third, the presence of catalysts can lower the light-off temperature of regeneration reactions [82, 174]. This can reduce the peak temperature during active regeneration [46], which in turn reduces the chance of filter failure due to thermal-induced stress.

The soot-catalyst contact can influence the regeneration performance of the catalyst [15]. It is strongly dependent on the morphology of the catalyst and support [5, 150]. The morphology is particularly important for soot oxidation since trapped particles are immobile [4, 16]. As most of the soot cake is not touching the filter wall, only thermal (uncatalysed) regeneration is appreciable in the soot cake [45]. Nonetheless, the catalyst can improve regeneration of the soot cake by producing oxidants such as NO_2 that can diffuse towards the soot cake. The dependence of catalysed regeneration on soot-catalyst contact conditions can also vary with temperature. Piumetti et al. [172] found that the impact of the soot-catalyst condition on catalysed soot oxidation is more significant at high temperatures for self-prepared ceria-based catalysts. The catalysed soot oxidation can be insensitive to the surface contact condition at low temperature if the surface of the catalyst is masked by adsorbed species.

Other species in the exhaust can also affect regeneration reactions. The presence of H_2O and CO_2 has been observed to slightly delay soot ignition [170]. On the other hand, H_2O has also been reported to catalyse NO_2 regeneration [82]. In addition, O_2-only soot oxidation may be catalysed by water vapour between 450 °C and 600 °C [273].

It should be noted that soot does not only contain elemental carbon. Whilst catalyst may be active for the oxidation of elemental carbon in soot particles, it may not be active for the oxidation of adsorbed polyaromatics [182]. If this is the case, polyaromatics may be released into the atmosphere during regeneration.

3.2 Rate equations

The rates of regeneration reactions depend on the filter temperature, the concentration of gaseous reactants, the properties of the particles, and the catalysts involved. A general equation to describe the rate of regeneration reaction is

$$r = -\frac{\mathrm{d}m_\mathrm{p}}{\mathrm{d}t} = kG\Gamma, \tag{92}$$

where k is the reaction rate constant, G is a function of the concentrations of the gaseous reactants and Γ is a function of particle state, usually its mass. It should be noted that the rate of regeneration is often presented as the rate of oxidant consumption instead of the rate of soot mass consumption. These rates may be interconverted based on the stoichiometry of regeneration reactions.

Arrhenius-type equations are frequently used to describe reaction rate constants [43, 243, 244]

$$k = AT^b \exp\left(-\frac{E}{RT}\right), \tag{93}$$

where A is the pre-exponential constant, b is the temperature exponent and E is the activation energy of the reaction. The temperature exponent b is often assumed to be 0 [10, 57, 227] or 1 [51, 95, 180, 268] before any calibration. Catalysed and thermal regeneration are often modelled as independent reactions with different rate parameters [46, 180, 214].

G in eq. (92) is usually a function of concentrations of gaseous oxidants [10, 95, 111, 212, 268]. Since O_2 and NO_2 are the most common oxidants for filter regeneration, the following expressions can cover most variations of G used in the literature

$$G = c_{\mathrm{O_2}}^{q_{\mathrm{O_2}}} c_{\mathrm{NO_2}}^{q_{\mathrm{NO_2}}}, \tag{94}$$

where c is molar concentration and q is the reaction order of the oxidants. G can also be defined in terms of partial pressures, mass fractions or mole fractions of oxidants [135, 214, 242]. Regeneration reactions are often assumed to be first-order in the involved oxidants [43, 51, 111, 138, 243]. However, experimental studies have shown that the reaction order of O_2 regeneration ranges between 0.8 to 1 in the absence of catalysts [23, 41, 160]. This implies that the rate of oxidation is determined by the adsorption of oxygen on active carbon sites [210]. The presence of a catalytic coating in the filter can affect the reaction orders with respect to oxidants since the rate-determining step is different. For example, the reaction order of O_2 in a regeneration reaction catalysed by a

Pt/Pd catalyst is found to be 0.3 [214]. It should be noted that the influences of catalyst on different regeneration pathways are different *e.g.* the reaction order of NO_2 regeneration remains 0.6 regardless of the presence of the Pt/Pd catalyst [214].

Chemical species other than the oxidants can affect the reaction rates as well. Schejbal et al. [196] used the following expression for NO_2-only regeneration to include the catalytic effect of water vapour

$$G = Y_{\mathrm{NO_2}}^{q_{\mathrm{NO_2}}} \left(1 + C Y_{\mathrm{H_2O}}^{q_{\mathrm{H_2O}}}\right), \tag{95}$$

where Y is the mass fraction. Parameter C and reaction orders q require calibration.

The simplest and the most widely used expression of P in eq. (92) is the n^{th}-order model [10, 23, 95, 111, 134, 180]

$$\Gamma = m_{\mathrm{p}}^{q_{\mathrm{p}}}. \tag{96}$$

If the oxidation occurs solely on the surface of the particle, the rate of the regeneration should be proportional to the surface area of the particles and hence the reaction order $q_{\mathrm{p}} = \frac{2}{3}$. On the other hand, $q_{\mathrm{p}} = 1$ implies internal burning and hence the rate of regeneration is proportional to the mass of the particles [227]. Kinetic studies sometimes include the initial mass of soot into the rate equation [41, 160]

$$\Gamma = m_{\mathrm{p0}} \left(\frac{m_{\mathrm{p}}}{m_{\mathrm{p0}}}\right)^{q_{\mathrm{p}}} = m_{\mathrm{p0}}^{1-q_{\mathrm{p}}} m_{\mathrm{p}}^{q_{\mathrm{p}}}. \tag{97}$$

It will be difficult to integrate such rate equations with simulations of continuously regenerating filters since the history of trapped particles needs to be tracked to compute the rate of regeneration.

Some authors expressed the formation of CO and CO_2 as separate reactions with their own rate parameters. Alternatively, the temperature-dependence of the CO selectivity Ψ_{CO} may be modelled as such [43]

$$\begin{aligned}
\dot{c}_{\mathrm{CO}} &= \Psi_{\mathrm{CO}} k c_{\mathrm{O_2}}, \\
\dot{c}_{\mathrm{CO_2}} &= \left(1 - \Psi_{\mathrm{CO}}\right) k c_{\mathrm{O_2}}, \\
k &= A \exp\left(-\frac{E}{RT}\right), \\
\frac{1}{\Psi_{\mathrm{CO}}} &= 1 + A' \exp\left(\frac{E'}{RT}\right) c_{\mathrm{O_2}}^{q'},
\end{aligned} \tag{98}$$

where $\dot{c}$ is the rate of production of chemical species in molar concentration. The Arrhenius parameters of the CO selectivity A', E' and q' will need to be calibrated.

Once the expression of reaction rate is chosen, kinetic parameters are typically calibrated based on experimental data. Engine bench tests should be used to determine soot oxidation kinetics to ensure that experimental results are obtained with real soot under realistic

operating conditions [2], although thermogravimetric analysis (TGA) is also used frequently. The importance of the methodology on the rate parameters was highlighted by Bogarra et al. [23] who found that TGA with a heat ramp and isothermal TGA gave different estimates of rate parameters. It should also be noted that Printex-U is often used as a surrogate of diesel soot with high elemental carbon content in kinetics tests [24]. Whilst Printex-U oxidises similarly to ash-free GDI soot [53], its oxidation behaviour does not always represent real diesel soot [258].

The reactive surface area of soot particles plays a role in controlling the rate of oxidation. Many models assume a fixed specific surface area for the soot cake during regeneration [39, 42, 51, 135, 139, 149, 243, 267]. This is counter-intuitive as we expect particles to become smaller as it burns and hence an increase in the specific surface area [248]. This is expected to speed up combustion because of the increasing surface-volume ratio [134].

The change in surface area of soot particles is dependent on the combustion mode of the particles. Different burning modes were observed when soot particles were oxidised by different oxidants. When only O_2 is present, significant internal burning can occur within soot particles [205]. This is due to the preferential removal of amorphous carbon over less reactive graphitic carbon. On the other hand, NO_2 has shown no preference. As a result, a shrinking sphere model is adequate to describe the change in specific surface area during soot oxidation by NO_2. When both NO_2 and O_2 are present, the degree of internal burning is greatly suppressed due to cooperative oxidation (eq. (89) and (90)). Whether internal burning occurs also depends on the soot composition. Jung et al. [84] found that acetylene soot is impermeable to O_2 and hence combustion will only occur on the soot surface.

Macián et al. [137] considered the mass transport phenomena within soot aggregates during regeneration. Diffusion of oxidants within the soot aggregate as well as the adsorption of oxidants onto the reactive sites are considered. The impact of the adsorption and reaction of gaseous reactants on the rate of regeneration is described by the Langmuir isotherm

$$G = \frac{K_\mathrm{g} p_\mathrm{g}}{1 + K_\mathrm{g} p_\mathrm{g}}, \tag{99}$$

where p_g is the partial pressure of a gaseous reactant. The equilibrium constant of adsorption K_g is described by

$$K_\mathrm{g} = A \exp\left(-\frac{\Delta H_\mathrm{ads}}{RT}\right), \tag{100}$$

where ΔH_ads is the adsorption enthalpy.

The reaction rate is set to be proportional to the total reactive specific surface area of soot particles $S_\mathrm{p,r}$

$$S_\mathrm{p,r} = S_\mathrm{p,ext} + \gamma_\mathrm{p} S_\mathrm{p,int}, \tag{101}$$

where $S_\mathrm{p,ext}$ and $S_\mathrm{p,int}$ are the external and internal specific surface area of soot deposits. The external specific surface area was measured by Kandas et al. [90] experimentally. The internal specific surface area was assumed to be the uncovered area after removal of SOF.

The internal effectiveness factor γ_p was included to account for the effect of internal pore diffusion

$$\gamma_p = \frac{1}{\phi}\left(\frac{1}{\tanh 3\phi} - \frac{1}{\phi}\right), \tag{102}$$

The Thiele modulus ϕ for adsorption-reaction on spherical soot primary particles is [78]

$$\phi = \frac{d_{pri}}{6}\sqrt{\frac{S_{p,int} k \Upsilon}{2D'_{m,Kn}(K_g p_g - \ln[1+K_g p_g])}}\frac{K_g p_g}{1+K_g p_g}, \tag{103}$$

where Υ is the stoichiometric factor in eqs. (87) and $D'_{m,Kn}$ is the adjusted Knudsen diffusivity calculated using the Salatino's procedure [189]

$$D'_{m,Kn} = D_{m,Kn}\exp\left(-\frac{E_{ads}}{RT}\right), \tag{104}$$

where E_{ads} is the activation energy of the adsorption step. Using this model, Macián et al. [137] found that the equivalent reaction order of NO_2 is around 0.3 and 0.4 in typical passive regeneration conditions, whereas the equivalent reaction order of O_2 varied during the course of regeneration.

The evolution of specific surface area during regeneration may be modelled as [160]

$$S_p = S_{p0}(1-\zeta)\sqrt{1-\Pi\ln(1-\zeta)}, \tag{105}$$

where S_{p0} is the initial specific surface area and ζ is the conversion of soot. The structural factor Π describes the initial pore structure within soot aggregates [220]. According to this equation, the surface area will increase initially due to pore growth. As regeneration continues, the surface area will reach a maximum and then decrease as the remaining soot collapses into itself.

Some works have found that there is no correlation between the specific surface area and soot reactivity [53, 257]. Zygogianni et al. [274] found that structural differences of soot (*e.g.* the size of crystallite) and the composition of particles are more correlated to the soot oxidation reactivity. For example, a higher degree of graphitisation (more ordered structure) leads to less reactive soot [186]. However, most models neglect the difference in nanostructure of soot particles and treated them as pure carbon species [7, 33, 42]. Kastrinaki et al. [95] proposed a multi-population kinetics to describe soot oxidation behaviour. The soot samples were divided into three populations with their own reaction rate constants. The authors attributed the difference in soot oxidation behaviour to distinct families of surface oxygen complexes (SOC) formed on the carbon surface of each population.

Furthermore, real engine soot also contains a soluble organic fraction (SOF) and ash. Soot oxidation activity may be enhanced by higher soluble organic fraction (SOF) content and weakly bonded carbon (WBC) content [36]. Removal of SOF can lead to a rapid

increase in the specific surface area of soot particles at the early stage of oxidation [213]. Depending on the ash composition, soot oxidation activity may be enhanced or reduced [57]. Ash particles may act as oxygen carrier which improves soot oxidation [49]. On the other hand, ash originated from phosphate-doped fuel was found to inhibit soot oxidation [37].

Choi and Seong [36] proposed a global soot oxidation kinetic scheme that considers the impact of ash and SOF/WBC content in GDI soot. The overall rate is

$$\hat{r} = \frac{\mathrm{d}\zeta}{\mathrm{d}t} = \frac{m_{\mathrm{SW},0}}{m_{\mathrm{soot},0}}\hat{r}_{\mathrm{SW}} + \frac{m_{\mathrm{C},0}}{m_{\mathrm{soot},0}}\hat{r}_{\mathrm{C}}, \tag{106}$$

where ζ is the overall conversion and $\hat{r}$ is a dimensionless reaction rate. The subscripts SW and C refer to SOF/WBC and carbon respectively. The rate of SOF/WBC oxidation is

$$\hat{r}_{\mathrm{SW}} = \frac{\mathrm{d}\zeta_{\mathrm{SW}}}{\mathrm{d}t} = A_{\mathrm{SW}} \exp\left(-\frac{E_{\mathrm{SW}}}{RT}\right)(1-\zeta_{\mathrm{SW}})^{q_{\mathrm{SW}}}, \tag{107}$$

where ζ_{SW} is the degree of conversion of SOF-WBC

$$\zeta_{\mathrm{SW}} = 1 - \frac{m_{\mathrm{SW}}}{m_{\mathrm{SW},0}}. \tag{108}$$

The rate of carbon oxidation r_{C} is

$$\hat{r}_{\mathrm{C}} = \frac{\mathrm{d}\zeta_{\mathrm{C}}}{\mathrm{d}t} = A_{\mathrm{C}} \exp\left(-\frac{E_{\mathrm{C}}}{RT}\right)(1-\zeta_{\mathrm{C}})^{q_{\mathrm{C}}} + C_1 \exp(C_2 T) Y_{\mathrm{ash,O}}, \tag{109}$$

where C_1 and C_2 are tunable parameters of ash-assisted soot oxidation, $Y_{\mathrm{ash,O}}$ is the fraction of oxidation-derived ash and ζ_{C} is the degree of conversion of carbon

$$\zeta_{\mathrm{C}} = 1 - \frac{m_{\mathrm{C}}}{m_{\mathrm{C},0}}. \tag{110}$$

Ash may be deliberately introduced by doping the fuel with fuel-borne catalyst (FBC) metal additives because this can reduce the temperature at which soot burns off in the filter [211]. FBC is expected to perform better than the catalytic coating on filter walls because of close contact between ash and soot especially in the soot cake layer [37]. Ash accumulates in the filter while soot burns off.

Easter [53] observed a three-stage oxidation behaviour for ash-rich GDI soot. This was attributed to the change in soot-ash contact during oxidation. The proposed mechanism is shown in Fig. 12.

Initially, soot and ash are in close contact and the rate of oxidation is at its highest. As regeneration continues, the contact between soot and ash is lost, result in a lower oxidation rate. The rate of oxidation is recovered slightly towards the end of the oxidation, as contact

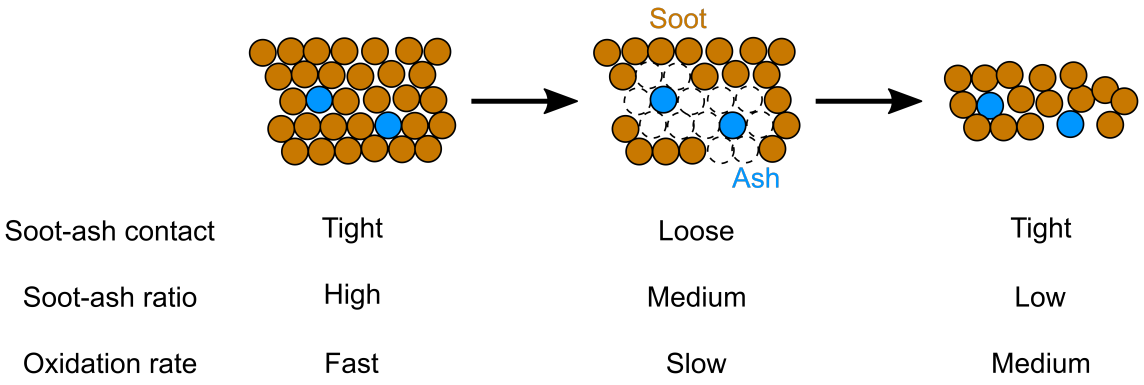

Figure 12: *Three-stage oxidation behaviour of ash-containing GDI soot.*

between remaining soot and ash are re-established since the majority of soot is already consumed.

Although the contact condition between soot and catalyst can affect the regeneration performance significantly [15], quantification of the impact of soot-catalyst contact on regeneration is rarely seen in literature filter models. Konstandopoulos et al. [111] studied the effect of the size of milled catalyst particles on their soot oxidation ability using the multi-population model [95]. They found that reducing the size of ceria catalyst particles can increase the oxidation rate of highly and moderately reactive soot (Activation energies of 120 kJ/mol and 180 kJ/mol respectively), whereas the oxidation of the least reactive soot (240 kJ/mol) was insensitive to the size of catalyst particles. Note that Konstandopoulos et al. [111] have kept the activation energies of soot populations constant regardless of the presence of a catalyst. Other authors often use lower activation energy for catalysed regeneration pathways with respect to thermal regeneration pathways [45].

Catalysts within the filter can assist NO_2 regeneration by producing NO_2 from NO, although the rate of NO_2 soot oxidation is not promoted by catalysts [196]. If NO_2 is being produced within catalysed filter walls, it can aid oxidation of the soot cake layer. NO_2 may reach the soot cake layer via back-diffusion [222]. In order to capture the concentration gradient across the soot cake and the filter wall, eq. (77) would need to be solved in channel-scale models. The soot cake layer would need to be discretised in this case to resolve the concentration gradient of NO_2 across the soot cake[243]. On the other hand, competition for NO_2 can occur between passive regeneration and SCR reactions in SCR-coated filters [239]. SCR reactions are more competitive for NO_2 than soot oxidation [140], although at high temperatures, soot oxidation can outweigh SCR reactions [197]. Furthermore, NH_3 may block free-edge sites on carbon particles. This phenomenon has been modelled by Trandafilović et al. [220].

It is shown in this section that the rates of regeneration reactions are influenced by many factors, ranging from the nanostructure of soot deposits, the surface of soot deposits, their "non-soot" components and the presence of catalysts. Many researchers have developed models to quantify the impact of these factors, but it remains a challenging task to combine these developments into a coherent regeneration model that can capture the effect of all factors mentioned above.

3.3 Evolution of particle deposit

The changes of soot cake properties during regeneration are often ignored in modelling studies [135]. Many filter modelling studies have assumed that the packing density of the soot cake layer remains constant during regeneration [33, 39, 42, 131, 149, 243]. The thickness of the soot cake w_{cake} under O_2 regeneration may be obtained by solving the following equation [135]

$$\frac{\mathrm{d}w_{\text{cake}}}{\mathrm{d}t} = -\frac{v\rho_{\text{g}}Y_{\text{O}_2,0}}{\Upsilon\rho_{\text{cake}}}\left(1-\exp\left[-\frac{S_{\text{p}}kw_{\text{cake}}}{v}\right]\right), \tag{111}$$

where v is the through-wall gas flow velocity, ρ_{g} is the gas density, $Y_{\text{O}_2,0}$ is the mass fraction of oxygen at the top of the soot cake, Υ is the stoichiometric coefficient of O_2, S_{p} is the specific surface area of the soot cake layer and k is the reaction rate constant described by an Arrhenius-type equation (eq. (93)).

Kostoglou and Konstandopoulos [114] examined how assumptions about the microstructure of the soot cake can affect the calibration and prediction of the regeneration process. Four models were considered in their work and are shown in Fig. 13.

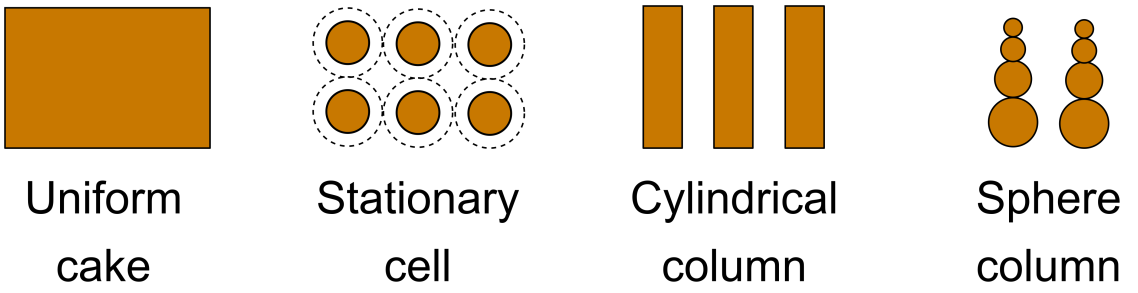

Figure 13: *Conceptual regeneration models to describe the change in packing density and surface area of soot cakes during regeneration [114].*

The packing density and the specific surface area of the soot cake are the two relevant parameters during the regeneration process [114]. The first model in Fig. 13 assumes constant cake density and specific surface throughout regeneration. The second model treats the soot cake as spherical particles held in stationary cells that all burn at the same rate. The third model treats the soot cake as cylindrical columns with the same diameters as the primary soot particles. The fourth model treats the soot cake as columns of spherical particles, where the movement of particles and hence a change in cake thickness is considered, in contrast to the second model. The fourth model was used to fit against experimental data and good agreement was found. The authors suggested that future soot cake models should track the evolution of both the cake density and the cake thickness.

However, the change in the microstructure of the soot cake layer during regeneration has been experimentally observed to be more complicated than cases considered by Kostoglou and Konstandopoulos [114]. Fig. 14 shows a conceptual model proposed by Toops et al. [219] who studied the evolution of the soot cake layer during active regeneration using neutron tomography.

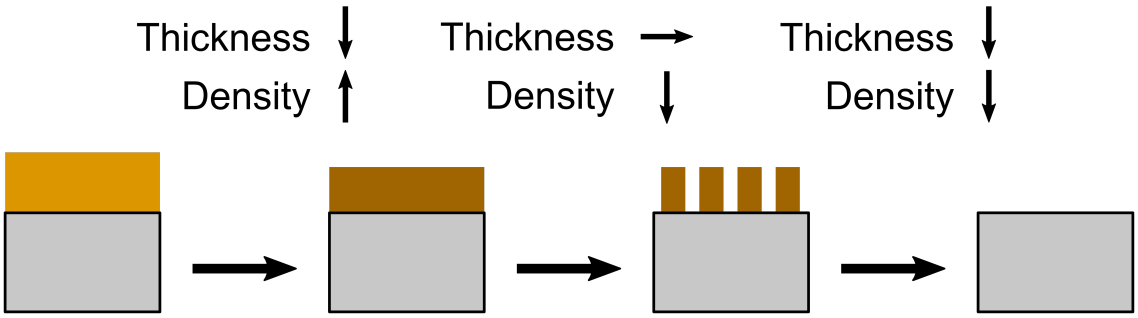

Figure 14: *Conceptual model of soot cake evolution during active regeneration based on neutron tomography observations [219].*

During the first stage of regeneration, the soot cake becomes thinner and more compact while maintaining its structural uniformity. At the second stage, the soot cake becomes more porous without significant change in the cake thickness. Many irregular scallops were observed through SEM during this stage [49]. A similar phenomenon was also observed for GDI soot [53]. The formation of these scallops may be driven by the high attractive force between soot deposits, which is stronger than the attractive forces between soot and filter wall substrate [86]. The packing density and the thickness of the soot cake continue to decrease gradually after the second stage until the soot cake is completely oxidised.

The rate of pressure drop reduction was observed to be higher during the second stage of active regeneration than the first and the third stage [38, 49]. This implies an increase in the permeability of the soot cake. Mahadevan et al. [139] modelled the increase in soot cake permeability using an analogy with cracked concrete [171]. The cracks in concrete allow gas to flow through with little resistance which results in an increase in the permeability. In the case of the soot cake, the "cracks" are the gaps between soot scallops formed during the second stage of active regeneration. The permeability of the damaged soot cake layer is modelled as

$$\kappa_{\text{cake}} = \kappa_{\text{cake},0} \exp\left[\left(C_1 \zeta_{\text{d}}\right)^{C_2}\right], \tag{112}$$

where C_1 and C_2 are calibrated parameters. The damage variable ζ_{d} is defined as

$$\zeta_{\text{d}} = 1 - \frac{m_{\text{cake}}}{m_{\text{cake},0}}. \tag{113}$$

In contrast to active regeneration, the combined permeability of the clogged wall and the soot cake is not altered significantly by passive regeneration [61]. The bottom of the soot cake layer has the highest regeneration rate during passive regeneration of catalysed filters since NO_2 is generated in the catalysed wall and then diffuses back to the soot cake. The soot cake has been discretised into multiple layers in filter models in order to resolve the concentration gradient within the soot cake. The model proposed by Wurzenberger et al. [244] used a fixed spatial grid to describe the soot cake as shown in Fig. 15.

A mobility term for soot mass is needed to describe the shrinking of the cake layer during

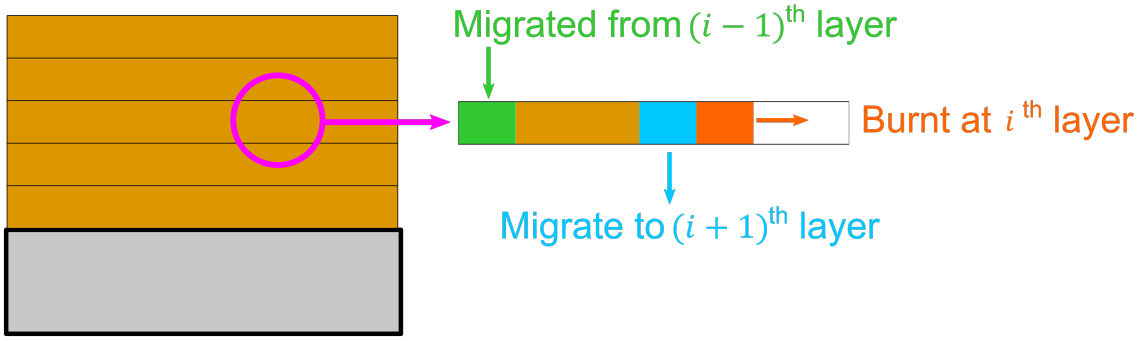

Figure 15: *The fixed spatial discretisation of the soot cake proposed by Wurzenberger et al. [244]. A mobility term is introduced to describe the movement of soot due to regeneration.*

regeneration. The rate of migration of soot is expressed as

$$\dot{m}_{\mathrm{mob},i} = C_{\mathrm{mob}} \alpha_{\mathrm{soot},i} \varepsilon_{i+1}, \tag{114}$$

were C_{mob} is a mobility factor, $\alpha_{\mathrm{soot},i}$ is the volume fraction of soot of the i^{th} layer and ε_{i+1} is the void fraction of the $(i+1)^{\mathrm{th}}$ layer that is below the i^{th} layer. On the other hand, Haralampous and Koltsakis [74] discretised the soot cake into a fixed number of slabs. The soot cake is re-divided into elements of equal mass at every time step. Whilst a moving grid approach can reduce numerical diffusion [241], this model does not consider the local variation of soot cake properties such as the porosity, unlike the model used by Wurzenberger et al. [244].

Sometimes the soot cake may collapse during regeneration and leads to the formation of a mid-channel soot plug. This will lead to a rapid increase in pressure drop. Since the pressure drop of the filter is frequently used to estimate the soot load of the filter by on-board controls [230], the formation of mid-channel soot plug will lead to malfunction of the on-board control. Fukui et al. [63] found that this phenomenon can be invoked with intermittent increases of flow rate and engine torque. A later study by Kim et al. [96] showed that three factors would be needed to trigger the collapse of the soot cake layer. First, passive regeneration by in-situ NO_2 generation is needed to create a gap between the soot cake and the filter wall. Second, water needs to adsorb onto the soot cake and create a concave shape in the soot. Finally, the collapse of the soot cake layer is triggered by a cold start with heavy acceleration. To the best of our knowledge, this phenomenon has yet to be included in the after treatment models reported in the literature.

Various experimental studies have reported surges in the concentration of particle being released from regenerating filters [12]. Large (80 nm) solid particles have been observed to be released from particulate filters during active regeneration [186]. They are likely to be unfiltered particles that pass straight through the filter due to a reduction in the filtration efficiency after regeneration [246]. Many sub-23 nm particles have also been observed [27]. They are composed of semi-volatile material since they are not detected under high dilution ratio conditions [247]. They may be sulphuric acid particles desorbed from the catalyst [185, 246]. Passively regenerating filters were found to have lower

particle emission levels than actively regenerating filters [207] since the presence of soot cake can limit the reduction in filtration efficiency.

The increased emission of solid particles during regeneration have been modelled in the literature. Lao et al. [119] has proposed an empirical model to describe the reduction in filtration efficiency of the soot cake due to non-uniform regeneration using a sigmoid function

$$E_{\text{cake}} = \frac{\exp\left[C_1\left(\frac{m_{\text{cake}}}{m_{\text{cake},0}} - C_2\right)\right]}{\exp\left[C_1\left(\frac{m_{\text{cake}}}{m_{\text{cake},0}} - C_2\right)\right] + 1}, \tag{115}$$

where $m_{\text{cake},0}$ is the initial mass of the soot cake at the start of regeneration, C_1 and C_2 are numerical parameters that were calibrated based on the experimental filtration efficiency measurements during active regeneration. A reduction in the wall filtration efficiency at elevated temperatures was also discovered during the model calibration process. This reduction in filtration efficiency cannot be explained by the removal of trapped particles. The cause of the reduction in filtration efficiency was not identified and remains an open question.

Tan et al. [214] simulated the emission of particles during the passive regeneration of a catalysed filter. The leaked particles were hypothesised to be fragments of soot particles produced during catalytic oxidation in the filter wall. A correction factor was applied to the combined single collector efficiency predicted by the model (η in eq. (10)). The correction factor C_{frag} was made to be a function of the partition coefficient Φ (eq. (56))

$$C_{\text{frag}} = \begin{cases} 1 & \Phi < \Phi_{\text{low}} \\ 1 - (1 - C_{\text{frag,min}})\frac{\Phi - \Phi_{\text{low}}}{\Phi_{\text{high}} - \Phi_{\text{low}}} & \Phi_{\text{low}} \leq \Phi \leq \Phi_{\text{high}} \\ \delta & \Phi > \Phi_{\text{high}}, \end{cases} \tag{116}$$

where Φ_{high} and Φ_{low} are the limiting partition coefficients chosen by Tan et al. [214]. The minimum correction factor $C_{\text{frag,min}}$ describes the level of fragmentation and is a function of particle size and operating condition. Whilst the model is largely empirical, it allows quantification of the factor C_{frag} and can help further the development of a more physical model.

Predicting the release of particles formed from semi-volatile material during regeneration is difficult because they are difficult to measure [188]. The state of the semi-volatile particles is strongly dependent on the gas phase composition. Significant losses of semi-volatile particles can occur within the measuring system due to diffusional losses of particles to the walls of the measurement device. Lee et al. [124] presented a model that considers sulphates and SOF particles in addition to solid soot particles. The model was shown to be successful in describing the evolution of the particle population in both the engine and in the particle sampling system. The release of semi-volatile particles during filter regeneration may be captured if this type of modelling approach is integrated with existing filter models.

4 Modelling ash accumulation and migration

4.1 Formation mechanisms

Ash are formed from incombustible metallic residues that remains in particulate filters after regeneration. The ash can be distributed within the filter wall, form a layer on the filter wall and can form plugs at the end of inlet channels. In some cases, ash plugs can also be found in the middle of inlet channels. These are illustrated in Fig. 16.

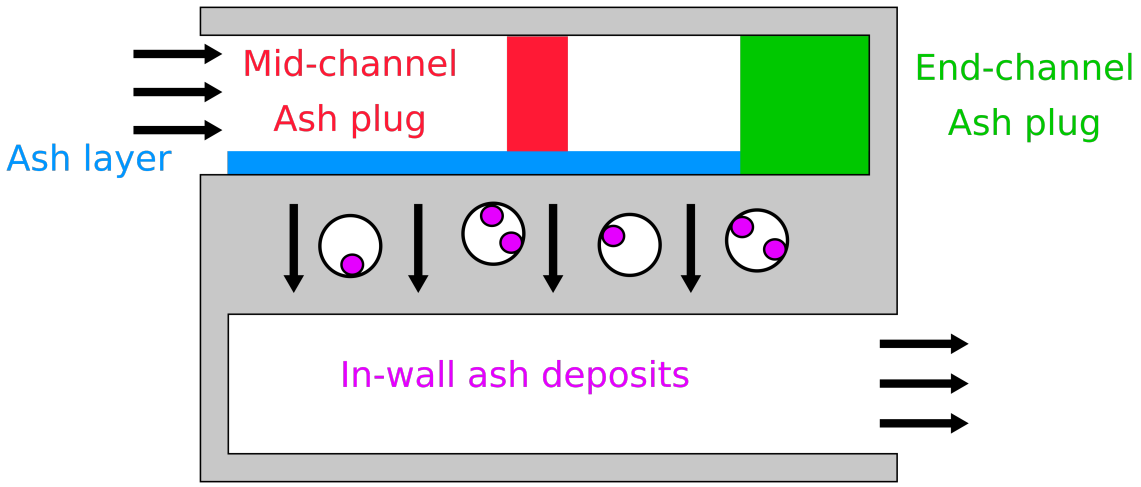

Figure 16: *Different possible forms of ash deposits in a particulate filter.*

The pattern of ash deposition is closely related to the regeneration process, the pattern is not dictated by whether the regeneration process is active or passive [48]. A passively regenerated filter with high NO_x content and high temperature can have a similar ash deposition pattern to actively regenerated filters.

Deep-bed ash deposits are formed by the regeneration of ash-containing soot particles that are trapped within the walls of a filter [48]. Whilst most experimental studies have shown that ash usually only deposits on the surface of filter walls [40, 187], there is experimental evidence of deep penetration of ash into filter walls ($\geq$ 50% of the wall thickness [199]). Kamp et al. [87] found that ash deposits penetrated the filter walls of sintered metal fibre filters further if the filter undergoes active regeneration instead of passive regeneration. This is because the persistent presence of the soot cake layer during passive regeneration acted as an effective barrier for ash-bearing soot to deposit within the filter wall.

The ash layer and the ash plug are formed from the combustion of the soot cake layer. The ash plug is formed from soot fragments produced during regeneration which migrate towards the back of the inlet channels [40]. An optical study conducted by Matsuno and Kitamura [144] found that lumps of soot can migrate towards the end of inlet channels during active regeneration. Whether ash plugs form at the early stages of ash accumulation depends on the initial amount of soot [144]. Once the ash layer is established, it makes soot migration during active regeneration occur more readily [144]. Shearing flow can also cause ash to migrate towards the back of inlet channels. Whether ash particles are re-entrained into the gas flow depends on their size [237]. Particles with diameters around

100 microns are the easiest to be re-entrained [203]. Larger particles are difficult to be re-entrained due to their inertia and smaller particles are difficult to be re-entrained due to their smaller surfaces [235].

The size of ash particles depends on the regeneration conditions. Low regeneration temperature, low soot loading and high soot-to-ash ratio before regeneration can lead to the formation of small, densely packed ash particles [235]. These ash particles may grow by sintering with temperature excursion and become more sticky [191, 265]. Bagi et al. [9] optically observed the densification and sintering of ash precursor remained from soot oxidation. As ash particles sinter and increase in size, they may be more susceptible to shearing flow which can lead to formation of the ash plugs in the mid-channel [89].

Modelling the formation of ash is a challenging task. The following three aspects need to be considered in modelling ash deposition in particulate filters:

1. Movement of ash fractions as part of soot particles due to filtration and regeneration-induced migration.
2. Movement of ash deposits due to flow-induced migration.
3. Change in size and structure of ash deposits due to agglomeration and sintering at high temperature.

The filtration process can be modelled as described in Section 2. Additional variables such as ash mass fraction within soot particles need to be tracked by the filter model in order to simulate the deposition of ash contained within soot particles. The migration of soot cake during regeneration can be described by the following equation [43]

$$\frac{\partial w_{\text{cake}}}{\partial t} + C_{\text{mob}} \frac{\partial (v w_{\text{cake}})}{\partial z} = 0, \tag{117}$$

where w_{cake} is the (local) thickness of the soot cake, v is the axial gas flow velocity and C_{mob} is the mobility constant. Deng et al. [43] did not specify how the mobility constant may be calibrated. Recent work by Koltsakis et al. [101] has considered the detachment and re-deposition of the soot cake due to the shear stress experienced by the soot cake. The shear stress ι can be calculated [193]

$$\iota = \frac{F_{\text{f}} \mu v}{4(d_{\text{c}} - 2w_{\text{cake}} - 2w_{\text{ash}})}, \tag{118}$$

where F_{f} is the laminar channel flow friction factor, μ is the dynamic viscosity, v is the local axial gas flow velocity and $(d_{\text{c}} - 2w_{\text{cake}} - 2w_{\text{ash}})$ is the channel diameter of the open cross-section available for gas flow after accounting for the thicknesses of the soot cake and the ash layer. Soot fragments will detach when the shear stress exceeds a critical value. The detached fragment will flow along the inlet channel until it reattaches to the soot cake. This happens in the model if the local shear stress drops below critical reattachment shear stress. No explicit formula or values regarding the critical shear stresses were reported by Koltsakis et al. [101]. The critical shear stress is expected to be a function

of the size of the soot fragment and its adhesiveness to the soot cake/filter wall surface. Although the latter could be measured by atomic force microscopy (AFM) [86], no numerical model has been proposed to predict the size of the soot fragment produced during the combustion of a soot cake layer. Since the detachment of soot fragments depends on adhesion with the surface, the likelihood of soot migration will change depending on whether the ash layer is present. This is in agreement with experimental observations made by Matsuno and Kitamura [144].

In addition to the regeneration-induced transport, migration of ash due to shearing flow on the ash layer has been modelled by Konstandopoulos et al. [109]. The governing equations for the ash mass fraction suspended in the gas phase Y_{ash} and the ash layer thickness w_{ash} are

$$\rho_{\text{g}} v \frac{dY_{\text{ash}}}{dz} = \frac{4}{d_{\text{ch}}} J_{\text{ash}} - \frac{4}{d_{\text{ch}}} \rho_{\text{g}} v_{\text{w}} Y_{\text{ash}}, \tag{119}$$

$$\rho_{\text{g}} \frac{\partial w_{\text{ash}}}{\partial t} = \rho_{\text{g}} v_{\text{w}} Y_{\text{ash}} - J_{\text{ash}}, \tag{120}$$

where v_{w} is the through-wall gas flow velocity. The ash re-entrainment flux J_{ash} takes a non-zero pre-set value J_0 if the local shear stress exceeded the critical detachment shear stress and the local temperature is lower than a critical value. The temperature constraint attempts to capture the impact of the ash stickiness. In the model proposed by Koltsakis et al. [101], the migration of the ash layer can be inhibited if a soot cake layer is present on top of the ash layer, subject to a critical soot cake mass constraint. The critical detachment shear stress of the ash layer is a function of the local velocity and the local ash agglomerate size. The following expression was used by Koltsakis et al. [101] to describe the rate of agglomeration of primary ash particles r_{agglo}

$$r_{\text{agglo}} = C_1 \exp\left(-\frac{C_2}{T}\right) \left(\frac{V_{\text{ash}}}{V_{\text{cake}}}\right)^{C_3}, \tag{121}$$

where C_1, C_2 and C_3 are calibrated rate parameters. Eq. (121) is analogous to the Arrhenius equation, which C_1 being the pre-exponential constant, C_2 being the "activation energy" of ash agglomeration and the volume ratio of ash with respect to soot cake represents the impact of ash "concentration".

Last but not least, a multi-channel model would be needed for an accurate description of real ash loaded filters because ash deposition patterns in real filters vary significantly between channels. Rubino et al. [187] found that ash plugs had a half-elliptical distribution across filter channels, where the longest plug was found in the centre channel. It is apparent that more work is required to develop a filter model that can accurately predicts the accumulation, migration and evolution of ash deposits. The development of such a model will be supported by large amount of experimental data. Non-destructive optical measurements such as MRI and XRT will be helpful.

4.2 Impact of ash deposits on filter performance

Ash deposits in the filter can increase filter pressure drop via different means depending on their form and location. Ash deposits within the filter wall can lead to a reduction in the permeability of the filter wall. The ash layer is a porous medium that gas has to flow through in addition to the soot cake layer. The ash plug can influence the momentum balance in inlet channels via reduction of the effective inlet channel length. These can interfere with regeneration control strategies that rely on the filter pressure drop as an input signal. In general, ash deposition causes active regenerations to occur more frequently due to the overestimation of the actual soot load [131]. Unnecessary active regenerations can reduce the fuel economy of vehicles.

The impact of ash deposits on the permeability of the filter wall is often neglected in modelling studies [266, 269]. Kamp et al. [88] published one of the few studies that did consider this. The following equation has been used by Kamp et al. [88] to estimate the wall permeability with soot load and ash load

$$\frac{1}{\kappa_{\mathrm{w}}} = \frac{1}{\kappa_{\mathrm{w0}}} + \hat{V}_{\mathrm{soot}} \frac{1}{\kappa_{\mathrm{soot}}} + \hat{V}_{\mathrm{ash}} \frac{1}{\kappa_{\mathrm{ash}}}, \tag{122}$$

where $\hat{V}_{\mathrm{soot}}$ and $\hat{V}_{\mathrm{ash}}$ are the volume ratio of soot and ash deposit with respect to the total porous space within the wall. In principle, eq. (38) may be modified to capture the impact of deep bed ash deposits in the unit collector model

$$d_{\mathrm{c}} = 2 \left[\frac{3}{4\pi} \left(\frac{m_{\mathrm{sw}}}{\rho_{\mathrm{sw}}} + \frac{m_{\mathrm{aw}}}{\rho_{\mathrm{aw}}} \right) + \left(\frac{d_{\mathrm{c0}}}{2} \right) \right]^{\frac{1}{3}}, \tag{123}$$

where m_{aw} is the mass of ash deposits and ρ_{aw} is the packing density of ash deposits within the filter wall. It should be noted that the value of ρ_{aw} may increase during the lifetime of the filter as ash deposits undergo sintering after multiple regeneration events.

Similar to the soot cake layer, Darcy's law is often used to describe pressure drop across the ash layer (eq. (40)) [33, 169, 234, 266–268]. Whilst the inertial resistance of the ash layer is often ignored in models, experimental studies have shown that the pressure drop of ash-loaded GPFs can have a quadratic relationship with space velocity which suggests that ash-induced inertial pressure loss is not negligible [40]. The permeability of the ash layer may be modelled analogously to that of the soot cake as shown in eq. (51). Wurzenberger et al. [244] proposed such a model. The model considers a particle cake layer composed of both soot and ash. The particle cake layer is discretised and Darcy's law is used to describe the pressure drop, with the permeability being described as a function of the through-cake distance. The permeability of the hybrid cake is described by Carmen-Kozeny equation

$$\kappa_{\mathrm{cake,hybrid}} = \frac{\varepsilon^3_{\mathrm{cake,hybrid}}}{(1-\varepsilon_{\mathrm{cake,hybrid}})^2} \frac{\overline{d}^2_{\mathrm{cake,hybrid}}}{180}, \tag{124}$$

where the porosity $\varepsilon_{\mathrm{cake,hybrid}}$ is calculated as follows

$$\varepsilon_{\text{cake,hybrid}} = 1 - \alpha_{\text{soot}}\left(1 - \varepsilon_{\text{soot}}\right) - \alpha_{\text{ash}}\left(1 - \varepsilon_{\text{ash}}\right), \tag{125}$$

where α_{soot} and α_{ash} are the **bulk** volume fractions of soot and ash within the cake layer. The average particle diameter of the cake composite $\overline{d}_{\text{p,cake,hybrid}}$ is calculated as

$$\frac{\alpha_{\text{soot}} + \alpha_{\text{ash}}}{\overline{d}^2_{\text{p,cake,hybrid}}} = \frac{\alpha_{\text{soot}}}{\overline{d}^2_{\text{p,soot}}} + \frac{\alpha_{\text{ash}}}{\overline{d}^2_{\text{p,ash}}}. \tag{126}$$

Ash plugs at the end of inlet channels have a smaller impact on the filter pressure drop than the ash layer [83]. On the other hand, mid-channel ash plugs can lead to a drastic change in velocity profiles and a huge increase in pressure drop [232]. If a mid-channel ash plug is impermeable to the gas flow, the effective length of the inlet channel is reduced significantly. Despite its detrimental impact on the pressure drop at channel-scale, the severity of mid-channel plug formation is limited on the overall filter pressure drop as long as there are enough clean channels because gas will preferably flow through paths with the lowest resistances [235].

The formation of an ash layer generally leads to an increase in filtration efficiency [83, 118, 130, 176]. Deep bed filtration is assumed to be negligible once the ash layer is established. When the ash layer has not been established, ash deposition within the filter wall can reduce the duration of deep bed filtration [56]. The impact of ash deposits on the filtration process plays a crucial role in the ash deposition pattern since ash precursors are transported within soot particles. However, there are at least three problems associated with physic-based filtration models for ash deposits:

1. Deep bed ash deposits would have a different packing density with respect to deep bed soot deposits as shown in eq. (123).

2. The partition coefficient approach breaks down when an ash layer is present since the soot cake layer would build on the surface of the ash layer instead of the filter wall.

3. Whilst the filtration efficiency of the ash layer may be modelled using eq. (10), SEM images have shown that ash layers are quite different from spherical packed beds [85, 88]. It is challenging to adequately describe the microstructure of the ash layer.

Ash can hinder mass transfer in catalysed filters [198]. Bagi et al. [9] optically observed the wetting of substrate by ash deposits. The gaseous reactant will have difficulty accessing the catalytic surface due to ash masking. Ash layers can act as a diffusive barrier analogously to soot cake. It should be noted that the impact of ash on the catalytic performance of filters depends on its composition. For example, magnesium-based ash can promote soot regeneration better than calcium-based ash [11].

The impact of ash on heat transfer would be similar to that of soot as described in Section 2.5 albeit with different material properties. Opposing comments about the role of ash on the thermal behaviour of regenerating filters have been made in the literature. Chen et al. [33] suggested that ash deposits can hinder heat transfer and lead to higher peak

temperature during active regeneration, whilst other researchers have suggested that the overall heat capacity of the filter may be increased by ash deposits, which reduces the peak temperature [49, 56]. The impact of ash on heat transfer also depends on the distribution of ash within particulate filters.

Ash deposits can undergo substantial microscopic change during their lifetime in particulate filters. This substantially increases the difficulty of modelling the impact of ash deposits. Whilst sintering and other re-structuring phenomena of ash have been widely reported in experimental studies, limited modelling studies have attempted to consider the evolution of the properties of ash deposits. Linking the microstructure of the ash deposits to their impact on pressure drop, filtration and regeneration is vital for accurate filter models. In addition, the irregular shape of ash deposits further complicates the issue. SEM images have shown that the ash layer may not be formed by spherical ash primary particles; rather it may be molten and have an irregular structure [85]. Hollow ash particles can be formed due to sintering over multiple regeneration events. Although most existing models using an analogous treatment for the ash and soot deposits, describing aged ash deposits as particles or aggregates is inconsistent with experimental observations.

5 Summary

This paper has critically assessed how filtration, regeneration and ash formation have been considered by particulate filter models. In particular, the description of particle deposits is discussed in detail.

The filtration efficiency of filter walls can be estimated precisely with pore-scale models using knowledge of the internal structure of the filter wall that can be obtained by tomography. Soot aggregates can be reasonably approximated as equivalent spherical particles in pore-scale models. Correlations are available for the calculation of the diameter and the density of the equivalent spherical particles. However, the application of pore-scale models is limited due to computational cost. They are rarely applied to study the impact of soot deposits on the filtration behaviour of the walls. Channel-scale filtration models remain the first choice for such tasks. They approximate the complex internal structure of the porous wall using simple geometries, which allow analytical expressions of the filtration efficiency to be derived. Many expressions have been developed in the literature with subtle differences between them. Simulations of pore-scale models can be a useful benchmark for the evaluation of various channel-scale filtration models.

As particles accumulate in a particulate filter, the pressure drop and the filtration efficiency generally increases. The rates of the increase in the pressure drop and filtration efficiency are closely related to the packing of the trapped particles. The channel-scale models available in the literature often consider the number of trapped particles on a mass basis instead of a volume basis. This may compromise their ability to predict filter behaviour when the incoming particles are polydisperse.

The transition from deep bed filtration to soot cake formation is another important phenomenon to model. The deep bed filtration occurs when particles are trapped in the walls of the filter. This eventually gives way to cake filtration once a layer of particles is estab-

lished on the surface of the wall. The rate of transition is dependent on the clogging of the surface pores and the filtration efficiency of the developing soot cake layer. The saturation of the surface pores is usually modelled using a partition coefficient approach by channel-scale models. It should be noted that the calibration process of this approach is sensitive to the spatial discretisation of the wall. Great caution should be taken when quoting the values of the related model parameters. The filtration ability of the developing soot cake has been considered by recent modelling studies. However, some models estimate the filtration behaviour of the developing soot cake with equations that assume the presence of a uniform porous medium, which is not an accurate description of a developing soot cake.

The impact of mass transfer on the performance of catalysed particulate filters is a complex subject. Since current models rely on empirical tuning to obtain good agreement between model results and experimental measurements, a model that is capable of predicting the impact of soot deposits on the mass transfer for a wide range of systems and operating conditions is not expected to be developed in the near future. There is potential in linking the mass transfer models for in-wall soot deposits to the filtration model. This will allow better quantification of the impact of soot deposits on the mass transfer phenomenon. The impact of soot load on heat transfer within particulate filters has not been studied in detail in the literature because it is not an important factor in contrast to other factors such as operating condition and substrate properties. Current approaches in the literature are deemed adequate in this regard.

Regeneration reactions are described by Arrhenius-like equations. Details of many chemical and physical phenomena are rarely explicitly considered in channel-scale models. Their influences are lumped into the values of calibrated parameters such as the pre-exponential constant. This severely limits the applicability of the calibrated kinetics. In particular, the change in the soot deposits during regeneration is often oversimplified since many models only consider the mass of remaining soot deposits. Consideration of the change in the morphology of soot deposits during regeneration will allow a better description of the regeneration process as well as the performances of partially regenerated filters.

Furthermore, the change in soot deposits during regeneration is closely related to the formation of ash deposits. There is plenty of room for the development of ash formation models as they are scarce compare to experimental studies on ash formation in the literature. The development of the ash formation models will need support from extensive experimental data in addition to filter pressure drop measurements. Non-destructive optical measurements will be extremely helpful in assisting the development of ash models. In addition, the impact of ash deposits on filtration behaviour should be studied in detail as it can feed back to the ash formation process. It is important to understand that approximating ash deposits as spherical particles can be inappropriate due to sintering of the ash during regeneration events.

Filter models have been developed and applied successfully in the past, but further improvement can be made in various aspects. Regarding impacts of particulates on filter behaviour, focusing on phenomena occurring at the smaller length scales *i.e.* pore size and particle size will be needed. Since the high computational cost limits the applications of pore-scale models to clean filter walls with relatively simple particle models, channel-

scale models will remain the major tool for predicting filter behaviour during the entire life cycle of the filter. Extension of channel-scale models to consider pore-scale phenomena will be needed to improve the predictive power of models. Further development of channel-scale models can benefit from support by experimental measurements and pore-scale models.

Acknowledgements

This research was supported by the National Research Foundation, Prime Minister's Office, Singapore under its Campus for Research Excellence and Technological Enterprise (CREATE) programme. This project has received funding from the European Union's Horizon 2020 research and innovation programme under grant agreement 814492. This work was supported by the UK Engineering and Physical Sciences Research Council (EPSRC) grant 1622599. The authors would like to thank Royal Dutch Shell for their support. MK gratefully acknowledges the support of the Alexander von Humboldt Foundation.

Nomenclature

Upper-case Roman

A	Pre-exponential constant	(varies)
C	Numerical coefficient	-
C_c	Cunningham correction factor	-
C_F	Shape factor for fibrous medium	-
C_S	Sticking coefficient	-
D	Diffusion coefficient	$m^2\ s^{-1}$
D_m	Diffusivity	$m^2\ s^{-1}$
D_{mm}	Mass-mobility exponent	-
E	Filtration efficiency	-
E	Activation energy	$kg\ mol^{-1}$
F	Force	N
F_f	Friction factor	-
G	Regeneration function of gas	(varies)
ΔH	Enthalpy	$J\ mol^{-1}$
J	Ash re-entrainment flux	$kg\ m^{-2}\ s^{-1}$
K	Kuwabara function	-
K_g	Equilibrium constant	-
Kn	Knudsen number	-
L	Channel length	m
M_r	Molecular weight	$kg\ mol^{-1}$
N_{ic}	Number of inlet channels	-
N_R	Interception parameter	-

P	Pressure	Pa
Pe	Peclet number	-
$\dot{Q}$	Rate of heat generation	W
R	Universial gas constant	J mol^{-1} K^{-1}
Re	Reynolds number	-
S	Specific surface area	m^2 kg^{-1}
Sh	Sherwood number	-
St	Stokes number	-
T	Temperature	K
U	Superficial velocity	m s^{-1}
V	Volume	m^3
W	Wiener process	-
$\hat{V}$	Normalised volume	-
V_{sp}	Soot penetration volume	m^3
$\mathbf{W}$	Wiener process	-
Y	Mass fraction	-

Lower-case Roman

a	Area	m^2
b	Temperature exponent	-
c	Molar concentration	kg mol^{-3}
c_p	Specific heat capacity	J kg^{-1} K^{-1}
d	Diameter	m
d_{ch}	Channel diameter	m
f	Distribution function	-
f_K	Kuwabara geometric function	-
h	Heat transfer coefficient	W m^{-2} K^{-1}
i	Counter	-
k	Rate constant	(varies)
k_B	Boltzmann constant	m^2 kg s^{-2} K^{-1}
k_m	Mass transfer coefficient	m s^{-1}
m	Mass	kg
$\dot{m}$	Mass flow rate	kg s^{-1}
n	Number of particles	-
p	Partial pressure	Pa
p_D	Deposition probability	-
q	Reaction order	-
r	Rate of regeneration	kg s^{-1}
r_{agglo}	Rate of agglomeration of primary ash particles	s^{-1}
$\hat{r}$	Normalised rate of regeneration	s^{-1}
s	Interception exponent	-
t	Time	s
u	Interstitial velocity	m s^{-1}
v	Velocity	m s^{-1}

w	Thickness	m
$\hat{w}_{sat}$	Normalised soot penetration thickness	-
x	Spatial coordinate	m
y	Spatial coordinate	m
z	Spatial coordinate	m

Upper-case Greek

Γ	Regeneration function of particle	(varies)
Λ	Thermal conductivity	W m^{-1} K^{-1}
Π	Structural factor	-
Υ	Stoichiometric coefficient	-
Φ	Partition coefficient	-
Φ_{soot}	Soot density factor	-
Ψ	Selectivity	-

Lower-case Greek

α	Solidity	-
β	Forchheimer constant	m^{-1}
γ	Effectiveness factor	-
δ	Thickness	m
ε	Porosity	-
ζ	Conversion	-
ζ_d	Damage variable	-
η	Single collector efficiency	-
θ	Area correction factor	-
κ	Permeability	m^2
λ	Mean free path	m
μ	Dynamic viscosity	Pa s
ρ	Density	kg m^{-3}
σ	Standard deviation of particle size distribution	m
τ	Tortuosity	-
ϕ	Thiele modulus	-
χ	Shape factor	-
ψ	Percolation constant	-
$\dot{\omega}$	Rate of species molar production	mol m^{-3} s^{-1}

Subscripts

ads	Denotes adsorption
aw	Denotes ash in wall
bulk	Bulk
B	Denotes Brownian diffusion
C	Denotes carbon
c	Denotes collector
cake	Cake

cat	Catalytic
cg	Cake growth
clog	Clog
D	Denotes drag
D	Denotes diffusion
eff	Effective
ext	Denotes external
f	Denotes fibre
frag	Denotes fragmentation
g	Denotes gas
I	Denotes inertial impaction
int	Denotes internal
Kn	Denotes Knudsen diffusion
lim	Denotes limit
mob	Denotes mobility diameter
p	Denotes particle
pore	Denotes pore
pri	Primary particle
R	Denotes interception
ref	Reference
sat	Saturation
sd	Denotes soot dendrites
soot	Denotes soot
SW	Denotes SOF/WBC
sw	Denotes soot in wall
w	Denotes wall
0	Denotes an initial condition

References

[1] Regulation (EC) No 715/2007 on type approval of motor vehicles with respect to emissions from light passenger and commercial vehicles (Euro 5 and Euro 6) and on access to vehicle repair and maintenance information, 2007.

[2] M. Ahmadinejad, J. E. Etheridge, T. C. Watling, A. Johansson, and G. John. Computer simulation of automotive emission control systems. *Johnson Matthey Technology Review*, 59(2):152–165, 2015. doi:10.1595/205651315X687876.

[3] M. Anbari Attar and H. Xu. Correlations between particulate matter emissions and gasoline direct injection spray characteristics. *Journal of Aerosol Science*, 102: 128–141, 2016. doi:10.1016/j.jaerosci.2016.09.006.

[4] T. Andana, M. Piumetti, S. Bensaid, N. Russo, D. Fino, and R. Pirone. CO and Soot Oxidation over Ce-Zr-Pr Oxide Catalysts. *Nanoscale Research Letters*, 11(1), 2016. doi:10.1186/s11671-016-1494-6.

[5] T. Andana, M. Piumetti, S. Bensaid, L. Veyre, C. Thieuleux, N. Russo, D. Fino, E. A. Quadrelli, and R. Pirone. Ceria-supported small Pt and Pt_3Sn nanoparticles for NO_x-assisted soot oxidation. *Applied Catalysis B: Environmental*, 209(x):295–310, 2017. doi:10.1016/j.apcatb.2017.03.010.

[6] K. Aravelli and A. Heibel. Improved Lifetime Pressure Drop Management for Robust Cordierite (RC) Filters with Asymmetric Cell Technology (ACT). In *SAE Technical Paper*. SAE International, 2007. doi:10.4271/2007-01-0920.

[7] H. Arunachalam, G. Pozzato, M. A. Hoffman, and S. Onori. Modeling the thermal and soot oxidation dynamics inside a ceria-coated gasoline particulate filter. *Control Engineering Practice*, 94:104199, 2020. doi:10.1016/j.conengprac.2019.104199.

[8] M. Babaie Rabiee, S. Talebi, O. Abouali, and E. Izadpanah. Investigation of the characteristics of particulate flows through fibrous filters using the lattice Boltzmann method. *Particuology*, 21:90–98, 2015. doi:10.1016/j.partic.2014.11.010.

[9] S. Bagi, C. J. Kamp, V. Sharma, and P. B. Aswath. Multiscale characterization of exhaust and crankcase soot extracted from heavy-duty diesel engine and implications for DPF ash. *Fuel*, 282:118878, 2020. doi:10.1016/j.fuel.2020.118878.

[10] S. Bai, J. Tang, G. Wang, and G. Li. Soot loading estimation model and passive regeneration characteristics of DPF system for heavy-duty engine. *Applied Thermal Engineering*, 100:1292–1298, 2016. doi:10.1016/j.applthermaleng.2016.02.055.

[11] E. A. Bardasz, S. Cowling, A. Panesar, J. Durham, and T. N. Tadrous. Effects of lubricant derived chemistries on performance of the catalyzed diesel particulate filters. In *SAE Technical Paper*. SAE International, 2005. doi:10.4271/2005-01-2168.

[12] C. Beatrice, M. A. Costagliola, C. Guido, P. Napolitano, and M. V. Prati. How much regeneration events influence particle emissions of dpf-equipped vehicles? In *13th International Conference on Engines & Vehicles*. SAE International, 2017. doi:10.4271/2017-24-0144.

[13] I. Belot, D. Vidal, M. Votsmeier, R. E. Hayes, and F. Bertrand. Numerical investigation of the impact of washcoat distribution on the filtration performance of gasoline particulate filters. *Chemical Engineering Science*, 221:115656, 2020. doi:10.1016/j.ces.2020.115656.

[14] S. Bensaid, D. Marchisio, D. Fino, G. Saracco, and V. Specchia. Modelling of diesel particulate filtration in wall-flow traps. *Chemical Engineering Journal*, 154 (1):211–218, 2009. doi:10.1016/j.cej.2009.03.043.

[15] S. Bensaid, N. Russo, and D. Fino. CeO_2 catalysts with fibrous morphology for soot oxidation: The importance of the soot–catalyst contact conditions. *Catalysis Today*, 216:57–63, 2013. doi:10.1016/j.cattod.2013.05.006.

[16] S. Bensaid, M. Piumetti, C. Novara, F. Giorgis, A. Chiodoni, N. Russo, and D. Fino. Catalytic Oxidation of CO and Soot over Ce-Zr-Pr Mixed Oxides Synthesized in a Multi-Inlet Vortex Reactor: Effect of Structural Defects on the Catalytic Activity. *Nanoscale Research Letters*, 11(1):1–14, 2016. doi:10.1186/s11671-016-1713-1.

[17] V. Bermúdez, J. M. Luján, S. Ruiz, D. Campos, and W. G. Linares. New European Driving Cycle assessment by means of particle size distributions in a light-duty diesel engine fuelled with different fuel formulations. *Fuel*, 140:649–659, jan 2015. doi:10.1016/j.fuel.2014.10.016.

[18] R. Bernardoff, B. Hennebert, T. Delvigne, O. Courtois, and P. China. A Study of Ash Accumulation in the After-treatment System of a Gasoline Direct Injection Engine Equipped with a Gasoline Particulate Filter. *SAE Technical Papers*, 2017. doi:10.4271/2017-01-0879.

[19] J. D. Bishop, N. Molden, and A. M. Boies. Using portable emissions measurement systems (PEMS) to derive more accurate estimates of fuel use and nitrogen oxides emissions from modern Euro 6 passenger cars under real-world driving conditions. *Applied Energy*, 242:942–973, 2019. doi:10.1016/j.apenergy.2019.03.047.

[20] E. J. Bissett, M. Kostoglou, and A. G. Konstandopoulos. Frictional and heat transfer characteristics of flow in square porous tubes of wall-flow monoliths. *Chemical Engineering Science*, 84:255 – 265, 2012. doi:10.1016/j.ces.2012.08.012.

[21] N. Bock, J. Jeon, D. Kittelson, and W. F. Northrop. Solid Particle Number and Mass Emissions from Lean and Stoichiometric Gasoline Direct Injection Engine Operation. *SAE Technical Papers*, 2018:1–10, 2018. doi:10.4271/2018-01-0359.

[22] M. Bogarra, J. M. Herreros, A. Tsolakis, A. P. York, and P. J. Millington. Study of particulate matter and gaseous emissions in gasoline direct injection engine using on-board exhaust gas fuel reforming. *Applied Energy*, 180:245–255, 2016. doi:10.1016/j.apenergy.2016.07.100.

[23] M. Bogarra, J. M. Herreros, A. Tsolakis, J. Rodríguez-Fernández, A. P. York, and P. J. Millington. Gasoline direct injection engine soot oxidation: Fundamentals and determination of kinetic parameters. *Combustion and Flame*, 190:177–187, 2018. doi:10.1016/j.combustflame.2017.11.027.

[24] T. Boger, D. Rose, P. Nicolin, N. Gunasekaran, and T. Glasson. Oxidation of Soot (Printex® U) in Particulate Filters Operated on Gasoline Engines. *Emission Control Science and Technology*, 1(1):49–63, 2015. doi:10.1007/s40825-015-0011-1.

[25] R. C. Brown. *Air filtrationan integrated approach to the theory and applications of fibrous filters*. Pergamon Press, 1993.

[26] H. Burtscher. Physical characterization of particulate emissions from diesel engines: a review. *Journal of Aerosol Science*, 36(7):896–932, 2005. doi:10.1016/j.jaerosci.2004.12.001.

[27] L. Cedric, M. Goriaux, P. Tassel, P. Perret, M. Andre, and Y. Liu. Impact of Aftertreatment Device and Driving Conditions on Black Carbon, Ultrafine Particle and NO_x Emissions for Euro 5 Diesel and Gasoline Vehicles. *Transportation Research Procedia*, 14(2):3079–3088, 2016. doi:10.1016/j.trpro.2016.05.454.

[28] T. W. Chan, M. Saffaripour, F. Liu, J. Hendren, K. A. Thomson, J. Kubsh, R. Brezny, and G. Rideout. Characterization of Real-Time Particle Emissions from a Gasoline Direct Injection Vehicle Equipped with a Catalyzed Gasoline Particulate Filter During Filter Regeneration. *Emission Control Science and Technology*, pages 1–14, 2016. doi:10.1007/s40825-016-0033-3.

[29] K. Chen and D. Luss. Temperature excursions in diesel particulate filters: Response to shift to idle. *Industrial & Engineering Chemistry Research*, 50(2):832–842, 2011. doi:10.1021/ie101844r.

[30] K. Chen, K. S. Martirosyan, and D. Luss. Wrong-way behavior of soot combustion in a planar diesel particulate filter. *Industrial & Engineering Chemistry Research*, 48(18):8451–8456, 2009. doi:10.1021/ie900848d.

[31] P. Chen and J. Wang. Air-fraction modeling for simultaneous Diesel engine NO_x and PM emissions control during active DPF regenerations. *Applied Energy*, 122: 310–320, 2014. doi:10.1016/j.apenergy.2014.02.031.

[32] S. C. Chen, J. Wang, H. Fissan, and D. Y. Pui. Optimizing Filtration Experiments for Length and Fractal Dimension Characterization of Non-Spherical Particles. *Aerosol Science and Technology*, 49(8):547–555, 2015. doi:10.1080/02786826.2015.1052038.

[33] T. Chen, Z. Wu, J. Gong, and J. E. Numerical Simulation of Diesel Particulate Filter Regeneration Considering Ash Deposit. *Flow, Turbulence and Combustion*, 97(3):849–864, 2016. doi:10.1007/s10494-016-9717-6.

[34] P. I. Chigada, M. Ahmadinejad, A. D. Newman, A. I. P. Ng, R. Torbati, and T. C. Watling. Impact of SCR Activity on Soot Regeneration and the Converse Effects of Soot Regeneration on SCR Activity on a Vanadia-SCRF®. *SAE Technical Papers*, 2018(2):1–10, 2018. doi:10.4271/2018-01-0962.

[35] B. Choi and K.-S. Lee. LNT/CDPF catalysts for simultaneous removal of NO_x and PM from diesel vehicle exhaust. *Chemical Engineering Journal*, 240:476–486, 2014. doi:10.1016/j.cej.2013.10.100.

[36] S. Choi and H. Seong. Oxidation characteristics of gasoline direct-injection (GDI) engine soot: Catalytic effects of ash and modified kinetic correlation. *Combustion and Flame*, 162(6):2371–2389, 2015. doi:10.1016/j.combustflame.2015.02.004.

[37] S. Choi and H. Seong. Lube oil-dependent ash chemistry on soot oxidation reactivity in a gasoline direct-injection engine. *Combustion and Flame*, 174:68–76, 2016. doi:10.1016/j.combustflame.2016.09.019.

[38] S. Choi, K.-C. Oh, and C.-B. Lee. The effects of filter porosity and flow conditions on soot deposition/oxidation and pressure drop in particulate filters. *Energy*, 77: 327–337, 2014. doi:10.1016/j.energy.2014.08.049.

[39] V. R. Chundru, B. S. Mahadevan, J. H. Johnson, G. G. Parker, and M. Shahbakhti. Development of a 2D Model of a SCR Catalyst on a DPF. *Emission Control Science and Technology*, 5(2):133–171, 2019. doi:10.1007/s40825-019-00115-4.

[40] N. Custer, C. J. Kamp, A. Sappok, J. Pakko, C. Lambert, C. Boerensen, and V. Wong. Lubricant-Derived Ash Impact on Gasoline Particulate Filter Performance. *SAE International Journal of Engines*, 9(3):1604–1614, 2016. doi:10.4271/2016-01-0942.

[41] P. Darcy, P. Da Costa, H. Mellottée, J.-M. Trichard, and G. Djéga-Mariadassou. Kinetics of catalyzed and non-catalyzed oxidation of soot from a diesel engine. *Catalysis Today*, 119(1):252–256, 2007. doi:10.1016/j.cattod.2006.08.056.

[42] Y. Deng, J. Cui, J. E, B. Zhang, X. Zhao, Z. Zhang, and D. Han. Investigations on the temperature distribution of the diesel particulate filter in the thermal regeneration process and its field synergy analysis. *Applied Thermal Engineering*, 123: 92–102, 2017. doi:10.1016/j.applthermaleng.2017.05.072.

[43] Y. Deng, W. Zheng, J. E, B. Zhang, X. Zhao, Q. Zuo, Z. Zhang, and D. Han. Influence of geometric characteristics of a diesel particulate filter on its behavior in equilibrium state. *Applied Thermal Engineering*, 123:61–73, 2017. doi:10.1016/j.applthermaleng.2017.05.071.

[44] C. Depcik and D. Assanis. Simulating area conservation and the gas-wall interface for one-dimensional based diesel particulate filter models. *Journal of Engineering for Gas Turbines and Power*, 130(6), 2008. doi:10.1115/1.2939002.

[45] V. Di Sarli and A. Di Benedetto. Modeling and simulation of soot combustion dynamics in a catalytic diesel particulate filter. *Chemical Engineering Science*, 137:69–78, 2015. doi:10.1016/j.ces.2015.06.011.

[46] V. Di Sarli and A. Di Benedetto. Operating Map for Regeneration of a Catalytic Diesel Particulate Filter. *Industrial and Engineering Chemistry Research*, 55(42): 11052–11061, 2016. doi:10.1021/acs.iecr.6b02521.

[47] V. Di Sarli, G. Landi, L. Lisi, A. Saliva, and A. Di Benedetto. Catalytic diesel particulate filters with highly dispersed ceria: Effect of the soot-catalyst contact on the regeneration performance. *Applied Catalysis B: Environmental*, 197:116–124, 2016. doi:10.1016/j.apcatb.2016.01.073.

[48] A. Dittler. Ash transport in diesel particle filters. In *SAE 2012 International Powertrains, Fuels & Lubricants Meeting*. SAE International, 2012. doi:10.4271/2012-01-1732.

[49] Y. Du, Z. Meng, J. Fang, Y. Qin, Y. Jiang, S. Li, J. Li, C. Chen, and W. Bai. Characterization of soot deposition and oxidation process on catalytic diesel particulate filter with ash loading through an optimized visualized method. *Fuel*, 243:251–261, 2019. doi:10.1016/j.fuel.2019.01.103.

[50] J. E, L. Xie, Q. Zuo, and G. Zhang. Effect analysis on regeneration speed of continuous regeneration-diesel particulate filter based on NO_2-assisted regeneration. *Atmospheric Pollution Research*, 7(1):9–17, 2016. doi:10.1016/j.apr.2015.06.012.

[51] J. E, W. Zuo, J. Gao, Q. Peng, Z. Zhang, and P. M. Hieu. Effect analysis on pressure drop of the continuous regeneration-diesel particulate filter based on NO_2 assisted regeneration. *Applied Thermal Engineering*, 100:356–366, 2016. doi:10.1016/j.applthermaleng.2016.02.031.

[52] J. E, X. Zhao, G. Liu, B. Zhang, Q. Zuo, K. Wei, H. Li, D. Han, and J. Gong. Effects analysis on optimal microwave energy consumption in the heating process of composite regeneration for the diesel particulate filter. *Applied Energy*, 254: 113736, 2019. doi:10.1016/j.apenergy.2019.113736.

[53] J. Easter. *Influence of Fuel Introduction Parameters on the Reactivity and Oxidation Process of Soot from a Gasoline Direct Injection Engine*. PhD thesis, University of Michigan, 2017.

[54] N. A. Eaves, Q. Zhang, F. Liu, H. Guo, S. B. Dworkin, and M. J. Thomson. Coflame: A refined and validated numerical algorithm for modeling sooting laminar coflow diffusion flames. *Computer Physics Communications*, 207:464–477, 2016. doi:10.1016/j.cpc.2016.06.016.

[55] Y. Endo, D.-R. Chen, and D. Y. Pui. Theoretical consideration of permeation resistance of fluid through a particle packed layer. *Powder Technology*, 124(1):119–126, 2002. doi:10.1016/S0032-5910(01)00479-X.

[56] J. Fang, Z. Meng, J. Li, Y. Pu, Y. Du, J. Li, Z. Jin, C. Chen, and G. G.Chase. The influence of ash on soot deposition and regeneration processes in diesel particular filter. *Applied Thermal Engineering*, 124:633–640, 2017. doi:10.1016/j.applthermaleng.2017.06.076.

[57] J. Fang, R. Shi, Z. Meng, Y. Jiang, Z. Qin, Q. Zhang, Y. Qin, J. Tan, and W. Bai. The interaction effect of catalyst and ash on diesel soot oxidation by thermogravimetric analysis. *Fuel*, 258:116151, 2019. doi:10.1016/j.fuel.2019.116151.

[58] M. Fiebig, A. Wiartalla, B. Holderbaum, and S. Kiesow. Particulate emissions from diesel engines: correlation between engine technology and emissions. *Journal of Occupational Medicine and Toxicology*, 9(1):6, 2014. doi:10.1186/1745-6673-9-6.

[59] D. Fino, N. Russo, F. Millo, D. S. Vezza, F. Ferrero, and A. Chianale. New tool for experimental analysis of diesel particulate filter loading. *Topics in Catalysis*, 52 (13):2083, 2009. doi:10.1007/s11244-009-9393-z.

[60] D. Fino, S. Bensaid, M. Piumetti, and N. Russo. A review on the catalytic combustion of soot in Diesel particulate filters for automotive applications: From powder catalysts to structured reactors. *Applied Catalysis A: General*, 509:75–96, 2016. doi:http://dx.doi.org/10.1016/j.apcata.2015.10.016.

[61] R. Foley, J. Johnson, J. Naber, and L. Rogoski. Experimental Measurements of Particulate Matter Distribution in a Catalyzed Particulate Filter. *Emission Control Science and Technology*, 1(1):32–48, 2015. doi:10.1007/s40825-014-0005-4.

[62] S. K. Friedlander. *Smoke, dust and haze: Fundamentals of aerosol behavior*. Wiley, 1977.

[63] R. Fukui, Y. Okamoto, and M. Nakao. Experimental Analysis of Sudden Pressure Increase Phenomenon by Real-Time Internal Observation of Diesel Particulate Filter. *Journal of Engineering for Gas Turbines and Power*, 138(10):102803, 2016. doi:10.1115/1.4033061.

[64] J. Galindo, J. R. Serrano, P. Piqueras, and Óscar García-Afonso. Heat transfer modelling in honeycomb wall-flow diesel particulate filters. *Energy*, 43(1):201–213, 2012. doi:10.1016/j.energy.2012.04.044.

[65] B. Giechaskiel, M. Maricq, L. Ntziachristos, C. Dardiotis, X. Wang, H. Axmann, A. Bergmann, and W. Schindler. Review of motor vehicle particulate emissions sampling and measurement: From smoke and filter mass to particle number. *Journal of Aerosol Science*, 67:48–86, 2014. doi:10.1016/j.jaerosci.2013.09.003.

[66] J. Gong and C. J. Rutland. PDF-based heterogeneous multiscale filtration model. *Environmental Science and Technology*, 49(8):4963–4970, 2015. doi:10.1021/acs.est.5b00329.

[67] J. Gong and C. J. Rutland. Filtration Characteristics of Fuel Neutral Particulates Using a Heterogeneous Multiscale Filtration Model. *Journal of Engineering for Gas Turbines and Power*, 137(11):111507, 2015. doi:10.1115/1.4030282.

[68] J. Gong, S. Viswanathan, D. A. Rothamer, D. E. Foster, and C. J. Rutland. Dynamic Heterogeneous Multiscale Filtration Model: Probing Micro- and Macroscopic Filtration Characteristics of Gasoline Particulate Filters. *Environmental Science and Technology*, 51(19):11196–11204, 2017. doi:10.1021/acs.est.7b02535.

[69] J. Gong, M. L. Stewart, A. Zelenyuk, A. Strzelec, S. Viswanathan, D. A. Rothamer, D. E. Foster, and C. J. Rutland. Importance of filter's microstructure in dynamic filtration modeling of gasoline particulate filters (gpfs): Inhomogeneous porosity and pore size distribution. *Chemical Engineering Journal*, 338:15–26, 2018. doi:10.1016/j.cej.2018.01.006.

[70] R. Greiner, T. Prill, O. Iliev, B. A. van Setten, and M. Votsmeier. Tomography based simulation of reactive flow at the micro-scale: Particulate filters with wall integrated catalyst. *Chemical Engineering Journal*, 378:121919, 2019. doi:10.1016/j.cej.2019.121919.

[71] B. Guan, R. Zhan, H. Lin, and Z. Huang. Review of the state-of-the-art of exhaust particulate filter technology in internal combustion engines. *Journal of Environmental Management*, 154:225–258, 2015. doi:10.1016/j.jenvman.2015.02.027.

[72] O. Haralampous and G. C. Koltsakis. Intra-layer temperature gradients during regeneration of diesel particulate filters. *Chemical Engineering Science*, 57(13): 2345–2355, 2002. doi:10.1016/S0009-2509(02)00135-5.

[73] O. A. Haralampous and G. C. Koltsakis. Oxygen diffusion modeling in diesel particulate filter regeneration. *AIChE Journal*, 50(9):2008–2019, 2004. doi:10.1002/aic.10181.

[74] O. A. Haralampous and G. C. Koltsakis. Back-Diffusion Modeling of NO_2 in Catalyzed Diesel Particulate Filters. *Industrial & Engineering Chemistry Research*, 43(4):875–883, 2004. doi:10.1021/ie034187p.

[75] H. Hayashi and S. Kubo. Computer simulation study on filtration of soot particles in diesel particulate filter. *Computers & Mathematics with Applications*, 55(7): 1450 – 1460, 2008. doi:10.1016/j.camwa.2007.08.012.

[76] L. He, J. Hu, S. Zhang, Y. Wu, R. Zhu, L. Zu, X. Bao, Y. Lai, and S. Su. The impact from the direct injection and multi-port fuel injection technologies for gasoline vehicles on solid particle number and black carbon emissions. *Applied Energy*, 226:819–826, 2018. doi:10.1016/j.apenergy.2018.06.050.

[77] S.-H. Ho, Y.-D. Wong, and V. W.-C. Chang. Developing singapore driving cycle for passenger cars to estimate fuel consumption and vehicular emissions. *Atmospheric Environment*, 97:353–362, 2014. doi:10.1016/j.atmosenv.2014.08.042.

[78] J. Hong, W. C. Hecker, and T. H. Fletcher. Improving the accuracy of predicting effectiveness factors for mth order and langmuir rate equations in spherical coordinates. *Energy & Fuels*, 14(3):663–670, 2000. doi:10.1021/ef9902193.

[79] D. Houi and R. Lenormand. Particle deposition on a filter medium. In *Kinetics of Aggregation and Gelation*, pages 173 – 176. Elsevier, 1984. doi:10.1016/B978-0-444-86912-8.50041-9.

[80] J. Jang, J. Lee, Y. Choi, and S. Park. Reduction of particle emissions from gasoline vehicles with direct fuel injection systems using a gasoline particulate filter. *Science of the Total Environment*, 644:1418–1428, 2018. doi:10.1016/j.scitotenv.2018.06.362.

[81] M. Jeguirim, V. Tschamber, J. Brilhac, and P. Ehrburger. Oxidation mechanism of carbon black by NO_2: Effect of water vapour. *Fuel*, 84(14):1949–1956, 2005. doi:10.1016/j.fuel.2005.03.026.

[82] M. Jeguirim, V. Tschamber, and J. F. Brilhac. Kinetics of catalyzed and non-catalyzed soot oxidation with nitrogen dioxide under regeneration particle trap conditions. *Journal of Chemical Technology & Biotechnology*, 84(5):770–776, 2009. doi:10.1002/jctb.2110.

[83] J. Jiang, J. Gong, W. Liu, T. Chen, and C. Zhong. Analysis on filtration characteristic of wall-flow filter for ash deposition in cake. *Journal of Aerosol Science*, 95: 73–83, 2016. doi:10.1016/j.jaerosci.2016.01.009.

[84] H. Jung, D. B. Kittelson, and M. R. Zachariah. Kinetics and visualization of soot oxidation using transmission electron microscopy. *Combustion and Flame*, 136(4): 445–456, 2004. doi:10.1016/j.combustflame.2003.10.013.

[85] C. J. Kamp, A. Sappok, and V. Wong. Soot and ash deposition characteristics at the catalyst-substrate interface and intra-layer interactions in aged diesel particulate filters illustrated using focused ion beam (fib) milling. *SAE Int. J. Fuels Lubr.*, 5: 696–710, 2012. doi:10.4271/2012-01-0836.

[86] C. J. Kamp, A. Sappok, Y. Wang, W. Bryk, A. Rubin, and V. Wong. Direct measurements of soot/ash affinity in the diesel particulate filter by atomic force microscopy and implications for ash accumulation and dpf degradation. *SAE Int. J. Fuels Lubr.*, 7:307–316, 2014. doi:10.4271/2014-01-1486.

[87] C. J. Kamp, P. Folino, A. Sappok, V. W. Wong, Y. Wang, J. Ernstmeyer, A. Saeid, R. Singh, and B. Kharraja. Ash Accumulation and Impact on Sintered Metal Fiber Diesel Particulate Filters. *SAE International Journal of Fuels and Lubricants*, 8 (2):487–493, 2015. doi:10.4271/2015-01-1012.

[88] C. J. Kamp, S. Zhang, S. Bagi, V. Wong, G. Monahan, A. Sappok, and Y. Wang. Ash Permeability Determination in the Diesel Particulate Filter from Ultra-High Resolution 3D X-Ray Imaging and Image-Based Direct Numerical Simulations. *SAE International Journal of Fuels and Lubricants*, 10(2), 2017. doi:10.4271/2017-01-0927.

[89] C. J. Kamp, S. Bagi, and Y. Wang. Phenomenological investigations of mid-channel ash deposit formation and characteristics in diesel particulate filters. *SAE Technical Papers*, 2019:1–11, 2019. doi:10.4271/2019-01-0973.

[90] A. W. Kandas, I. Gokhan Senel, Y. Levendis, and A. F. Sarofim. Soot surface area evolution during air oxidation as evaluated by small angle X-ray scattering and CO_2 adsorption. *Carbon*, 43(2):241–251, 2005. doi:10.1016/j.carbon.2004.08.028.

[91] I. P. Kandylas and G. C. Koltsakis. NO_2-assisted regeneration of diesel particulate filters: A modeling study. *Industrial & Engineering Chemistry Research*, 41(9): 2115–2123, 2002. doi:10.1021/ie010842m.

[92] W. Kang and B. Choi. Effect of copper precursor on simultaneous removal of PM and NO_x of a 2-way SCR/CDPF. *Chemical Engineering Science*, 141:175–183, 2016. doi:10.1016/j.ces.2015.11.007.

[93] D. Karamitros and G. Koltsakis. Model-based optimization of catalyst zoning on SCR-coated particulate filters. *Chemical Engineering Science*, 173:514–524, 2017. doi:10.1016/j.ces.2017.08.016.

[94] W. Kaspera, P. Indyka, Z. Sojka, and A. Kotarba. Bridging the gap between tight and loose contacts for soot oxidation by vanadium doping of cryptomelane nanorods catalyst using NO_2 as an oxygen carrier. *Catalysis Science and Technology*, 8(12):3183–3192, 2018. doi:10.1039/c8cy00545a.

[95] G. Kastrinaki, S. Lorentzou, and A. G. Konstandopoulos. Soot Oxidation Kinetics of Different Ceria Nanoparticle Catalysts. *Emission Control Science and Technology*, 1(3):247–253, 2015. doi:10.1007/s40825-015-0021-z.

[96] K. Kim, R. Mital, and T. Higuchi. An Investigative Study of Sudden Pressure Increase Phenomenon Across the SCR on Filter Catalyst. *SAE Technical Papers*, 2016, 2016. doi:10.4271/2016-01-2319.

[97] D. B. Kittelson. Engines and nanoparticles: a review. *Journal of Aerosol Science*, 29(5):575–588, 1998. doi:10.1016/S0021-8502(97)10037-4.

[98] E. A. Kladopoulou, S. L. Yang, J. H. Johnson, G. G. Parker, and A. G. Konstandopoulos. A study describing the performance of diesel particulate filters during loading and regeneration - a lumped parameter model for control applications. In *SAE 2003 World Congress & Exhibition*. SAE International, 2003. doi:10.4271/2003-01-0842.

[99] P. Kočí, M. Isoz, M. Plachá, A. Arvajová, M. Václavík, M. Svoboda, E. Price, V. Novák, and D. Thompsett. 3D reconstruction and pore-scale modeling of coated catalytic filters for automotive exhaust gas aftertreatment. *Catalysis Today*, 2018. doi:10.1016/j.cattod.2017.12.025.

[100] G. Koltsakis, O. Haralampous, C. Depcik, and J. C. Ragone. Catalyzed diesel particulate filter modeling. *Reviews in Chemical Engineering*, 29(1):1–61, 2013. doi:10.1515/revce-2012-0008.

[101] G. Koltsakis, M. Mitsouridis, I. Mylonidis, K. Baumgard, R. Duddukuri, W. Zhou, S. George, S. Viswanathan, and A. Heibel. Towards predictive ash accumulation and transport modeling. Presented at CLEERS 2020 on 15/09/2020, 2020. URL https://cleers.org/cleers-workshops/workshop-presentations/entry/2755/.

[102] A. Konstandopoulos, M. Kostoglou, and N. Vlachos. The multiscale nature of diesel particulate filter simulation. *International Journal of Vehicle Design*, 41, 2006. doi:10.1504/IJVD.2006.009676.

[103] A. G. Konstandopoulos. Flow resistance descriptors for diesel particulate filters: Definitions, measurements and testing. In *SAE Technical Paper*. SAE International, 2003. doi:10.4271/2003-01-0846.

[104] A. G. Konstandopoulos and J. H. Johnson. Wall-flow diesel particulate filters—their pressure drop and collection efficiency. In *SAE Technical Paper*. SAE International, 1989. doi:10.4271/890405.

[105] A. G. Konstandopoulos and M. Kostoglou. Analysis of Asymmetric and Variable Cell Geometry Wall-Flow Particulate Filters. *SAE International Journal of Fuels and Lubricants*, 7(2):489–495, 2014. doi:10.4271/2014-01-1510.

[106] A. G. Konstandopoulos, M. Kostoglou, E. Skaperdas, E. Papaioannou, D. Zarvalis, and E. Kladopoulou. Fundamental studies of diesel particulate filters: Transient loading, regeneration and aging. In *SAE 2000 World Congress*. SAE International, mar 2000. doi:10.4271/2000-01-1016.

[107] A. G. Konstandopoulos, E. Skaperdas, and M. Masoudi. Inertial contributions to the pressure drop of diesel particulate filters. In *SAE 2001 World Congress*. SAE International, 2001. doi:10.4271/2001-01-0909.

[108] A. G. Konstandopoulos, E. Skaperdas, and M. Masoudi. Microstructural properties of soot deposits in diesel particulate traps. In *SAE 2002 World Congress and Exhibition*. SAE International, 2002. doi:10.4271/2002-01-1015.

[109] A. G. Konstandopoulos, M. Kostoglou, P. Housiada, N. Vlachos, and D. Zarvalis. Multichannel simulation of soot oxidation in diesel particulate filters. In *SAE Technical Paper*. SAE International, 2003. doi:10.4271/2003-01-0839.

[110] A. G. Konstandopoulos, M. Kostoglou, N. Vlachos, and E. Kladopoulou. Progress in diesel particulate filter simulation. In *SAE 2005 World Congress & Exhibition*. SAE International, 2005. doi:10.4271/2005-01-0946.

[111] A. G. Konstandopoulos, C. Pagkoura, S. Lorentzou, and G. Kastrinaki. Catalytic Soot Oxidation: Effect of Ceria-Zirconia Catalyst Particle Size. *SAE International Journal of Engines*, 9(3), 2016. doi:10.4271/2016-01-0968.

[112] A. G. Konstandopoulos, R. Metallinou, and D. A. Dimitrakis. Growth and Restructuring Phenomena of Deposits in Particulate Filters. *SAE Technical Papers*, 2018: 1–8, 2018. doi:10.4271/2018-01-1265.

[113] A. Kontses, G. Triantafyllopoulos, L. Ntziachristos, and Z. Samaras. Particle number (PN) emissions from gasoline, diesel, LPG, CNG and hybrid-electric light-duty vehicles under real-world driving conditions. *Atmospheric Environment*, 222: 117126, 2020. doi:10.1016/j.atmosenv.2019.117126.

[114] M. Kostoglou and A. G. Konstandopoulos. Effect of soot layer microstructure on diesel particulate filter regeneration. *AIChE Journal*, 51(9):2534–2546, 2005. doi:10.1002/aic.10484.

[115] M. Kostoglou, P. Housiada, and A. G. Konstandopoulos. Multi-channel simulation of regeneration in honeycomb monolithic diesel particulate filters. *Chemical Engineering Science*, 58(14):3273–3283, 2003. doi:10.1016/S0009-2509(03)00178-7.

[116] M. Kostoglou, E. J. Bissett, and A. G. Konstandopoulos. Improved transfer coefficients for wall-flow monolithic catalytic reactors: Energy and momentum transport. *Industrial & Engineering Chemistry Research*, 51(40):13062–13072, 2012. doi:10.1021/ie3011098.

[117] C. Lambert, T. Chanko, D. Dobson, X. Liu, and J. Pakko. Gasoline Particle Filter Development. *Emission Control Science and Technology*, pages 105–111, 2017. doi:10.1007/s40825-016-0055-x.

[118] C. K. Lambert, T. Chanko, M. Jagner, J. Hangas, X. Liu, J. Pakko, and C. J. Kamp. Analysis of Ash in Low Mileage, Rapid Aged, and High Mileage Gasoline Exhaust Particle Filters. *SAE International Journal of Engines*, 10(4), 2017. doi:10.4271/2017-01-0930.

[119] C. T. Lao, J. Akroyd, N. Eaves, A. Smith, N. Morgan, A. Bhave, and M. Kraft. Modelling particle mass and particle number emissions during the active regeneration of diesel particulate filters. *Proceedings of the Combustion Institute*, 37(4): 4831–4838, 2019. doi:10.1016/j.proci.2018.07.079.

[120] C. T. Lao, J. Akroyd, N. Eaves, A. Smith, N. Morgan, D. Nurkowski, A. Bhave, and M. Kraft. Investigation of the impact of the con fi guration of exhaust after-treatment system for diesel engines. *Applied Energy*, 267:114844, 2020. doi:10.1016/j.apenergy.2020.114844.

[121] M. Lapuerta, J. Rodríguez–Fernández, and J. Sánchez-Valdepeñas. Soot reactivity analysis and implications on diesel filter regeneration. *Progress in Energy and Combustion Science*, 78, 2020. doi:10.1016/j.pecs.2020.100833.

[122] H. Lee and C. J. Rutland. Modeling uncontrolled regeneration of diesel particulate filters, taking into account hydrocarbon slip. *Proceedings of the Institution of Mechanical Engineers, Part D: Journal of Automobile Engineering*, 227(2):281–296, 2013. doi:10.1177/0954407012450837.

[123] K. Lee, L. Reed, and J. Gieseke. Pressure drop across packed beds in the low Knudsen number regime. *Journal of Aerosol Science*, 9(6):557 – 565, 1978. doi:10.1016/0021-8502(78)90021-6.

[124] K. F. Lee, N. Eaves, S. Mosbach, D. Ooi, J. Lai, A. Bhave, A. Manz, J. N. Geiler, J. A. Noble, D. Duca, and C. Focsa. Model Guided Application for Investigating Particle Number (PN) Emissions in GDI Spark Ignition Engines. *SAE Technical Papers*, 2019, 2019. doi:10.4271/2019-26-0062.

[125] K. W. Lee and J. A. Gieseke. Collection of aerosol particles by packed beds. *Environmental Science & Technology*, 13(4):466–470, 1979. doi:10.1021/es60152a013.

[126] J. Lelieveld, J. S. Evans, M. Fnais, D. Giannadaki, and A. Pozzer. The contribution of outdoor air pollution sources to premature mortality on a global scale. *Nature*, 525(7569):367–371, 2015. doi:10.1038/nature15371.

[127] H. Liu, Z. Wang, Y. Long, S. Xiang, J. Wang, and M. Fatouraie. Comparative study on alcohol–gasoline and gasoline–alcohol Dual-Fuel Spark Ignition (DFSI) combustion for engine particle number (PN) reduction. *Fuel*, 159:250–258, nov 2015. doi:10.1016/j.fuel.2015.06.059.

[128] J. Liu, J. J. Swanson, D. B. Kittelson, D. Y. Pui, and J. Wang. Microstructural and loading characteristics of diesel aggregate cakes. *Powder Technology*, 241:244 – 251, 2013. doi:10.1016/j.powtec.2013.03.028.

[129] X. Liu, J. Kim, T. Chanko, C. Lambert, and J. Pakko. A Modeling Analysis of Fibrous Media for Gasoline Particulate Filters. *SAE Technical Papers*, 2017, 2017. doi:10.4271/2017-01-0967.

[130] X. Liu, T. Chanko, C. Lambert, and M. Maricq. Gasoline Particulate Filter Efficiency and Backpressure at Very Low Mileage. *SAE Technical Papers*, 2018:1–9, 2018. doi:10.4271/2018-01-1259.

[131] Y. Liu, C. Su, J. Clerc, A. Harinath, and L. Rogoski. Experimental and Modeling Study of Ash Impact on DPF Backpressure and Regeneration Behaviors. *SAE International Journal of Engines*, 8(3), 2015. doi:10.4271/2015-01-1063.

[132] Z. G. Liu and P. K. Wang. Pressure drop and interception efficiency of multifiber filters. *Aerosol Science and Technology*, 26(4):313–325, 1997. doi:10.1080/02786829708965433.

[133] W. Long, H. Huang, J. Serlemitsos, E. Liu, A. H. Reed, and M. Hilpert. Pore-scale study of the collector efficiency of nanoparticles in packings of nonspherical collectors. *Colloids and Surfaces A: Physicochemical and Engineering Aspects*, 358(1):163–171, 2010. doi:10.1016/j.colsurfa.2010.01.043.

[134] Y. Luo, L. Zhu, J. Fang, Z. Zhuang, C. Guan, C. Xia, X. Xie, and Z. Huang. Size distribution, chemical composition and oxidation reactivity of particulate matter from gasoline direct injection (GDI) engine fueled with ethanol-gasoline fuel. *Applied Thermal Engineering*, 89:647–655, 2015. doi:10.1016/j.applthermaleng.2015.06.060.

[135] J. Lupše, M. Campolo, A. Soldati, J. Lupse, M. Campolo, and A. Soldati. Modelling soot deposition and monolith regeneration for optimal design of automotive DPFs. *Chemical Engineering Science*, 151:36–50, sep 2016. doi:10.1016/j.ces.2016.05.008.

[136] Y. Ma, M. Zhu, and D. Zhang. Effect of a homogeneous combustion catalyst on the characteristics of diesel soot emitted from a compression ignition engine. *Applied Energy*, 113:751–757, 2014. doi:10.1016/j.apenergy.2013.08.028.

[137] V. Macián, J. R. Serrano, P. Piqueras, and E. J. Sanchis. Internal pore diffusion and adsorption impact on the soot oxidation in wall-flow particulate filters. *Energy*, 179 (2):407–421, 2019. doi:10.1016/j.energy.2019.04.200.

[138] B. S. Mahadevan, J. H. Johnson, and M. Shahbakhti. Development of a Catalyzed Diesel Particulate Filter Multi-zone Model for Simulation of Axial and Radial Substrate Temperature and Particulate Matter Distribution. *Emission Control Science and Technology*, 1(2):183–202, 2015. doi:10.1007/s40825-015-0015-x.

[139] B. S. Mahadevan, J. H. Johnson, and M. Shahbakhti. Predicting Pressure Drop, Temperature, and Particulate Matter Distribution of a Catalyzed Diesel Particulate Filter Using a Multi-Zone Model Including Cake Permeability. *Emission Control Science and Technology*, 3(2):171–201, 2017.

[140] F. Marchitti and E. Tronconi. Experimental study of the interaction between soot combustion and NH_3-SCR reactivity over a Cu–Zeolite SDPF catalyst. *Catalysis Today*, 267:110–118, 2016. doi:10.1016/j.cattod.2016.01.027.

[141] A. Marotta, J. Pavlovic, B. Ciuffo, S. Serra, and G. Fontaras. Gaseous Emissions from Light-Duty Vehicles: Moving from NEDC to the New WLTP Test Procedure. *Environmental Science and Technology*, 49(14):8315–8322, 2015. doi:10.1021/acs.est.5b01364.

[142] J. W. Martin, M. Salamanca, and M. Kraft. Soot inception: Carbonaceous nanoparticle formation in flames. *Progress in Energy and Combustion Science*, 88:100956, 2022. ISSN 0360-1285. doi:10.1016/j.pecs.2021.100956.

[143] M. Masoudi, A. Heibel, and P. M. Then. Predicting pressure drop of wall-flow diesel particulate filters - theory and experiment. In *SAE Technical Paper*. SAE International, 2000. doi:10.4271/2000-01-0184.

[144] M. Matsuno and T. Kitamura. Direct Visualization of Soot and Ash Transport in Diesel Particulate Filters during Active Regeneration Process. *SAE Technical Papers*, 2019. doi:10.4271/2019-01-2287.

[145] G. Matte-Deschênes, D. Vidal, F. Bertrand, and R. E. Hayes. Numerical investigation of the impact of thermophoresis on the capture efficiency of diesel particulate filters. *Canadian Journal of Chemical Engineering*, 94(2):291–303, 2016. doi:10.1002/cjce.22396.

[146] M. Matti Maricq. Chemical characterization of particulate emissions from diesel engines: A review. *Journal of Aerosol Science*, 38(11):1079–1118, 2007. doi:10.1016/j.jaerosci.2007.08.001.

[147] A. Mayer, J. Czerwinski, M. Kasper, A. Ulrich, and J. J. Mooney. Metal oxide particle emissions from diesel and petrol engines. In *SAE Technical Paper*. SAE International, 2012. doi:10.4271/2012-01-0841.

[148] Z. Meng, J. Fang, Y. Pu, Y. Yan, Y. Wu, Y. Wang, and Q. Song. Experimental study on the influence of DPF micropore structure and particle property on its filtration process. *Journal of Combustion*, 2016, 2016. doi:10.1155/2016/9612856.

[149] Z. Meng, J. Zhang, C. Chen, and Y. Yan. A numerical investigation of the diesel particle filter regeneration process under temperature pulse conditions. *Heat and Mass Transfer*, 2016. doi:10.1007/s00231-016-1924-0.

[150] P. Miceli, S. Bensaid, N. Russo, and D. Fino. Effect of the morphological and surface properties of CeO_2-based catalysts on the soot oxidation activity. *Chemical Engineering Journal*, 278:190–198, 2015. doi:10.1016/j.cej.2014.10.055.

[151] O. Mihai, S. Tamm, M. Stenfeldt, C. Wang-Hansen, and L. Olsson. Evaluation of an Integrated Selective Catalytic Reduction-Coated Particulate Filter. *Industrial and Engineering Chemistry Research*, 54(47):11779–11791, 2015. doi:10.1021/acs.iecr.5b02392.

[152] O. Mihai, S. Tamm, M. Stenfeldt, and L. Olsson. The effect of soot on ammonium nitrate species and NO_2 selective catalytic reduction over Cu–zeolite catalyst-coated particulate filter. *Philosophical Transactions of the Royal Society A: Mathematical, Physical and Engineering Sciences*, 374(2061):20150086, 2016. doi:10.1098/rsta.2015.0086.

[153] O. Mihai, M. Stenfeldt, and L. Olsson. The effect of changing the gas composition on soot oxidation over DPF and SCR-coated filters. *Catalysis Today*, 306:243–250, 2018. doi:10.1016/j.cattod.2017.03.005.

[154] F. Millo, M. Andreata, M. Rafigh, D. Mercuri, and C. Pozzi. Impact on vehicle fuel economy of the soot loading on diesel particulate filters made of different substrate materials. *Energy*, 86:19–30, 2015. doi:10.1016/j.energy.2015.03.076.

[155] M. A. Mitsouridis, D. Karamitros, and G. Koltsakis. Model-Based Analysis of TWC-Coated Filters Performance. *Emission Control Science and Technology*, pages 238–252, 2019. doi:10.1007/s40825-019-00124-3.

[156] N. Mladenov, J. Koop, S. Tischer, and O. Deutschmann. Modeling of transport and chemistry in channel flows of automotive catalytic converters. *Chemical Engineering Science*, 65(2):812 – 826, 2010. doi:10.1016/j.ces.2009.09.034.

[157] S. Mohankumar and P. Senthilkumar. Particulate matter formation and its control methodologies for diesel engine: A comprehensive review. *Renewable and Sustainable Energy Reviews*, 80:1227–1238, 2017. doi:10.1016/j.rser.2017.05.133.

[158] L. Morawska, Z. Ristovski, E. Jayaratne, D. Keogh, and X. Ling. Ambient nano and ultrafine particles from motor vehicle emissions: Characteristics, ambient processing and implications on human exposure. *Atmospheric Environment*, 42(35): 8113–8138, 2008. doi:10.1016/j.atmosenv.2008.07.050.

[159] K. Nakamura, A. Konstandopoulos, M. Kostoglou, T. Shibata, and Y. Hashizume. New asymmetric plugging layout of diesel particulate filters for the pressure drop reduction. *SAE Technical Papers*, 1, 2014. doi:10.4271/2014-01-1512.

[160] J. Neeft. Kinetics of the oxidation of diesel soot. *Fuel*, 76(12):1129–1136, 1997. doi:10.1016/S0016-2361(97)00119-1.

[161] E. Ohara, Y. Mizuno, Y. Miyairi, T. Mizutani, K. Yuuki, Y. Noguchi, T. Hiramatsu, M. Makino, A. Takahashi, H. Sakai, M. Tanaka, A. Martin, S. Fujii, P. Busch, T. Toyoshima, T. Ito, I. Lappas, and C. D. Vogt. Filtration behavior of diesel particulate filters (1). In *SAE Technical Paper*. SAE International, 2007. doi:10.4271/2007-01-0921.

[162] S. Olowojebutu and T. Steffen. A Review of the Literature on Modelling of Integrated SCR-in-DPF Systems. *SAE Technical Papers*, 2017, 2017. doi:10.4271/2017-01-0976.

[163] B. Opitz and M. Votsmeier. A simulation study on the conversion efficiency of catalytically active particulate filters. *Chemical Engineering Science*, apr 2016. doi:10.1016/j.ces.2016.04.010.

[164] M. P. Orihuela, A. Gómez-Martín, J. A. Becerra, R. Chacartegui, and J. Ramírez-Rico. Performance of biomorphic Silicon Carbide as particulate filter in diesel boilers. *Journal of Environmental Management*, 203:907–919, 2017. doi:10.1016/j.jenvman.2017.05.003.

[165] Q. Ou, M. M. Maricq, J. Pakko, T. B. Chanko, and D. Y. Pui. Design and evaluation of a sintered metal fiber filter for gasoline direct injection engine exhaust aftertreatment. *Journal of Aerosol Science*, 133:12–23, 2019. doi:10.1016/j.jaerosci.2019.04.003.

[166] V. Palma, P. Ciambelli, E. Meloni, and A. Sin. Catalytic DPF microwave assisted active regeneration. *Fuel*, 140:50–61, 2015. doi:10.1016/j.fuel.2014.09.051.

[167] J. Pavlovic, B. Ciuffo, G. Fontaras, V. Valverde, and A. Marotta. How much difference in type-approval CO_2 emissions from passenger cars in Europe can be expected from changing to the new test procedure (NEDC vs. WLTP)? *Transportation Research Part A: Policy and Practice*, 111:136–147, 2018. doi:10.1016/j.tra.2018.02.002.

[168] F. Payri, A. Broatch, J. Serrano, and P. Piqueras. Experimental–theoretical methodology for determination of inertial pressure drop distribution and pore structure properties in wall-flow diesel particulate filters (DPFs). *Energy*, 36(12):6731–6744, 2011. doi:10.1016/j.energy.2011.10.033.

[169] F. Payri, F. J. Arnau, P. Piqueras, and M. J. Ruiz. Lumped Approach for Flow-Through and Wall-Flow Monolithic Reactors Modelling for Real-Time Automotive Applications. *SAE Technical Papers*, 2018:1–24, 2018. doi:10.4271/2018-01-0954.

[170] V. R. Pérez and A. Bueno-López. Catalytic regeneration of Diesel Particulate Filters: Comparison of Pt and CePr active phases. *Chemical Engineering Journal*, 279:79–85, 2015. doi:10.1016/j.cej.2015.05.004.

[171] V. Picandet, A. Khelidj, and G. Bastian. Effect of axial compressive damage on gas permeability of ordinary and high-performance concrete. *Cement and Concrete Research*, 31(11):1525 – 1532, 2001. doi:10.1016/S0008-8846(01)00546-4.

[172] M. Piumetti, S. Bensaid, N. Russo, and D. Fino. Nanostructured ceria-based catalysts for soot combustion: Investigations on the surface sensitivity. *Applied Catalysis B: Environmental*, 165:742–751, 2015. doi:10.1016/j.apcatb.2014.10.062.

[173] M. Piumetti, T. Andana, S. Bensaid, N. Russo, D. Fino, and R. Pirone. Study on the CO Oxidation over Ceria-Based Nanocatalysts. *Nanoscale Research Letters*, 11(1):165, 2016. doi:10.1186/s11671-016-1375-z.

[174] M. Piumetti, B. van der Linden, M. Makkee, P. Miceli, D. Fino, N. Russo, and S. Bensaid. Contact dynamics for a solid-solid reaction mediated by gas-phase oxygen: Study on the soot oxidation over ceria-based catalysts. *Applied Catalysis B: Environmental*, 199:96–107, 2016. doi:10.1016/j.apcatb.2016.06.006.

[175] M. Plachá, P. Kočí, M. Isoz, M. Svoboda, E. Price, D. Thompsett, K. Kallis, and A. Tsolakis. Pore-scale filtration model for coated catalytic filters in automotive exhaust gas aftertreatment. *Chemical Engineering Science*, 226:1–10, 2020. doi:10.1016/j.ces.2020.115854.

[176] Q. Porter and A. Strzelec. Benchtop Investigation of Filtration Efficiency and Pressure Drop Behavior of Commercial High Porosity Gasoline Particulate Filters. *SAE Technical Paper Series*, 1:1–11, 2019. doi:10.4271/2019-01-0054.

[177] K. C. Premchand, J. H. Johnson, and S.-L. Yang. Development of a 1-D catalyzed diesel particulate filter model for simulation of the oxidation of particulate matter and gaseous species during passive oxidation and active regeneration. In *SAE Technical Paper*. SAE International, 2013. doi:10.4271/2013-01-1574.

[178] M. Purfürst, S. Naumov, K.-J. Langeheinecke, and R. Gläser. Influence of soot on ammonia adsorption and catalytic DeNO$_x$-properties of diesel particulate filters coated with SCR-catalysts. *Chemical Engineering Science*, 168:423–436, 2017. doi:10.1016/j.ces.2017.04.052.

[179] Y. Qian, Z. Li, L. Yu, X. Wang, and X. Lu. Review of the state-of-the-art of particulate matter emissions from modern gasoline fueled engines. *Applied Energy*, 238:1269–1298, 2019. doi:10.1016/j.apenergy.2019.01.179.

[180] D. Qu, J. Li, and Y. Liu. Research on particulate filter simulation and regeneration control strategy. *Mechanical Systems and Signal Processing*, 87:214–226, 2017. doi:10.1016/j.ymssp.2016.05.039.

[181] V. Ramanathan, G. Carmichael, V. Ramanathan and G. Carmichael, V. Ramanathan, and G. Carmichael. Global and regional climate changes due to black carbon. *Nature Geoscience*, 1(4):221 – 227, 2008. doi:10.1038/ngeo156.

[182] R. Ramdas, E. Nowicka, R. Jenkins, D. Sellick, C. Davies, and S. Golunski. Using real particulate matter to evaluate combustion catalysts for direct regeneration of diesel soot filters. *Applied Catalysis B: Environmental*, 176:436–443, 2015. doi:10.1016/j.apcatb.2015.04.031.

[183] J. Reijnders, M. Boot, and P. de Goey. Particle nucleation-accumulation mode trade-off: A second diesel dilemma? *Journal of Aerosol Science*, 124:95–111, 2018. doi:10.1016/j.jaerosci.2018.06.013.

[184] Q. Ribeyre, A. Charvet, C. Vallières, and D. Thomas. Impact of relative humidity on a nanostructured filter cake – Experimental and modelling approaches. *Chemical Engineering Science*, 161:109–116, 2017. doi:10.1016/j.ces.2016.12.013.

[185] B. R'Mili, A. Boréave, A. Meme, P. Vernoux, M. Leblanc, L. Noël, S. Raux, and B. D'Anna. Physico-Chemical Characterization of Fine and Ultrafine Particles Emitted during Diesel Particulate Filter Active Regeneration of Euro5 Diesel Vehicles. *Environmental Science and Technology*, 52(5):3312–3319, 2018. doi:10.1021/acs.est.7b06644.

[186] D. Rothe, M. Knauer, G. Emmerling, D. Deyerling, and R. Niessner. Emissions during active regeneration of a diesel particulate filter on a heavy duty diesel engine: Stationary tests. *Journal of Aerosol Science*, 90:14–25, 2015. doi:10.1016/j.jaerosci.2015.07.007.

[187] L. Rubino, J. Piotr Oles, and A. La Rocca. Evaluating Performance of Uncoated GPF in Real World Driving Using Experimental Results and CFD modelling. *SAE Technical Papers*, 2017, 2017. doi:10.4271/2017-24-0128.

[188] C. Ruehl, J. D. Herner, S. Yoon, J. F. Collins, C. Misra, K. Na, W. H. Robertson, S. Biswas, M.-C. O. Chang, and A. Ayala. Similarities and Differences Between "Traditional" and "Clean" Diesel PM. *Emission Control Science and Technology*, 1(1):17–23, 2015. doi:10.1007/s40825-014-0002-7.

[189] P. Salatino and F. Zimbardi. A fractal approach to the analysis of low temperature combustion rate of a coal char. II: Model development. *Carbon*, 32(1):51–59, 1994. doi:10.1016/0008-6223(94)90008-6.

[190] A. Sappok. *The Nature of Lubricant-Derived Ash-Related Emissions and Their Impact on Diesel Aftertreatment System Performance*. PhD thesis, Massachusetts Institue of Technology, 2009.

[191] A. Sappok and V. W. Wong. Ash effects on diesel particulate filter pressure drop sensitivity to soot and implications for regeneration frequency and DPF control. *SAE International Journal of Fuels and Lubricants*, 3(1):380–396, 2010. doi:10.4271/2010-01-0811.

[192] A. Sappok, M. Santiago, T. Vianna, and V. W. Wong. Characteristics and effects of ash accumulation on diesel particulate filter performance: Rapidly aged and field aged results. In *SAE World Congress & Exhibition*. SAE International, 2009. doi:10.4271/2009-01-1086.

[193] A. Sappok, Y. Wang, R.-Q. Wang, C. Kamp, and V. Wong. Theoretical and experimental analysis of ash accumulation and mobility in ceramic exhaust particulate filters and potential for improved ash management. *SAE Int. J. Fuels Lubr.*, 7: 511–524, 2014.

[194] A. G. Sappok and V. W. Wong. Detailed chemical and physical characterization of ash species in diesel exhaust entering aftertreatment systems. In *SAE Technical Paper*. SAE International, 2007. doi:10.4271/2007-01-0318.

[195] M. Schejbal, M. Marek, M. Kubíček, and P. Kočí. Modelling of diesel filters for particulates removal. *Chemical Engineering Journal*, 154(1-3):219–230, 2009. doi:10.1016/j.cej.2009.04.056.

[196] M. Schejbal, J. Štěpánek, M. Marek, P. Kočí, and M. Kubíček. Modelling of soot oxidation by NO_2 in various types of diesel particulate filters. *Fuel*, 89(9):2365–2375, 2010. doi:10.1016/j.fuel.2010.04.018.

[197] J. Schobing, V. Tschamber, J.-F. Brilhac, A. Auclaire, and Y. Hohl. Simultaneous soot combustion and NO_x reduction over a vanadia-based selective catalytic reduction catalyst. *Comptes Rendus Chimie*, 21(3):221–231, 2018. doi:10.1016/j.crci.2017.03.002.

[198] H. Seong, S. Choi, S. Lee, N. J. Zaluzec, T. J. Toops, M. J. Lance, D. Kim, and K. Nguyen. Deactivation of Three-Way Catalysts Coated within Gasoline Particulate Filters by Engine-Oil-Derived Chemicals. *Industrial and Engineering Chemistry Research*, 58:10724–10736, 2019. doi:10.1021/acs.iecr.9b00342.

[199] H. Seong, S. Choi, K. E. Matusik, A. L. Kastengren, and C. F. Powell. 3D pore analysis of gasoline particulate filters using X-ray tomography: impact of coating and ash loading. *Journal of Materials Science*, 54(8):6053–6065, 2019. doi:10.1007/s10853-018-03310-w.

[200] J. Serrano, V. Bermúdez, P. Piqueras, and E. Angiolini. On the impact of DPF downsizing and cellular geometry on filtration efficiency in pre- and post-turbine placement. *Journal of Aerosol Science*, 113:20–35, 2017. doi:10.1016/j.jaerosci.2017.07.014.

[201] J. R. Serrano, F. J. Arnau, P. Piqueras, and Óscar García-Afonso. Packed bed of spherical particles approach for pressure drop prediction in wall-flow DPFs (diesel particulate filters) under soot loading conditions. *Energy*, 58:644–654, 2013. doi:10.1016/j.energy.2013.05.051.

[202] J. R. Serrano, H. Climent, P. Piqueras, and E. Angiolini. Filtration modelling in wall-flow particulate filters of low soot penetration thickness. *Energy*, 112:883–898, 2016. doi:10.1016/j.energy.2016.06.121.

[203] Y. Shao. *Physics and modelling of wind erosion*. Springer, 2008.

[204] L. Sileghem, D. Bosteels, J. May, C. Favre, and S. Verhelst. Analysis of vehicle emission measurements on the new WLTC, the NEDC and the CADC. *Transportation Research Part D: Transport and Environment*, 32:70–85, 2014. doi:10.1016/j.trd.2014.07.008.

[205] M. Singh, M. Srilomsak, Y. Wang, K. Hanamura, and R. Vander Wal. Nanostructure changes in diesel soot during NO_2–O_2 oxidation under diesel particulate filter-like conditions toward filter regeneration. *International Journal of Engine Research*, 20(8-9):953–966, 2019. doi:10.1177/1468087418807608.

[206] M. Sirignano and A. D'Anna. Filtration and coagulation efficiency of sub-10 nm combustion-generated particles. *Fuel*, 221:298–302, 2018. doi:10.1016/j.fuel.2018.02.107.

[207] J. D. Smith, C. Ruehl, M. Burnitzki, W. Sobieralski, R. Ianni, D. Quiros, S. Hu, D. Chernich, J. Collins, T. Huai, and H. Dwyer. Real-time particulate emissions rates from active and passive heavy-duty diesel particulate filter regeneration. *Science of the Total Environment*, 680:132–139, 2019. doi:10.1016/j.scitotenv.2019.04.447.

[208] C. M. Sorensen. The mobility of fractal aggregates: A review. *Aerosol Science and Technology*, 45(7):755–769, 2011. doi:10.1080/02786826.2011.560909.

[209] A. M. Stamatellou and A. Stamatelos. Overview of Diesel particulate filter systems sizing approaches. *Applied Thermal Engineering*, 121:537–546, 2017. doi:10.1016/j.applthermaleng.2017.04.096.

[210] B. Stanmore, J. Brilhac, and P. Gilot. The oxidation of soot: a review of experiments, mechanisms and models. *Carbon*, 39(15):2247–2268, 2001. doi:10.1016/S0008-6223(01)00109-9.

[211] Z. Stępień, L. Ziemiański, G. Żak, M. Wojtasik, Ł. Jęczmionek, and Z. Burnus. The evaluation of fuel borne catalyst (FBC's) for DPF regeneration. *Fuel*, 161: 278–286, 2015. doi:10.1016/j.fuel.2015.08.071.

[212] H. Ström, J. Sjöblom, A. S. Kannan, H. Ojagh, O. Sundborg, and J. Koegler. Near-wall dispersion, deposition and transformation of particles in automotive exhaust gas aftertreatment systems. *International Journal of Heat and Fluid Flow*, 70: 171–180, 2018. doi:10.1016/j.ijheatfluidflow.2018.02.013.

[213] A. Strzelec, R. L. Vander Wal, S. A. Lewis, T. J. Toops, and C. S. Daw. Nanostructure and burning mode of light-duty diesel particulate with conventional diesel, biodiesel, and intermediate blends. *International Journal of Engine Research*, 18 (5-6):520–531, 2017. doi:10.1177/1468087416674414.

[214] P.-Q. Tan, C.-Y. Cao, Z.-Y. Hu, and D.-M. Lou. Modeling of soot fragmentation that proceeds in a catalyzed diesel particulate filter of a diesel engine. *Chemical Engineering Journal*, 375:122110, 2019. doi:10.1016/j.cej.2019.122110.

[215] P.-q. Tan, D.-y. Wang, C.-j. Yao, L. Zhu, Y.-h. Wang, M.-h. Wang, Z.-y. Hu, and D.-m. Lou. Extended filtration model for diesel particulate filter based on diesel particulate matter morphology characteristics. *Fuel*, 277:118150, 2020. doi:10.1016/j.fuel.2020.118150.

[216] D. Tang, R. Zhao, S. Wang, J. Wang, L. Ni, and L. Chen. The simulation and experimental research of particulate matter sensor on diesel engine with diesel particulate filter. *Sensors and Actuators, A: Physical*, 259:160–170, 2017. doi:10.1016/j.sna.2017.03.036.

[217] D. Thomas, P. Penicot, P. Contal, D. Leclerc, and J. Vendel. Clogging of fibrous filters by solid aerosol particles experimental and modelling study. *Chemical Engineering Science*, 56(11):3549–3561, 2001. doi:10.1016/S0009-2509(01)00041-0.

[218] D. Thomas, F. Ouf, F. Gensdarmes, S. Bourrous, and L. Bouilloux. Pressure drop model for nanostructured deposits. *Separation and Purification Technology*, 138: 144–152, 2014. doi:10.1016/j.seppur.2014.09.032.

[219] T. J. Toops, J. A. Pihl, C. E. A. Finney, J. Gregor, and H. Bilheux. Progression of Soot Cake Layer Properties During the Systematic Regeneration of Diesel Particulate Filters Measured with Neutron Tomography. *Emission Control Science and Technology*, 1(1):24–31, 2015. doi:10.1007/s40825-014-0008-1.

[220] L. V. Trandafilović, O. Mihai, J. Woo, K. Leistner, M. Stenfeldt, and L. Olsson. A kinetic model for SCR coated particulate filters—Effect of ammonia-soot interactions. *Applied Catalysis B: Environmental*, 241:66–80, 2019. doi:10.1016/j.apcatb.2018.08.076.

[221] D. R. Tree and K. I. Svensson. Soot processes in compression ignition engines. *Progress in Energy and Combustion Science*, 33(3):272–309, 2007. doi:10.1016/j.pecs.2006.03.002.

[222] E. Tronconi, I. Nova, F. Marchitti, G. Koltsakis, D. Karamitros, B. Maletic, N. Markert, D. Chatterjee, and M. Hehle. Interaction of NO_x reduction and soot oxidation in a DPF with cu-zeolite SCR coating. *Emiss. Control Sci. Technol*, 1(x): 134–151, 2015. doi:10.1007/s40825-015-0014-y.

[223] D. Tsujimoto, K. Jin, and T. Fukuma. A Statistical Approach to Improve the Accuracy of the DPF Simulation Model under Transient Conditions. *SAE Technical Papers*, 2019:1–10, 2019. doi:10.4271/2019-01-0027.

[224] A. Überall, R. Otte, P. Eilts, and J. Krahl. A literature research about particle emissions from engines with direct gasoline injection and the potential to reduce these emissions. *Fuel*, 147:203–207, 2015. doi:10.1016/j.fuel.2015.01.012.

[225] T. Uenishi, E. Tanaka, G. Shigeno, T. Fukuma, J. Kusaka, and Y. Daisho. A quasi two dimensional model of transport phenomena in diesel particulate filters - the effects of particle and wall pore diameter on the pressure drop. In *JSAE/SAE 2015 International Powertrains, Fuels & Lubricants Meeting*. SAE International, 2015. doi:10.4271/2015-01-2010.

[226] M. Václavík, M. Plachá, P. Kočí, M. Svoboda, T. Hotchkiss, V. Novák, and D. Thompsett. Structure characterisation of catalytic particulate filters for automotive exhaust gas aftertreatment. *Materials Characterization*, 134:311–318, 2017. doi:10.1016/j.matchar.2017.11.011.

[227] N. Vernikovskaya, T. Pavlova, V. Mokrinskii, D. Murzin, N. Chumakova, and A. Noskov. Soot particulates abatement in diesel engine exhaust by catalytic oxidation followed their trapping in filters. *Chemical Engineering Journal*, 269:416–424, 2015. doi:10.1016/j.cej.2015.01.129.

[228] P. Versaevel, H. Colas, C. Rigaudeau, R. Noirot, G. C. Koltsakis, and A. M. Stamatelos. Some empirical observations on diesel particulate filter modeling and comparison between simulations and experiments. In *SAE Technical Paper*, 2000. doi:10.4271/2000-01-0477.

[229] S. Viswanathan, D. Rothamer, A. Zelenyuk, M. Stewart, and D. Bell. Experimental investigation of the effect of inlet particle properties on the capture efficiency in an exhaust particulate filter. *Journal of Aerosol Science*, 113:250–264, 2017. doi:10.1016/j.jaerosci.2017.08.002.

[230] O. Voutsi, D. Tsinoglou, D. Karamitros, and G. Koltsakis. Pressure Drop of Particulate Filters and Correlation with the Deposited Soot for Heavy-Duty Engines. *SAE Technical Papers*, 2019:692–701, 2019. doi:10.4271/2019-24-0151.

[231] W. Wang and E. J. Bissett. Frictional and Heat Transfer Characteristics of Flow in Triangle and Hexagon Channels of Wall-Flow Monoliths. *Emission Control Science and Technology*, 4(3):198–218, 2018. doi:10.1007/s40825-018-0093-7.

[232] Y. Wang and C. Kamp. The effects of mid-channel ash plug on dpf pressure drop. In *SAE 2016 World Congress and Exhibition*. SAE International, 2016. doi:10.4271/2016-01-0966.

[233] Y. Wang, C. Kamp, A. Saeid, C. Jackson, J. Ernstmeyer, B. Kharraja, A. Sappok, and V. W. Wong. Modeling Study of Metal Fiber Diesel Particulate Filter Performance. *SAE Technical Papers*, 2015, 2015. doi:10.4271/2015-01-1047.

[234] Y. Wang, Y. Pan, C. Su, A. Srinivasan, J. Gong, and C. J. Kamp. Performance of Asymmetric Particulate Filter with Soot and Ash Deposits: Analytical Solution and Its Application. *Industrial and Engineering Chemistry Research*, 57(46):15846–15856, 2018. doi:10.1021/acs.iecr.8b02848.

[235] Y. Wang, Y. Obuchi, J. Zhang, I. Tracy, and V. Wong. Experiments and analyses on stability/mid-channel collapse of ash-deposit wall layers and pre-mature clogging of diesel particulate filters. *SAE Technical Papers*, 2019:1–20, 2019. doi:10.4271/2019-01-0972.

[236] Y. Wang, J. Gong, C. Su, Q. Ou, Q. Lyu, D. Pui, and M. J. Cunningham. Theoretical Framework of a Polydisperse Cell Filtration Model. *Environmental science & technology*, 54(18):11230–11236, 2020. doi:10.1021/acs.est.0c02956.

[237] Y. Wang, C. J. Kamp, Y. Wang, T. J. Toops, C. Su, R. Wang, J. Gong, and V. W. Wong. The origin, transport, and evolution of ash in engine particulate filters. *Applied Energy*, 263:114631, 2020. doi:10.1016/j.apenergy.2020.114631.

[238] T. C. Watling. Geometric description of the soot cake in a one-dimensional model of an octo-square asymmetric particulate filter. *SAE Technical Papers*, 2019:1–23, 2019. doi:10.4271/2019-01-0991.

[239] T. C. Watling, M. R. Ravenscroft, and G. Avery. Development, validation and application of a model for an scr catalyst coated diesel particulate filter. *Catalysis Today*, 188(1):32–41, 2012. doi:10.1016/j.cattod.2012.02.007.

[240] T. C. Watling, M. R. Ravenscroft, J. P. Cleeton, I. D. Rees, and D. A. Wilkins. Development of a Particulate Filter Model for the Prediction of Backpressure: Improved Momentum Balance and Entrance and Exit Effect Equations. *SAE International Journal of Engines*, 10(4), 2017. doi:10.4271/2017-01-0974.

[241] J. Z. Wen, M. J. Thomson, M. F. Lightstone, S. H. Park, and S. N. Rogak. An improved moving sectional aerosol model of soot formation in a plug flow reactor. *Combustion Science and Technology*, 178(5):921–951, 2006. doi:10.1080/00102200500270007.

[242] J. C. Wurzenberger, C. Triebl, S. Kutschi, and C. Poetsch. Particulate Matter Classification in Filtration and Regeneration-Plant Modeling for SiL and HiL Environment. *SAE International Journal of Engines*, 10(4), 2017. doi:10.4271/2017-01-0970.

[243] J. C. Wurzenberger, C. Triebl, and S. Kutschi. Diffusion Supporting Passive Filter Regeneration- A Modeling Contribution on Coated Filters. *SAE Technical Papers*, 2018:1–15, 2018. doi:10.4271/2018-01-0957.

[244] J. C. Wurzenberger, S. Kutschi, and A. Nikodem. Ash transport and deposition, cake formation and segregation-a modeling study on the impact of ash on particulate filter performance. *SAE Technical Papers*, 2019:1–16, 2019. doi:10.4271/2019-01-0988.

[245] G. Xiao, B. Li, H. Tian, X. Leng, and W. Long. Numerical study on flow and pressure drop characteristics of a novel type asymmetric wall-flow diesel particulate filter. *Fuel*, 267, 2020. doi:10.1016/j.fuel.2020.117148.

[246] H. Yamada, S. Inomata, and H. Tanimoto. Particle and VOC Emissions from Stoichiometric Gasoline Direct Injection Vehicles and Correlation Between Particle Number and Mass Emissions. *Emission Control Science and Technology*, 2017. doi:10.1007/s40825-016-0060-0.

[247] H. Yamada, S. Inomata, and H. Tanimoto. Mechanisms of Increased Particle and VOC Emissions during DPF Active Regeneration and Practical Emissions Considering Regeneration. *Environmental Science and Technology*, 51(5):2914–2923, 2017. doi:10.1021/acs.est.6b05866.

[248] K. Yamamoto and Y. Kanamori. Measurements of Size Distribution and Oxidation Rate of PM with NO_x. In *JSAE/SAE 2015 International Powertrains, Fuels & Lubricants Meeting*, 2015. doi:10.4271/2015-01-1995.

[249] K. Yamamoto and T. Sakai. Simulation of continuously regenerating trap with catalyzed DPF. *Catalysis Today*, 242:357–362, 2015. doi:10.1016/j.cattod.2014.07.022.

[250] K. Yamamoto and T. Sakai. Effect of pore structure on soot deposition in diesel particulate filter. *Computation*, 4(4), 2016. doi:10.3390/computation4040046.

[251] K. Yamamoto and Y. Toda. Numerical simulation on flow dynamics and pressure variation in porous ceramic filter. *Computation*, 6(4), 2018. doi:10.3390/computation6040052.

[252] K. Yamamoto and K. Yamauchi. Numerical simulation of continuously regenerating diesel particulate filter. *Proceedings of the Combustion Institute*, 34(2): 3083–3090, 2013. doi:10.1016/j.proci.2012.06.117.

[253] K. Yamamoto, S. Oohori, H. Yamashita, and S. Daido. Simulation on soot deposition and combustion in diesel particulate filter. *Proceedings of the Combustion Institute*, 32(2):1965–1972, 2009. doi:10.1016/j.proci.2008.06.081.

[254] K. Yamamoto, M. Nakamura, H. Yane, and H. Yamashita. Simulation on catalytic reaction in diesel particulate filter. *Catalysis Today*, 153(3):118–124, 2010. doi:10.1016/j.cattod.2010.02.064.

[255] K. Yamamoto, F. Fujikake, and K. Matsui. Non-catalytic after-treatment for diesel particulates using carbon-fiber filter and experimental validation. *Proceedings of the Combustion Institute*, 34(2):2865–2875, 2013. doi:10.1016/j.proci.2012.09.006.

[256] S. Yang, C. Deng, Y. Gao, and Y. He. Diesel particulate filter design simulation: A review. *Advances in Mechanical Engineering*, 8(3):1–14, 2016. doi:10.1177/1687814016637328.

[257] P. Ye, C. Sun, M. Lapuerta, J. Agudelo, R. V. Wal, A. L. Boehman, T. J. Toops, and S. Daw. Impact of rail pressure and biodiesel fueling on the particulate morphology and soot nanostructures from a common-rail turbocharged direct injection diesel engine. *International Journal of Engine Research*, 17(2):193–208, 2016. doi:10.1177/1468087414564229.

[258] A. Yezerets, N. W. Currier, D. H. Kim, H. A. Eadler, W. S. Epling, and C. H. Peden. Differential kinetic analysis of diesel particulate matter (soot) oxidation by oxygen using a step–response technique. *Applied Catalysis B: Environmental*, 61 (1):120–129, 2005. doi:10.1016/j.apcatb.2005.04.014.

[259] A. P. York, M. Ahmadinejad, T. C. Watling, A. P. Walker, J. P. Cox, J. Gast, P. G. Blakeman, and R. Allansson. Modeling of the catalyzed continuously regenerating diesel particulate filter (CCR-DPF) system: Model development and passive regeneration studies. In *SAE Technical Paper*, 2007. doi:10.4271/2007-01-0043.

[260] D. M. Young, D. L. Hickman, G. Bhatia, and N. Gunasekaran. Ash storage concept for diesel particulate filters. In *SAE 2004 World Congress & Exhibition*. SAE International, 2004. doi:10.4271/2004-01-0948.

[261] M. Yu, D. Luss, and V. Balakotaiah. Analysis of flow distribution and heat transfer in a diesel particulate filter. *Chemical Engineering Journal*, 226:68–78, 2013. doi:10.1016/j.cej.2013.04.026.

[262] M. Yu, D. Luss, and V. Balakotaiah. Analysis of ignition in a diesel particulate filter. *Catalysis Today*, 216:158–168, 2013. doi:10.1016/j.cattod.2013.05.003.

[263] M. Yu, D. Luss, and V. Balakotaiah. Regeneration modes and peak temperatures in a diesel particulate filter. *Chemical Engineering Journal*, 232:541–554, 2013. doi:10.1016/j.cej.2013.08.006.

[264] A. A. Yusuf and F. L. Inambao. Effect of cold start emissions from gasoline-fueled engines of light-duty vehicles at low and high ambient temperatures: Recent trends. *Case Studies in Thermal Engineering*, 14:100417, 2019. doi:10.1016/j.csite.2019.100417.

[265] D. Zarvalis, S. Lorentzou, and A. G. Konstandopoulos. A methodology for the fast evaluation of the effect of ash aging on the diesel particulate filter performance. In *SAE Technical Paper*. SAE International, 2009. doi:10.4271/2009-01-0630.

[266] B. Zhang, J. E, J. Gong, W. Yuan, W. Zuo, Y. Li, and J. Fu. Multidisciplinary design optimization of the diesel particulate filter in the composite regeneration process. *Applied Energy*, 181:14–28, 2016. doi:10.1016/j.apenergy.2016.08.051.

[267] B. Zhang, J. E, J. Gong, W. Yuan, X. Zhao, and W. Hu. Influence of structural and operating factors on performance degradation of the diesel particulate filter based on composite regeneration. *Applied Thermal Engineering*, 121:838–852, 2017. doi:10.1016/j.applthermaleng.2017.04.155.

[268] J. Zhang, J. Qi, S. J. Shuai, L. Wang, S. Liu, G. Wang, F. Liu, and J. Brown. Numerical Analysis on the Potential of Reducing DPF Size Using Low Ash Lubricant Oil. *SAE Technical Papers*, 2018:1–11, 2018. doi:10.4271/2018-01-1760.

[269] J. Zhang, V. W. Wong, S. Shuai, Y. Chen, and A. Sappok. Quantitative estimation of the impact of ash accumulation on diesel particulate filter related fuel penalty for a typical modern on-road heavy-duty diesel engine. *Applied Energy*, 229:1010–1023, 2018. doi:10.1016/j.apenergy.2018.08.071.

[270] Z. Zhang, S. L. Yang, and J. H. Johnson. Modeling and numerical simulation of diesel particulate trap performance during loading and regeneration. In *SAE 2002 World Congress & Exhibition*. SAE International, 2002. doi:10.4271/2002-01-1019.

[271] H. Zheng and J. M. Keith. Ignition analysis of wall-flow monolith diesel particulate filters. *Catalysis Today*, 98(3):403–412, 2004. doi:10.1016/j.cattod.2004.08.008.

[272] C. Zhong, J. Gong, W. Liu, and G. Liu. Low temperature, medium temperature and high temperature performance of the continuous regenerative diesel particulate filter assisted by electric regeneration. *Chemical Engineering Science*, 207:980–992, 2019. doi:10.1016/j.ces.2019.07.024.

[273] N. Zouaoui, M. Labaki, and M. Jeguirim. Diesel soot oxidation by nitrogen dioxide, oxygen and water under engine exhaust conditions: Kinetics data related to the reaction mechanism. *Comptes Rendus Chimie*, 17(7):672–680, 2014. doi:10.1016/j.crci.2013.09.004.

[274] A. Zygogianni, M. Syrigou, A. G. Konstandopoulos, and M. Kostoglou. Oxidative Reactivity of Particulate Samples from Different Diesel Combustion Systems and Its Relation to Structural and Spectral Characteristics of Soot. *Emission Control Science and Technology*, 5(2):99–123, 2019. doi:10.1007/s40825-019-00118-1.